CHEMICAL ENRICHMENT HISTORY AND GAS MASS FRACTION OF THE GALAXY CLUSTER ABELL 3112

by

Cemile Ezer

B.S., Physics, Yıldız Teknik University, 2004

M.S., Physics, Boğaziçi University, 2008

Submitted to the Institute for Graduate Studies in
Science and Engineering in partial fulfillment of
the requirements for the degree of
Doctor of Philosophy

Graduate Program in Physics

Boğaziçi University

2017

ACKNOWLEDGEMENTS

I would like to thank several people who have been encouraging and supporting me in recent years as I have worked on this thesis. Firstly, I would like to express my deepest gratitude to my advisor Prof. Nihal Ercan for her continuous support, guidance and understanding throughout my thesis. Without her persistent help, this dissertation would not be possible.

I offer my sincerest gratitude to Dr. Esra Bulbul, who has supported and motivated me with her immense knowledge. I am grateful to her for teaching and imparting her experience with me, which is vital for completion of a challenging work. I thank Dr. Bulbul for her collaboration during the last four years and for her generous support in this thesis.

I owe my sincere appreciation to Prof. Randall Smith for giving me an incredible opportunity by supporting me to become a visiting researcher at Harvard-Smithsonian Center for Astrophysics. It was a working environment beyond my expectations.

I would also like to acknowledge with much appreciation to Prof. Taylan Akdoğan and Prof. Gülay Barbarasoğlu, who supported me in technical work at Boğazici University. I would not have been able to finish my work without their urgent help.

I would also like to express my deep gratitude to the members of my reading committee. Dear Prof. İnci, Prof. Akdoğan, Prof. Karataş, Asst. Prof. Hüdaverdi, Prof. Turgut and Assoc. Prof. Güver thank you for your efforts in correcting my work. Your comments and suggestions have great importance by helping me to improve my thesis.

Last but not least, I would like to thank all my wonderful friends; Neslihan Becerici Schmidt, Bora Işıldak, Burcu Tunç Çamlıbel, Kazım Çamlıbel, Erol Ertan, Serhat Iştın, Medine İldeş, Meral Somunyudan, Didar Talat and Bora Büyüksaraç for

their patience and friendship during my struggles. Without their existence, this period of my life would not be enjoyable and worthwhile.

This dissertation is dedicated to my family for their continuous love, help and support. I am especially grateful to my sister Burcu, my brother Ali and my cousin Eda for always being there for me. It would be a pleasure for me to dedicate this milestone of my life to them.

I am almost sure that I forgot many people that I should have been thankful. These moments are very immense time of my life so please tolerate me on this.

ABSTRACT

CHEMICAL ENRICHMENT HISTORY AND GAS MASS FRACTION OF THE GALAXY CLUSTER ABELL 3112

Clusters of galaxies are the largest concentrations of confined matter in the Universe. Their deep potential well locks all metals produced by stars and galaxies within the intra-cluster medium. The spatial distribution of the metals residing in the intra-cluster medium records all the information on a cluster's nucleosynthesis and chemical enrichment history. In this work, we constrain the radial distribution of supernova enrichment via supernova type Ia and core collapse supernova explosions from a total of 1.2 Ms *Suzaku* XIS and 72 ks *Chandra* observations of the cool-core galaxy cluster Abell 3112 out its virial radius ($\sim$ 1470 kpc).

We adopt a recently developed *snapec* XSPEC model for this study. In this study, it is found that the ratio of the observed supernova type Ia explosions to the core collapse supernova explosions has a uniform distribution at a level of 0.12 – 0.16 out to the cluster's virial radius. The observed fraction of type Ia supernova explosions is in agreement with the corresponding fraction found in our Galaxy and the chemical enrichment of our Galaxy. The non-varying supernova enrichment suggests that the intra-cluster medium in cluster outskirts was enriched by metals at an early stage before the cluster itself was formed during the period of intense star formation activity. Additionally, we find that the 2D delayed detonation model CDDT produces significantly worse fits to the X-ray spectra compared to simple 1D W7 models.

An explicit investigation with these X-ray observations can also be used to probe the approximate baryon fraction of the cluster. In this study, the gas mass fraction is determined as $f_{gas} = 0.21^{+0.16}_{-0.11}$ at R_{500}.

ÖZET

GALAKSİ KÜMESİ ABELL 3112'NİN KİMYASAL ZENGİNLEŞME TARİHİ VE GAZ KÜTLE ORANI

Galaksi kümeleri evrendeki en büyük ve birbirine bağlı olarak hareket eden yapılardır. İçinde bulundukları derin potansiyel kuyu, galaksi kümesinde bulunan yıldızlar ve galaksiler tarafından üretilmiş tüm metalleri küme içi ortamda hapseder. Bu özelliklerinden dolayı, küme içi ortama dağılmış metallerin uzaysal dağılımı nükleosentezin ve kimyasal zenginleşmenin kayıda alınmasına ve incelenmesine olanak sağlayan eşsiz ortamlardır. Bu çalışmada, 1.2 Ms *Suzaku* XIS ve 72 ks *Chandra* uydularından alınan verilerle Abell 3112 soğuk merkezli galaksi kümesinin halkalanma yarıçapını kapsayacak şekilde (1470 kpc) tip Ia süpernova ile tükenmiş çekirdeği çöken süpernova patlamalarının oluşturduğu kimyasal zenginleşmenin yarıçapa bağlı dağılımı ölçülmüştür.

Bu çalışma için, kısa süre önce geliştirilen *snapec* XSPEC modeli uygun bulunmuştur. Bu çalışmada, gözlemlenen tip Ia patlamalarının çekirdeği çöken süpernova patlamalarına oranının kümenin halkalanma yarıçapına kadar sabit bir dağılım gösterdiği ve bu değerin 0.12 – 0.16 aralığında olduğu gözlemlenmiştir. Bu oran, bizim galaksimizdeki oran ve kimyasal zenginleşmesiyle uyumludur. Değişmeyen süpernova zenginleşmesi, küme içi ortamın eteklerinde yıldız oluşumunun maksimuma ulaştığı küme oluşum döneminden evvel erken dönem metal zenginleşmesine uğradığına işaret etmektedir. Buna ilaveten, X-ışını tayf modellemesinde kullanılan iki boyutlu CDDT modelin diğer 1 boyutlu W7 modellere kıyasla daha kötü sonuçlar verdiği tespit edilmiştir.

X-ışını gözlemleri ile yapılan bu detaylı analizler kümenin yaklaşık baryonik madde oranını hesaplamak icin kullanılabilir. Gaz kütlesinin toplam kütleye oranı R_{500} yarıçapında $f_{gas} = 0.21^{+0.16}_{-0.11}$ ölçülmüştür.

TABLE OF CONTENTS

LIST OF FIGURES

LIST OF TABLES

LIST OF SYMBOLS

D_A	Angular diameter distance
f_{gas}	Gas mass ratio
g^{ff}	free-free Gaunt factor
H_0	Hubble Constant
K	Entropy
k_B	Boltzmann constant
M_{Ch}	Chandrasekhar mass
m_e	Electron mass
M_{gas}	Gas mass of the cluster
m_p	Proton mass
M_{total}	Total mass of the cluster
$M_\odot$	Solar Mass
n_e	Electron number density
N_H	Hydrogen Column Density
$P_e(r)$	Electron pressure
$2q$	Two photon
r_{cool}	Cooling radius
r_Δ	Overdensity radius
r_s	Scale radius
t_{cool}	Cooling time
T_{gas}	Gas Temperature
t_H	Hubble Time
V	Volume
Z_i	Ion charge
z	Redshift
$Z_\odot$	Solar Metallicity
ϵ_ν	X-Ray emissivity

μ_e	Electron mean molecular weight
Ω_B	Baryon density of the Universe
Ω_M	Matter density of the Universe
ϕ	Gravitational potential
ϕ_0	Central potential
ρ_{crit}	Critical density of the Universe

LIST OF ACRONYMS/ABBREVIATIONS

ACIS	Advanced CCD Imaging Spectrometer
AGN	Active Galactic Nuclei
APEC	Astrophysical Plasma Emission Code
APED	Astrophysical Plasma Emission Database
ARF	Ancillary Response File
BI	Back Illuminated
CALDB	Calibration Database
CC	Cool Core
CCD	Charge-Coupled Device
CIAO	Chandra Interactive Analysis of Observations
CMB	Cosmic Microwave Background
CXB	Cosmic X-Ray Background
DD	Doubly Degenerate Scenario
DDT	Deflagration-detonation Transition Scenario
d.o.f	Degrees of freedom
EOB	Extensible Optical Bench
FI	Front Illuminated
GH	Galactic Halo
HEASOFT	High Energy Astrophysics Software
HETG	High Energy Transmission Grating
HF	Hot Foreground
HRC	High Resolution Camera
HXD	Hard X-Ray Detector
HWHM	Half Width at Half Maximum
ICM	Intracluster Medium
IMF	Initial Mass Function
ISM	Interstellar Medium
JAXA	Japan Aerospace Exploration Agency

LETG	Low Energy Transmission Grating
LHB	Local Hot Bubble
LSS	Large Scale Structure
NTE	Night-Time-Earth Observations
NXB	Non X-Ray Background
NCC	Non-Cool Core
OBF	Optical block filters (OBF
PSF	Point Spread Function
RASS	ROSAT All Sky Survey
RMF	Redistribution Matrix File
SAA	South Atlantic Anomaly
SAP	Solar Array Paddles
SD	Single Degenerate Scenario
SN	Supernova
SN Ia	Supernova Type Ia
SN Ib	Supernova Type Ib
SN Ic	Supernova Type Ic
SN II	Supernova Type II
SN cc	Supernova Core Collapse
SNe	Supernova Explosions
SWCX	Solar Wind Charge Exchange
SZ	Sunyaev-Zel'dovich Effect
QE	Quantum Efficiency
VAPEC	Variable Astrophysical Plasma Emission Code
WD	White Dwarf
WMAP	Wilkinson Microwave Anisotropy Probe
XIS	X-Ray Imaging Spectrometer
XSPEC	Fitting software package
XRS	X-Ray Spectrometer
XRT	X-Ray Telescope

1. INTRODUCTION

Clusters of galaxies are the largest virialized structures in the Universe, whose mass range is about 10^{14} $M_{\odot}$ to 10^{15} $M_{\odot}$. In the light of the standard hierarchical structure formation model, they form from the merge of the less massive objects such as galaxies and subsclusters, covering a few Mpc [1, 2]. Since 1930s the theories and observations have provided that a cluster of galaxies is a multicomponent system with several galaxies; X-ray emitting hot dilute gas; and dark matter. The matter components, i.e. galaxies and hot dilute gas, account for ∼3% and ∼13% of the total mass respectively. The rest is the dark matter component contributing with a fraction of 84% to the total cluster's mass [3]. The galaxy clusters are of great interest as the cosmological probes since their dynamical timescale are comparable to the age of Universe and so they map the structure of the Universe on very large, i.e. a few hundred Mpc, scales. As being formed at an early epoch and retaining all the imprints of the formation history, they provide fundamental information on the history of the Universe. The observables from the clusters such as temperature and metallicity allow us to compare the theoretical predictions and thus probe into many phenomena such as metal enrichment history and the dark matter and matter distribution in the Universe. The cluster surveys constructed from new generation X-ray satellites, optical telescopes and mm wavelength satellites which are sensitive to Sunyaev-Zel'dovich Effect (SZ) have provided the statistical power to test and constrain cosmological models with accuracy.

1.1. Historical Background of the Clusters of Galaxies

With technological and scientific developments and advanced measurements in optical, radio and X-ray observations, our understanding of the galaxy clusters evolves significantly in time. The historical background of the galaxy clusters are well summarized in the work titled "From Messier to Abell: 200 Years of Science With Galaxy Clusters" of Andrea Biviano [4] and in this section, we will give brief information based on this study.

The first discovery of galaxy clusters dates back to the 18th century, when the French astronomer Charles Messier and the German astronomer F. Wilhelm Herschel independently noticed the existence of concentrations of nebulae on the sky and constructed the first catalogues of these nebulae. The discussion on the galactic or extragalactic nature of the nebulae took decades and it could be revealed through the works of V. M. Slipher and E. Hubble in the 20th century.

With the development of photography techniques in 1900s, the scientists were able to observe more on clusters of galaxies. In 1906, Max Wolf mapped a very detailed description of the Coma and Perseus clusters and thereafter with the investigations of Curtis in 1918, a total of 300 nebulae in the Coma cluster was reached. All these investigations were to question the location of these objects. The discovery of Cepheids in M31 by Edwin Hubble ended the discussions and pointed that these objects are far from our galaxy. In 1929, he published the paper [5] on the relation between distance and radial velocity as a proof of receding nature of extragalactic objects.

The advances in optical techniques opened a new era in the observations. Zwicky and Abell's catalog can be called as the milestones of this era. In 1937, the published paper by Fritz Zwicky pointed out that the ratio of mass to light for galaxies in Coma cluster was too much larger than the stars in the local Milky Way and thereafter this discrepant additional mass without emitting light has been explained by the existence of large amount of dark matter in the clusters [6]. The later landmark paper belongs to George Ogden Abell in 1958. When it is first published, this catalogue contained 2,712 rich clusters of galaxies with north of declination -27° -hence, it is also called "The Northern Survey". This survey was the collection of photographs from Palomar Observatory Sky Survey. Figure 1.1 is taken from Abell's catalog. The distribution of clusters are shown and the empty oval region is not covered by Palomar Observatory Sky Survey. The selection criteria were to be to have at least 30 members with a defined radius 1.5 Mpc (it is also called "Abell Radius") and each has a magnitude range m_3 to m_3+2, where m_3 is the magnitude of the third brightest cluster member. Afterwards, the catalogue was extended by adding 1,361 rich clusters from the Southern Sky Survey.

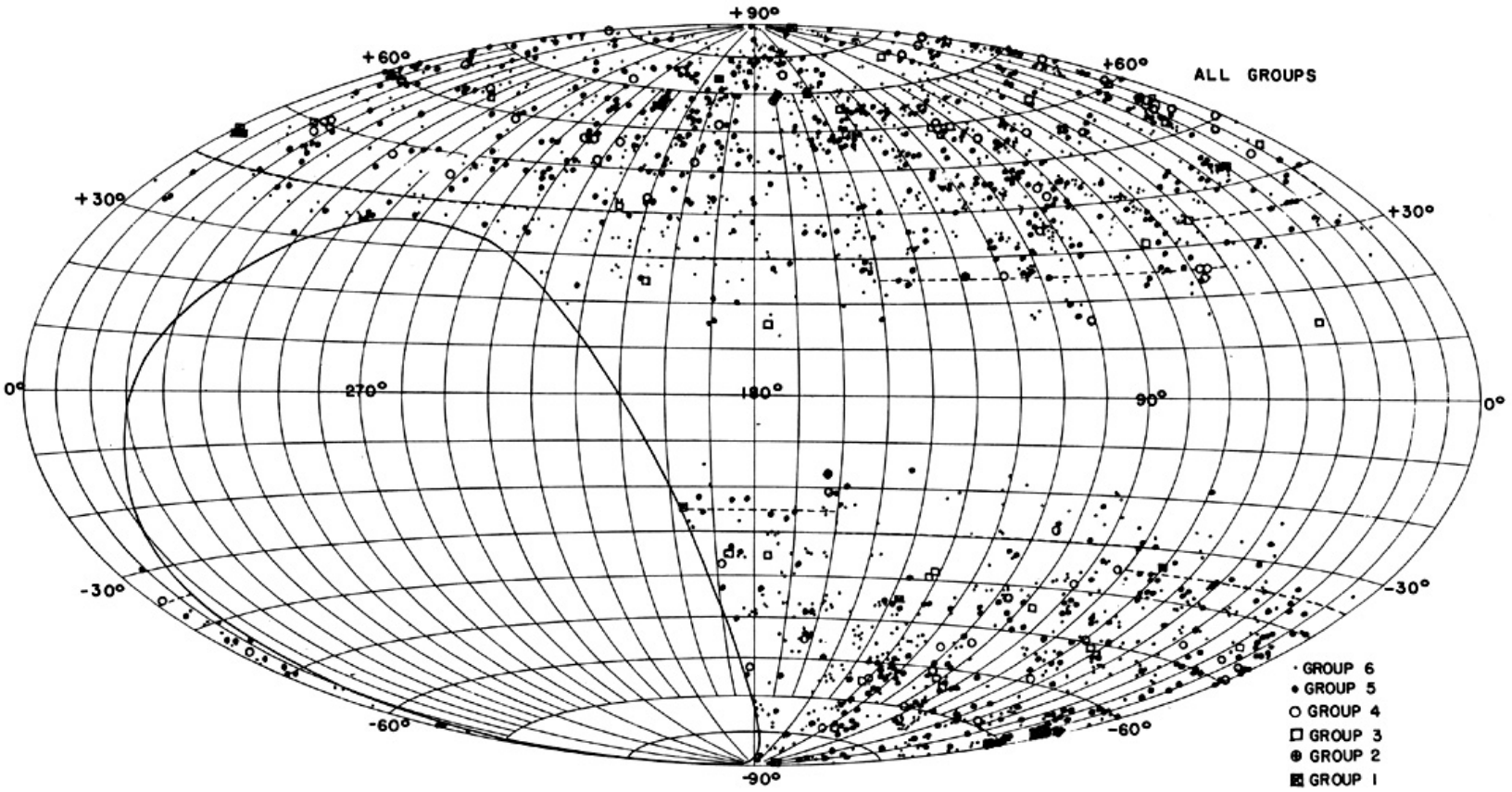

Figure 1.1. The clusters are classified with respect to the distance distribution categorized from 1 to 6 being, 0.027, 0.038, 0.067, 0.090, 0.140, and 0.180 respectively [7].

In 1960s, the radio sources in the clusters were in the center of the attention. The relativistic electrons inside a magnetic field emits synchrotron radiation and this mechanism is the main source of the radio emission in clusters of galaxies. The similar properties of the observed clusters at radio wavelength have importance. Those clusters generally have either high mass with higher overall power output or radio galaxies with large synchrotron jets. The radio source found in Abell clusters at a frequency 1400 MHz, a so-called WAT, has been surveyed such as [8–10]. There also exist a quite number of low frequency catalogs such as [11–15].

The opacity of the atmosphere prevents all kinds of ground based X-ray measurements. The very first X-ray observations were made with balloons and sounding rockets. In the most recent development, satellites orbiting around the Earth are the most advanced tools of the present. In 1949, sounding rocket with a detector in the nose cone was launched to an altitude above the atmosphere and collected X-ray data from the Sun. The first extragalactic object observed in X-ray emission was M87, which is a galaxy located at the centre of the Virgo cluster. In the following years, X-ray sources in the direction of Coma and Perseus as being the nearest richest clusters were also identified [16–19]. The first X-ray sky survey was established after the launch of Uhuru Satellite [20, 21]. And soon after, it is well agreed that the brightness of the X-ray emission from the galaxy clusters is not dependent on time and the mechanism behind the X-ray emission from clusters is well fitted with thermal bremsstrahlung from a hot plasma. From 1970s to today, there are still ongoing missing pieces of these objects and new design X-ray missions such as *Chandra* and *Suzaku* are continuously taking data. With the light of these observations, our understanding of these objects has been dramatically extended and now we use clusters as cosmological probes for such as the history of the formation, nucleosynthesis and the baryonic content of the Universe.

1.2. The Overview of the Clusters of Galaxies

All sky surveys and multi wavelength observations prove that Universe follows a hierarchal model with scaled up to superclusters and filaments. The galaxy clusters are

prominent constituents of the large scale structure (LSS) since these structures evolve from the mostly dark matter driven gravitational collapse of the rare high peaks of primordial perturbations in density. It is known that primordial fluctuations in the early history of the Universe are assumed to be the source of all structures. The most important aspect of the galaxy clusters is that they have enough time to reach the virial equilibrium. The term dynamical timescale can be considered as the elapsed time for a cluster to communicate with itself via its own potential and hence for a cluster with radius R, it is given by:

$$\tau_{dyn} = \frac{R}{V_r} \cong \Big(\frac{R}{\mathrm{Mpc}}\Big)\Big(\frac{V_r}{1000\ \mathrm{km\ s^{-1}}}\Big)^{-1}\mathrm{Gyr} \tag{1.1}$$

where V_r is the radial component of the velocity dispersion. For a typical cluster with $R = 1$ Mpc and $V_r = 10^3$ km s^{-1}, the crossing time for a galaxy from side to the other is 1 Gyr. By reason of the fact that the dynamical time is much shorter than the Hubble time ($t_H = 1/H_0 = 13.5$ Gyr, where $H_0 = 0.074$ Gyr^{-1}), the system is accepted to be in the dynamical equilibrium. The state of equilibrium implies that the gas pressure balances the gravitational force, where the strength of gravity decides the amount of average kinetic energies gained by the gas particles. Hence, the temperature of the gas is the measure of the average kinetic energy and so the average speed of the X-ray emitting gas particles. Despite the dynamically relaxed clusters, however, a great number of observations manifest the recent existence of turbulent regions by jets, sloshing and merging within the many of the clusters, which infers ongoing energy feedback activities. Thus, clusters can be assumed to be quasi-relaxed structures and provide a fair local sample of our Universe.

Luminous matter makes up $\sim 16\%$ of the galaxy cluster. The great percentage of this luminous matter is in the form of hot diffuse gas. The gas is trapped due to the gravitational potential well of the cluster and this structure is called intra-cluster medium (ICM). As soon as the gas is trapped in the cluster's potential well, it reaches the tenuous densities, $n_e = 10^{-4} - 10^{-2}$ electrons cm^{-3}, and temperatures up to $10^7 - 10^8$ K. At such conditions, the gas constitutes a nearly fully ionized optically

thin plasma, which produces X-rays via processes given in detail in Section 2. Except than some heavier elements, the most of the elements are entirely stripped of their electrons. The ICM luminosity is in the order of $10^{43} - 10^{45}$ ergs s^{-1}. The primordial cosmic gas contains 75% hydrogen (H), %24 helium (He) and the rest of light elements such as lithium (Li) and beryllium (Be). However, X-ray observations have proven that the gas is not purely in primordial state, but a comprehensive amount of it has been reprocessed in the stellar populations and injected into the ICM through supernova explosions (SNe) since the total metal abundance found in the ICM is greater than the abundance found in the stellar population [22, 23]. The ICM contains all the elements from the history of the cluster's formation up to today and therefore represents a fossil record of the cluster. The importance of revealing the chemical enrichment history of clusters is to illuminate us on nucleosynthesis and formation history of the Universe.

The density in the core of the cluster is higher than the cluster's outskirts, which foresees strong X-ray emissions from the center (see Figure 1.2). These X-ray emission mechanisms account for the cooling of the ICM. If we define the cooling time by the equation,

$$t_{cool} \propto T_g^{\alpha}/n_e, \text{where -1/2} < \alpha < 1/2 \tag{1.2}$$

when the cluster's cooling time is shorter than the cluster's age, the cooling flow occurs [24]. One of the main characteristics of cool core (CC) clusters is the presence of gas with a cooling time less than the age of the universe leading to both a centrally peaked surface brightness radial profile and a central temperature gradient that rises with radius and mostly flattens in the outskirts [25, 26].

Entropy is another measure of cooling flow in galaxy clusters, which is calculated by,

$$K = k_B T_g n_e^{-2/3} \qquad (\text{KeV cm}^2) \tag{1.3}$$

The entropy as the measure of the thermodynamic state of the ICM ensures that low entropy points cool and dense region. Therefore, for CC clusters we expected to have steep increasing radial profile, whereas non-cool core (NCC) clusters have flatter radial profiles.

The mass of the cluster determines the depth of the gravitational potential well so evidently it has direct impact on cluster's temperature. In the CC clusters, another indicator of the cooling flow is to have the mass deposition rates, which is expected to be large in the center where the cooling time is sharply short. Typical value is in the order of $\dot{M} = 10 - 100\ M_{\odot}\ yr^{-1}$, or even greater than those [27]. On the other hand, NCC clusters have either none or very small cooling radii with insignificant mass deposition values.

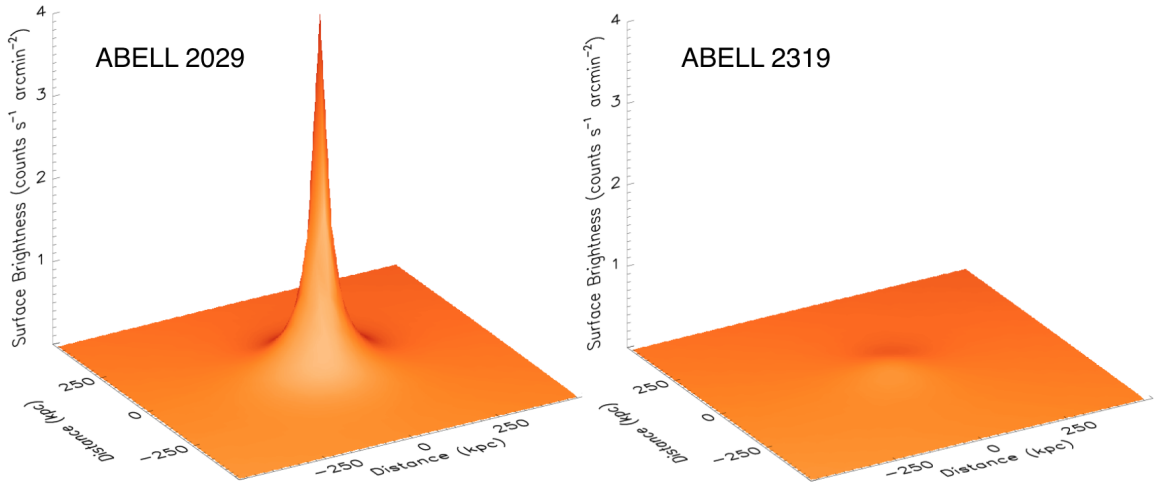

Figure 1.2. The figure on left belongs to CC Abell 2029 cluster, which has strong peak at the center, whereas NCC Abell 2319 cluster on the right has flattened surface brightness distribution [28].

Moreover, X-ray observations of galaxy clusters have been extremely successful at explaining and revealing the existence of dark matter (see Figure 1.3). This picture should drive the attention to that all dust and gas collected in the center and collided with each other during the interaction. We already mention that the vast majority of the cluster's mass is made from dark matter. Therefore, galaxy clusters are unique

reservoirs to study the nature of the gravitational interaction. Temperature and matter density of the ICM are helpful observables since they form by the shape and depth of the cluster's potential well [29].

Figure 1.3. The 1E0657-56 cluster (the bullet cluster) is shown with superimposed X-ray, optic and gravitational lensing maps. The blue parts represent the weakly interacting dark matter, the pink colour is for hot ICM and stellar objects are shown by yellow [30, 31].

1.3. Significance of our studies

The thesis attempts to use the results from a series of analysis to discuss two challenging phenomena. The main aim is to discuss the foundations of the evolution of the metals in large scale structures such as galaxy clusters spanning from the cluster's core out to the virial radius. The existence of large fraction of dark matter generates a deep gravitational potential well, and hence ICM locks all the metals produced via SNe in the stellar populations. Therefore, ICM as being a unique reservoir records all the imprints of chemical evolution history. Metals originate from star burst at $z\sim 2-3$ and are injected into ICM via Type Ia and core collapse SNe, and the abundance

measurements in the ICM can reveal the history of the nucleosynthesis of billions of SNe since the epoch of the star formation peak (z $\sim$ 2-3). There are a comprehensive number of supernova (SN) yields in literature from a comprehensive number of progenitor theories. By using the observed element abundances and their relative ratios, we can discuss and make a conclusion on the progenitor theory supporting the produced yields within the cluster. The main goal of this study is to investigate chemical enrichment history of Abell 3112 galaxy cluster out to R_{200}, which is the radius within which the average density is 200 times higher than the critical density. This study is unique since it will be the first time measurement of supernova contributions from cluster core to the outskirts at this high redshift ($z = 0.0752$).

In order to achieve a deep understanding on the evolution history of metals in the ICM, we will derive and confirm the fraction of gas mass, which has been measured for our cluster before. Galaxy clusters as being large enough to assume representative volume of the Universe are expected to have a nearly cosmic mix of baryonic and dark matter. The gas mass ratio of the cluster is given by,

$$f_{gas} = M_{gas}/M_{tot} \tag{1.4}$$

where M_{gas} and M_{tot} are the gas mass within and total mass of the cluster. This quantity is expected to be invariant with respect to redshift. If we can accurately measure the gas mass fraction of our cluster, this quantity will also reflect the baryonic matter fraction of the Universe, since

$$f_{gas} = M_{gas}/M_{tot} \approx \Omega_B/\Omega_M \tag{1.5}$$

where Ω_B refers to baryonic matter density and Ω_M is the matter density of the Universe.

Abell 3112 is a perfect sample by being an archetypal cool-core cluster and satisfying the conditions of studying these two phenomena by having a relaxed morphology.

It is a distant cluster located at 0.0752. The cluster has a strong radio source, PKS 0316–44, located in the cluster center [32]. The mass deposition rate of $10^{+7}_{-5}\ M_{\odot}\ yr^{-1}$ indicated by *XMM-Newton* observations is much less than the expected rate from cooling flow clusters [33, 34]. It was also reported that a soft X-ray gas was present in the ICM above the contribution from the diffuse 4–5 keV hot gas. This soft excess was first thought to be well described with an additional non-thermal power-law model or with a 1 keV thermal model of low metal abundance [35–37]. However, [34] ruled out the thermal origin of this soft excess using *XMM-Newton RGS* observations, leaving the possibility for non-thermal interpretation of a potential population of relativistic electrons with ∼7% of the cluster's gas pressure. The peaked Fe, Si, and S abundances in the core region reported in [34,38] imply an ongoing Type Ia supernova contribution towards the immediate cluster core ($< 0.5'$) followed by a more uniform core collapse supernova contribution. Finally, [38] used higher resolution *XMM-Newton RGS* observations of Abell 3112 to constrain the SNe models using a new method, *snapec*, and reported that $30.3\% \pm 5.4\%$ of the total SN which enriched the ICM are Type Ia within the immediate core ($\sim$ 50 kpc) of the cluster. It was also reported that the total number of SNe required to create the observed metals is $(1.06 \pm 0.34) \times 10^9$ in the cluster core [38].

In this study, we take a further step to investigate the radial distribution of SN enrichment in Abell 3112 out to the cluster's virial radius by comparing deep *Suzaku* and *Chandra* X-ray observations with the nucleosynthesis models available in the literature. We will also recalculate the gas mass fraction from *Suzaku* observations and confirm our results by *XMM-Newton* study [34].

At the cluster's redshift, $1'$ corresponds to ~ 82 kpc. The cosmological parameters used in the analysis are $H_0 = 73$ km s^{-1} Mpc^{-1}, $\Omega_M = 0.27$, $\Omega_\Lambda = 0.73$. Unless otherwise stated, reported errors correspond to 68% confidence intervals.

1.4. Thesis Outline

The thesis is organized as follows: a brief introduction to galaxy clusters and the thermodynamic properties of ICM physics have been discussed in Chapter 1. To analyze the spectrum of ICM of Abell 3112, the fundamental X-ray emission mechanisms of hot plasma and available codes that utilizes these mechanisms have been reviewed in Chapter 2. In Chapter 3, an overview of the physics of supernova explosions is given. The Chapter 4 contains the technical description and details on instruments that we used in these analyses; namely *Suzaku* and *Chandra* X-ray satellites. Observations and basic data reduction are discussed in Chapter 5. The background and systematic uncertainties relevant to *Suzaku* are described in Chapter 6 and 7. The analysis procedure and the results of global spectral properties of Abell 3112 cluster are given and well explained in Chapter 8. The Chapter 9 provides the robust model and its results revealing the chemical enrichment history of Abell 3112 galaxy cluster. To estimate the baryonic mass fraction of this cluster, we introduce deprojection techniques and obtain results in Chapter 10 and 11. We summarize our foundings in Chapter 12.

2. EMISSION MECHANISMS IN GALAXY CLUSTERS

It is already mentioned that the plasma of the ICM is very tenuous medium in thermal equilibrium from the core to the outskirts. We also know that plasma is optically thin, which means that emitted X-rays leave the cluster without scattered or absorbed. The collisional de-excitation is also negligible in these low density plasmas. Therefore, the modelling of X-ray spectra is trivial by fundamental emission processes. For high temperatures, since almost all the electrons of the elements in the plasma are stripped off, Bremsstrahlung as being a continuum emission determines the shape of the X-ray spectrum. On the other hand, for low temperatures, the line emissions by mainly transitions from K and L shells contribute to the radiation.

Corresponding to these emission processes, there are publicly available codes that can be used to calculate the radiation from plasma in thermal equilibrium. A detailed description of the codes adopted in these analyses is also given.

2.1. Continuum X-ray emission

The continuum emission in galaxy clusters mainly results from thermal bremsstrahlung (free-free), radiative recombination (free-bound) and two photon emission (bound-bound). In this thesis, the emissivity is described as a measure of the emitted power per unit volume and per unit frequency.

Bremsstrahlung is radiation emitted by accelerated electrons under the electrostatic fields of ions and nuclei. This process is also called free-free emission due to the fact that electron and ion are free before and after the collision. The velocity distribution of these electrons follows Maxwellian distribution, therefore this radiation is described as thermal. Since the thermal motion is not direction dependent, the radiation resulting from the thermal motion of these particles is unpolarized. The

Maxwellian speed distribution of electrons imposes that,

$$f_e(v) \propto e^{-\frac{m_e v^2}{2k_B T_{gas}}} v^2 dv \tag{2.1}$$

where m_e is the mass of the electron, k_B is the Boltzmann constant and T_{gas} is the temperature of the plasma. The thermal Bremsstrahlung radiation emissivity of the plasma calculated by integration from the so called minimum and maximum impact parameter is found by,

$$\epsilon_\nu^{ff} \propto n_e n_i g^{ff}(\nu, T_{gas}, Z_i) Z_i^2 T_{gas}^{-1/2} \exp^{-h\nu/k_B T_{gas}} \text{ erg s}^{-1}\text{cm}^{-3}\text{Hz}^{-1} \tag{2.2}$$

where Z_i is ion charge, n_e and n_i are the electron and ion density of the plasma, ν is the frequency of the emitted photon. The classical treatment gives this result and g^{ff} is known as Gaunt factor responsible for quantum mechanical corrections [39]. The average value of the Gaunt correction factor is close to unity. The emission has main dependence on the temperature of the plasma and the density of the ions. For an optically thin plasma, $n_e \approx n_i$, sum over frequency gives the total emissivity,

$$\epsilon \sim n_e^2 T_{gas}^{1/2} \tag{2.3}$$

Thermal Bremsstrahlung is the most dominant mechanism, which gives the shape of the X-ray spectra. There is also a small contribution form radiative recombination and two photon emission. However, at high temperatures ($> 10^7$ K), this process is the most dominant driven mechanism for producing X-ray radiation.

Radiative Recombination is a free-bound transition. This process involves the recapture of a free electron by an ion into a quantized bound state by a photon emission. Hence, this requires the medium to be highly ionized, similar to free-free emission. The continuum emissivity due to the radiative recombination is given by the equation,

$$\epsilon_\nu^{bf} \propto n_e n_j \sum_l \frac{\omega_{l,i}}{\omega_{gs,j}} a_{\nu,i}^l \nu^3 T_{gas}^{-3/2} \exp^{-(h\nu - \chi_{l,i})/k_B T_{gas}} \tag{2.4}$$

where l sums over all energy levels of ion i, ω refers to statistical weights of atomic levels and gs stands for ground state of the recombining ion j, $a^l_{\nu,i}$ is the photoionization cross section and $\chi_{l,i}$ is the ionization potential at each energy level of the ion i [40, 41]. We may summarize that when the ICM temperature $k_B T_{gas} << 0.1$ keV, the free-bound emission becomes the most dominant continuum emission mechanism. On the other hand, Bremsstrahlung dominates the continuum contribution at the ICM temperatures $k_B T_{gas} >> 1.0$ keV.

The final component is the two photon emission process. Two photon emission occurs when an electron in an excited state of $2s$ can not undergo direct downward transition ($1s$) since it is forbidden, however this transition becomes very high probable for low density ionized gas so the electron decays from the $2s$ to the $1s$ orbit by emitting two photons. Two photon emissivity is defined by the equation,

$$\epsilon^{2q}_{\nu} \propto n_p n_e \gamma_{\nu}(2q) \tag{2.5}$$

where n_p and n_e are the number density of protons and electrons respectively, the function $\gamma_{nu}(2q)$ is given in [40].

The sum of thermal Bremsstrahlung, radiative recombination and two photon emission gives the total continuum emissivity and it is expressed as,

$$\epsilon^{cont}_{\nu} = \epsilon^{ff}_{\nu} + \epsilon^{bf}_{\nu} + \epsilon^{2q}_{\nu} \tag{2.6}$$

2.2. Line X-ray emission

Line emission is also a primary X-ray radiation source in the plasma, especially at lower temperatures. The production of X-ray radiation due to the line emission originates from the electron transition between two different energy states. The calculated line emission from a plasma considers all energy levels of all ionization levels at a specific temperature, therefore the calculation is highly nontrivial. The line emissivity

due to a collisionally excited plasma is given by the equation,

$$\int \epsilon_{\nu}^{line} d\nu \propto n_i n_e \frac{\Omega(T_{gas})B}{\omega_{gs,i}} T_{gas}^{-1/2} \nu e^{-\Delta E/k_B T_{gas}} \tag{2.7}$$

where B is the branching ratio which is the probability of decay into the lower state, Ω is the collisional strength, $h\nu$ is the energy of the transition and ΔE is the excitation energy above the ground state of the excited level.

The strong line emission at 6.7 keV, which is identified as Fe-K line, is first discovered in Perseus cluster [42] and thereafter it is discovered in almost all of the clusters. In general, the spectra contain K-shell transitions from H/He-like Fe at higher temperatures since all the other elements are fully ionized, whereas at lower temperatures K-shell transitions from other elements such as O, S and Si contribute to the total radiation.

Figure 2.1 shows X-ray spectra of clusters at two different temperatures, where individual contributions from both continuum and line emissions are plotted. The blue line represents thermal Bremsstrahlung where for the higher temperature it gives the most dominant contribution to the total shape of the spectrum. Radiative recombination is indicated by the green line, whereas the two photon process is plotted by the purple. The most prominent line emissions are also labelled. This figure identifies the most relevant emission lines in clusters and it is clearly seen that at lower temperatures line emissions are predominant as the elements are not fully ionized.

2.3. The Modelling of the Collisionally Ionized Plasma

To model the hot dilute plasma, there are many spectral codes available in literature. In our analysis, the cluster emission is modelled with ATOMDB version 2.0.2 [44,45]. XSPEC v12.9.0 is used to perform the spectral fits [46] with the extended C-statistic as an estimator of the goodness-of-fit. We may give brief information on the main features of the models that we use to model the ICM of Abell 3112.

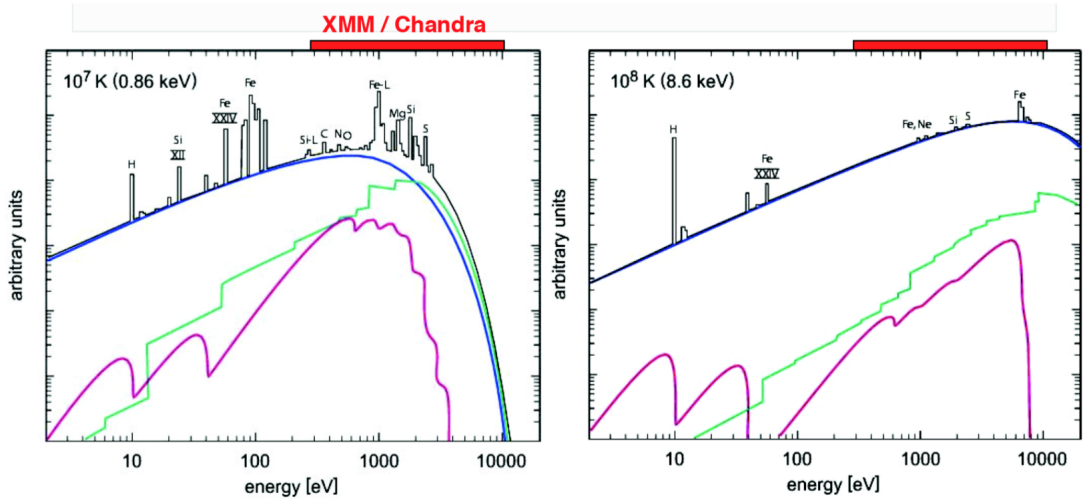

Figure 2.1. Comparison of X-ray spectra at two different temperatures which contain the total continuum and strong line emissions [43].

2.3.1. Astrophysical Plasma Emission Code (APEC)

The *apec* code, written in C language, principally calculate the line emissions and the continuum emissions from a hot and collisionally ionized plasma. The temperature in keV range is valid in galaxy clusters. Thermal bremsstrahlung is the dominant process for this range. However, considering thermal bremsstrahlung as the only process will cause the underestimation of modelling the plasma at lower temperatures. Therefore, we use *apec* code including both thermal bremsstrahlung, radiative recombination and two photon emissions. To estimate the line emissions, *apec* code utilizes the APED (Astrophysical Plasma Emission Database), which consists of all possible atomic rates and wavelengths to calculate the line emissions from an optically thin thermal plasma.

This code calculate a four set of parameters; plasma temperature kT in keV, the metallicity in solar units, the redshift of the sample and the normalization in (cm^{-5}) by using the comparison of theoretical emission model with input spectrum. It is essential to note that the temperature of the X-ray emitting plasma determines the shape of the spectrum. The normalization parameter refers to emission measure of the plasma,

$$Norm = \frac{10^{-14}}{4\pi[D_A(1+z)^2]} \int n_e(r) n_H(r) dV \tag{2.8}$$

where D_A is the angular diameter distance to the source, z is the cluster's redshift, n_e and n_H are the number densities of electron and hydrogen, respectively. This equation ensures that normalization factor is directly proportional to emission measure of the X-ray emitting plasma.

2.3.2. Variable Astrophysical Plasma Emission Code (VAPEC)

The *vapec* has the same origin with *apec* model so that it also uses the atomic data from APED. The main difference is that the *vapec* model allows to calculate the abundances of He, C, N, O, Ne, Mg, Al, Si, S, Ar, Ca, Fe, and Ni in solar units individually. The element abundances retained in the ICM can be depicted as the fossil records of the formation history, since it results from the contribution of different supernova explosions in the stellar population to the nucleosynthesis of heavy elements. We will discuss the origin of these metals in the following chapter.

3. THE PHYSICS OF SUPERNOVA EXPLOSIONS

3.1. Supernova Explosions

A supernova (SN) occurs when a star at the end of its life cycle explodes and releases most of its energies. This phenomenon is considered as the most luminous recorded event after the Big-Bang and the burst of the radiation expelled from the explosion can make the entire galaxy shine for weeks or even months. The amount of energy provided by SNe is in the order of $\sim 10^{51}$ erg, which is 10^{10} times energitic than our Sun. The energy is ejected in the form of kinetic energy and electromagnetic radiation and the ejecta contains heavy element synthesis. Therefore, SNe are responsible for the transportation and cycle of the elements through the galaxies, stars and life. The chemical composition of the ejecta is strongly depended on the progenitor star. However, specific elements play crucial role to differentiate between the nature of the explosion, and so the type of the SN.

3.2. Classification

The classification of SN explosions is broadly possible with respect to two observable features: the presence or absence of distinct chemical element lines in their spectra and their light curves. According to the absence or presence of the H lines, the SN explosions can be historically classified in two types; Type I and Type II respectively. If the spectrum of the SN ejecta contains H lines, this is called Type II (hereafter SN II). However, the absence of H lines is introduced as a primary indicator for Type I (hereafter SN I). Furthermore, with the advances in scientific observations, each of these classes is subdivided into subclasses. Type I class is divided into three subclasses; silicon (Si) rich Type Ia (hereafter SN Ia), non-ionized helium (He) rich Type Ib (hereafter SN Ib), and neither Si nor He line Type Ic (hereafter SN Ic). Figure 3.1 gives a schematic view of classification of SN types. The existence or absence of distinct absorption lines of specific elements lead a broad classification between supernova types. This figure also divides SNe with respect to their explosions mechanisms.

Additionally, although there are numerous exceptional examples, the well known sub-classification of SN II can be done by the shape of the light curve. A deep distinction between SN II explosions is possible by having rapid decrease in the light curve after the maximum light (Type II-P, hereafter SN II-P) and presenting a linear luminosity drop (Type II-L, hereafter SN II-L) [48]. To understand the nature of the classification, the measured features are demonstrated in Figure 3.2; where SN1996X and SN1994I are used for SN Ia, and SN1997B and SN1999dn are used for SN Ic, and SN1990I is for SN Ib, and SN1987A is for SN II [48].

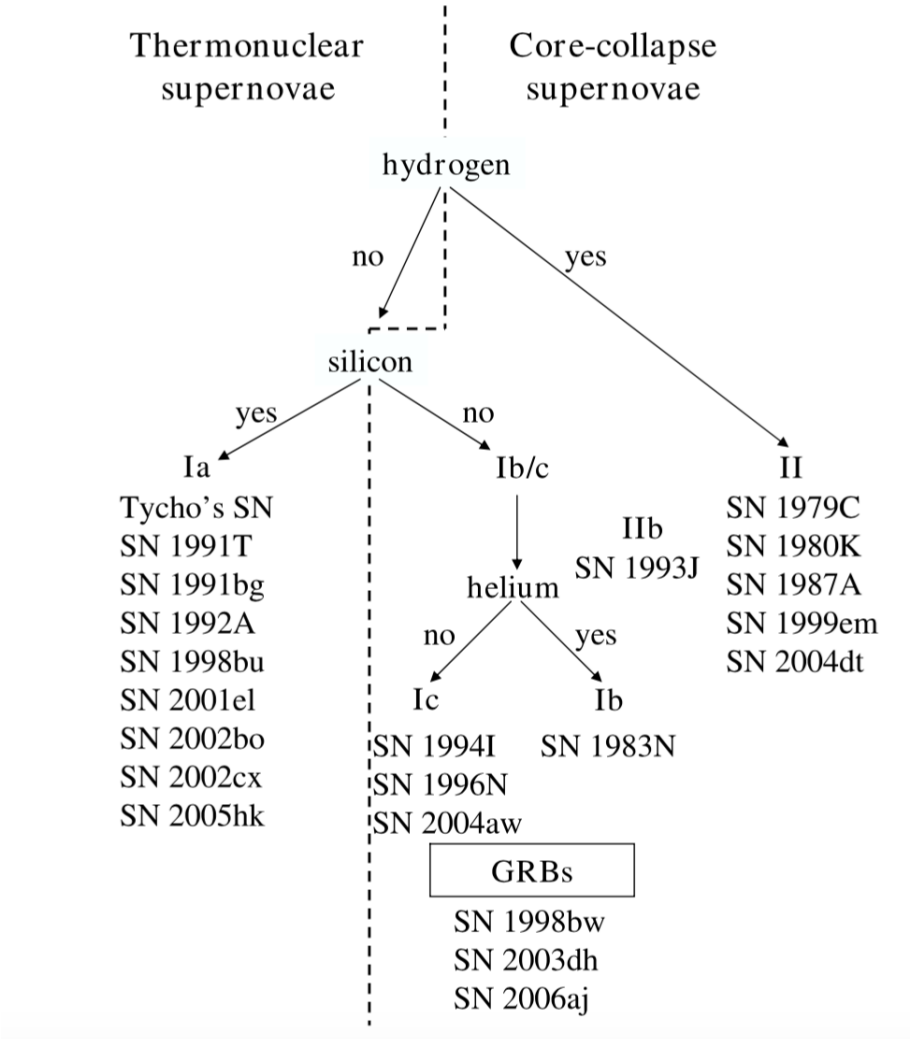

Figure 3.1. The schematic view of classified supernova types with peculiar examples [47].

The main classification is possible through the explosion mechanisms; core collapse SN (hereafter SN cc), and thermonuclear SN (SN Ia). Unlike SN Ia explosions, SN Ib and SN Ic are discovered in very near the star forming regions and thus accepted as having explosion mechanism ignited by the gravitational collapse of a massive star. Therefore, together with SN II, these two types of SN are collected under the same category named SN cc. On the other hand, SN Ia is started from thermonuclear explosions of white dwarfs near the Chandrasekhar mass limit. Although these two classes are two diverse phenomena, they have the same order of magnitude explosion energy ($\sim 10^{51}$ erg) and enhance the metallicity of the interstellar medium in common [49]. We are going to discuss the physical foundations of these two SN classes in the following sections.

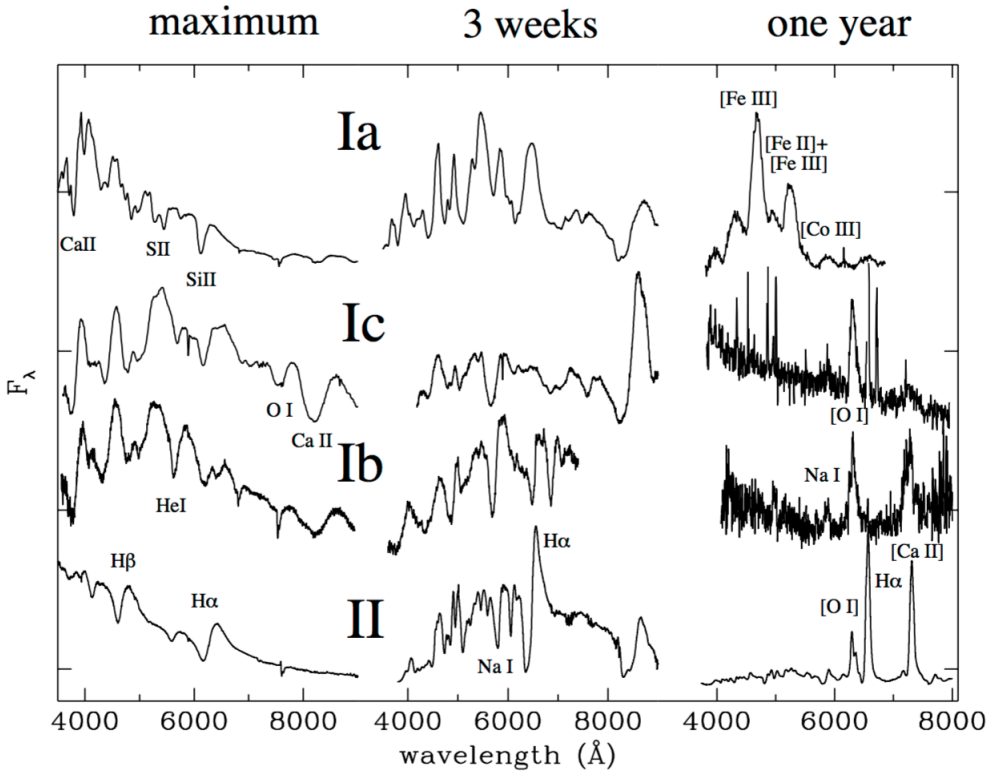

Figure 3.2. The typical optical spectra of the SN types at maximum brightness, and three weeks and one year after maximum [48].

3.3. Core Collapse Supernova Explosions (SN cc)

Massive stars with a zero-age-main-sequence mass (ZAMS) heavier than 8 – 10 $M_{\odot}$ turns into core collapse SNe at the end of their lives. The onion-like structure (see Figure 3.3) illustrates that a massive star at the end of its life left with various layers, where nuclear burning still continues. As having the most stable nuclei (Fe) in the core, nuclear fusion can not take place. Besides that Fe or Ni has the highest binding energy, and hence with no nuclear source to balance the inward gravitational force, the Fe in the core is compressed. The density increases so that the electrons constitute relativistic degenerate gas.

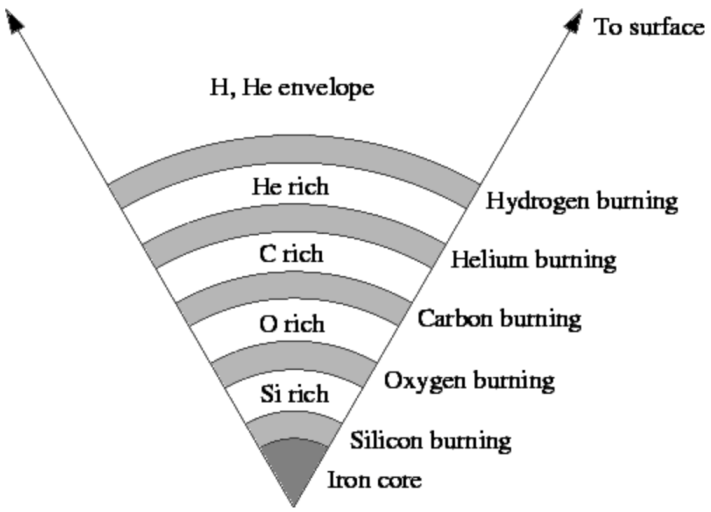

Figure 3.3. Onion-like structure of a star at the end of its life with nuclear burning stages at different layers [50].

The maximum mass for the electron degeneracy pressure of the iron core to balance the gravitational force is known as *Chandrasekhar* limit,

$$M_{Ch} = 5.8 {Y_e}^2 M_{\odot} \tag{3.1}$$

where Y_e is the number of free electrons per baryon. Above this limit the core starts to contract. Once the gravitational collapse of the core starts up, at ultra-high densities

electron capture by heavy nuclei arises, which leads the diminishing of the degenerate gas pressure against the gravitational attraction. The rise in the temperature up to 10^9 K ignites the photo-disintegration in Fe,

$$\begin{aligned} {}^{56}Fe + \gamma &\rightarrow 13\,{}^{4}He + 4n - 124.4 \text{ MeV} \\ {}^{4}He + \gamma &\rightarrow 2p + 2n + 2e - 28.3 \text{ MeV} \end{aligned} \tag{3.2}$$

where we should highlight that both reactions are endothermic and simultaneously electron capturing,

$$p + e \rightarrow n + \nu_e \tag{3.3}$$

occurs, which can not help the core to be collapsed. The core consists of mostly neutrons in this stage and hence two possible consequences with respect to neutron degeneracy pressure and gravitation await for the end of the star. If the initial mass of the star is greater than $25\mathrm{M}_\odot$, the neutron degeneracy can not resist to gravitational attraction. Therefore, the star collapses into a singularity, which is called a black-hole. It is still missing that if this black hole formation can lead to a supernova explosion. However, if the neutron degeneracy pressure defeats the gravitational attraction, the core stays as a ball of neutrons, which is so-called neutron star.

The outer layers of the star fall inward and reflect by the surface of the newly born neutron star. The velocity of this flow is much greater than the speed of sound so this creates a shock wave. And soon the resulting shock wave disrupts the star dramatically. The expansion of the wave is damped due to energy losses via dissociation of heavy elements within its path and grand neutrino production. After the time the shock stalls, there is thought to be a revived sequence which results the explosion. In final stage, inner core ultimately cools down, all the remnants are fully dispersed in the interstellar medium (ISM) and leaves newly born a neutron star or a black hole depending on the initial mass of the star.

3.4. Type Ia Supernova Explosions (SN Ia)

The basic model on SN Ia explosions are based on a carbon (C) and oxygen (O) rich white dwarf (hereafter CO WD) gaining mass from a companion and approaching a critical mass which causes the thermonuclear explosion. A nearby companion can ignite carbon fusion in the CO WD by dumping mass onto it. Accretion mass from the companion causes the CO WD to near the Chandrasekhar mass, which is also called the critical mass ($M_{Ch} \sim 1.4 M_{\odot}$). The presence of heavy elements in the SN Ia spectra can be explained by this model since the CO WDs do not contain elements lighter than C. There are variety of scenarios suggested to unveil observational features of SN Ia explosions. The proposed progenitor theories for the Type Ia SN explosions, which reproduce theoretical framework of the explosions and unveil observational features, are briefly explained in the following section. However, it should be noted that there is still no accepted progenitor theory and hence it remains as an open question.

3.4.1. Progenitor Theory

We can recall that thermonuclear explosions (Type Ia) occur when a carbon-oxygen (CO) white dwarf nears the critical *Chandrasekhar* mass. There are two basic models that explain the mass gain mechanism of the CO white dwarf, which leads to thermonuclear explosion at the end.

The first well known model is single degenerate (hereafter SD) [52]. In this SD scenario, the CO white dwarf has a non-degenerate living star as companion (See Figure 3.4). There are variety of options for the type of the donor. The companion can be a main sequence star (e.g., [54]), a subgiant (e.g., [55]), a helium star ([56]) or also a red giant ([57]). As it orbits close enough to its partner, it pulls mass (gas) from the surface of the companion star and accretes onto itself [52]. There are also different point of views for the mass transfer mechanism [58]. Roche lobe overflow is one of the proposed mechanism, where the Roche lobe is the maximum radius a star can reach before there will be a mass transfer. When this two-body system exceeds this critical radius, the material flows from the Roche lobe star to its companion via Roche lobe

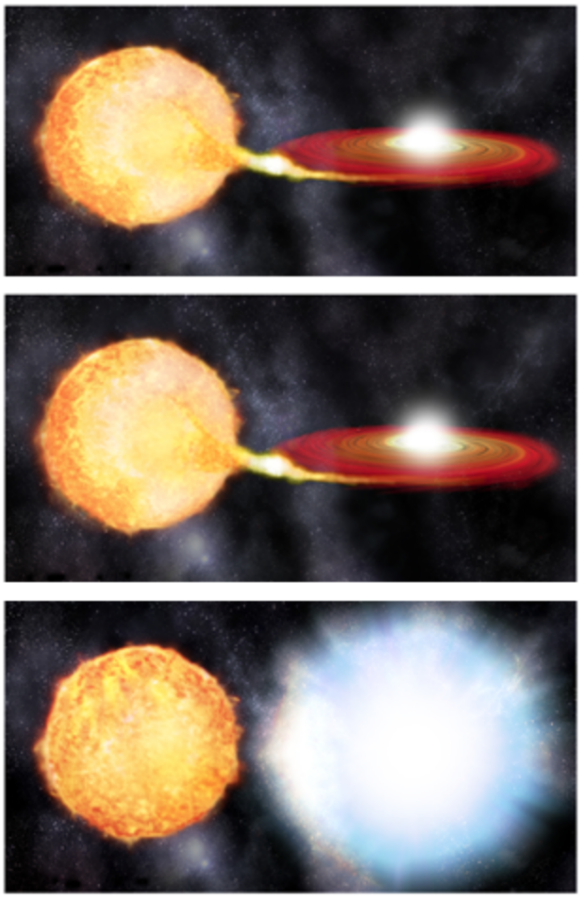

Figure 3.4. The illustration of one of the proposed progenitor theory of thermonuclear explosions, single degenerate scenario [53].

overflow (RLOF). Another possible mass transfer mechanism is via stellar winds. It is known that stars occasionally lose their masses via stellar wind, and this loss can be captured by the accretor. All these proposed configurations are still valid and have different impacts on observational outcomes.

The second proposed model is doubly degenerate (hereafter DD). In DD model, two CO white dwarfs, initially combined mass near the critical mass, orbit around each other. If this binary CO white dwarf pair is close enough, they may merge within less than a Hubble time via the emission of gravitational waves [59,60]. Another possibility is the heavier CO white dwarf disrupts the lighter companion and then accretes matter onto itself [61]. The recent accepted explanation is that when one of them exceeds the

Roche-lobe radius, the permission to accrete material is ignited. The stable or unstable nature of the mass transfer between two CO white dwarfs depends on the initial mass ratio. If the mass difference between primary and secondary is large, transfer happens to be smooth. The best ratio for stable transfer is determined as 2/3 [62]. In this content, it has similar procedure as in SD scenario due to the stable nature of mass transfer, primary CO white dwarf accreting mass onto itself and explosion. However, if the masses of primary and secondary CO white dwarfs are comparable, the transfer is so unstable. When one of them starts the accretion, the tidal forces becomes so effective on the secondary CO white dwarf and forms a hot thick accretion disk around the primary CO white dwarf. The very high accretion rate causes to ignite carbon on the surface and the primary white dwarf turns into an oxygen-neon white dwarf. Some studies claim that the fate of this oxygen-neon white dwarf is to collapse to a neutron star (e.g., [63, 64]).

Likewise, for the explosion constituents, the propagation of ignited flame is also under discussion. It is clear that the first stage of the explosion starts with C burning. The extreme dense core of CO white dwarf, 10^9 g cm^{-3}, allows this burning as thermal runaway. The proposed mechanisms for the propagation of burning fronts are *deflagration* and *detonation*. Deflagration refers that the front propagation is mediated by thermal conduction at subsonic speed, whereas detonation offers that the front propagation is mediated by shock compression at supersonic speed.

Pure detonation model [65] is ruled by the detection of intermediate-mass elements in the SN Ia spectra, since this model predicts the productions of Fe group elements only. The problem was that the supersonic propagation of burning front incinerate the whole star at very high density and leaves only Fe group elements. On the other hand, the 1D pure deflagration models (such as W7 & W70) give promising results, if the turbulent flame accelerates up to 30% of the speed of sound. Moreover, the combination of detonation and deflagration is also in use as delayed detonation models or the deflagration-detonation transition (hereafter DDT) models (e.g. [66, 67]). This model starts with the initial slow burning (deflagration), which is a requirement to expand at small densities, and follows by a supersonic combustion to produce intermediate-

mass elements. Although, the 1D delayed detonation simulations come up with better results than the pure deflagration, there are still many missing parts of the model.

Therefore, the underlying nature of Type Ia SNe is an intriguing phenomenon in astrophysics and yet virial radial observations have great importance to address all of these issues. It is acknowledged that different types of SN have different progenitors, leading different amount of heavy elements dependent on the effective time-scale during the chemical evolution of galaxy clusters. Due to the theoretical uncertainties mentioned above, this work considers as many SN yields in literature as possible to unravel the observational outcomes.

3.5. The applied supernova yields

The SN yields adopted for our work is represented in Table 3.1. We compare the fits of different models and investigate the best model that represents chemical enrichment history of Abell 3112 galaxy cluster. The very brief instructive definition of the models are listed below.

- Pure deflagration models of SN Ia are W7 & W70.

- The delayed-detonation models are WDD1, WDD2, WDD3 & CDD1, CDD2, CDD3, where the numbers represent the density in the time of the transition (in units of 10^7 g cm^{-3}); the C refers the central density at 1.37 $\times 10^9$ g cm^{-3}, and W infers the central density at 2.12 $\times 10^9$ g cm^{-3}.

- A pure deflagration model with a global spherical symmetry, where the deflagration is ignited within the c3-shape boundary, is C-DEF.

- A delayed detonation model with the 2D spherical deflagration C-DEF is C-DDT.

- An off-center delayed-detonation explosion (O-DDT), where the ignition is slightly shifted from the WD center.

Table 3.1. The literature view of SN yields used in this analysis.

Model	C	N	O	F	Ne	Na	Mg	Al	Si	P	S	Cl	Ar
SN Type II (10-50$M_{\odot}$) (Table 3; [68])	0.0793	0.00156002	1.80461	1.16e-09	0.23138	0.00651	0.1228	0.0148	0.12204	0.00121	0.0411998	0.0001198	0.00799002
W7 (Table 3; [68])	0.0483014	1.16132e-06	0.143	5.67e-10	0.00451846	6.32e-05	0.0085723	0.000986	0.156598	0.000357	0.0870044	0.0001737	0.01565
W70 (Table 3; [68])	0.0508	4.461e-07	0.133	1.37e-10	0.00229005	1.41e-05	0.0158004	0.000113	0.142129	9.12e-05	0.0914781	1.616e-05	0.0191007
WDD1 (Table 3; [68])	0.00542051	0.000284999	0.0882045	1.7e-09	0.0014526	8.77e-05	0.0076948	0.000438	0.273577	0.000238	0.163034	0.0001222	0.03233
WDD2 (Table 3; [68])	0.00899033	0.000269532	0.0658052	4.5e-10	0.00104439	2.61e-05	0.0045225	0.000247	0.206981	0.00016	0.124232	9.33e-05	0.02509
WDD3 (Table 3; [68])	0.0166003	0.000182121	0.0558038	2.3e-10	0.00128172	3.01e-05	0.0026609	0.000141	0.158601	0.000107	0.0952941	7.04e-05	0.019444
CDD1 (Table 3; [68])	0.00993085	9.0853e-05	0.0934012	5.83e-10	0.00160463	5.1e-05	0.0078181	0.000445	0.278602	0.00024	0.166041	0.0001189	0.033
CDD3 (Table 3; [68])	0.00508042	9.0547e-05	0.0583012	4.24e-10	0.00081799	3.5e-05	0.0042622	0.000235	0.198936	0.000152	0.119079	8.67e-05	0.024326
W7 (Table 2; [69])	0.0499	1.11e-06	0.14	7.19e-10	0.00428	6.59e-05	0.0163	0.0010	0.167	3.86e-04	0.0797	1.38e-04	0.0131
CDEF (Table 2; [69])	0.364	1.54e-06	0.427	1.04e-09	0.0251	1.59e-04	0.00992	7.23e-04	0.0519	1.91e-04	0.0198	4.15e-05	0.00294
CDDT (Table 2; [69])	0.0121	1.15e-06	0.376	1.54e-09	0.0113	2.07e-04	0.059	0.00322	0.338	0.00136	0.119	3.69e-04	0.0162
ODDT (Table 2; [69])	0.00349	2.8e-07	0.151	2.7e-10	0.00413	5.87e-05	0.0216	0.00117	0.287	5.91e-04	0.127	2.2e-04	0.022

Table 3.1. The literature view of SN yields used in this analysis (cont.)

	K	Ca	Sc	Ti	V	Cr	Mn	Fe	Co	Ni	Cu	Zn
SN Type II (10-50$M_{\odot}$) (Table 3; [68])	6.737e-05	0.00586868	2.29e-07	0.00013157	1.00007e-05	0.00131542	0.000386	0.09074	7.27e-05	0.0059725	1.244e-06	1.89291e-05
W7 (Table 3; [68])	7.841e-05	0.0119363	2.21e-07	0.00034291	7.49155e-05	0.008479	0.00887	0.74903	0.00104	0.125722	3.004e-06	2.82332e-05
W70 (Table 3; [68])	2.153e-06	0.0181139	3.85e-08	0.000420697	4.27122e-05	0.0092665	0.00666	0.77516	0.000968	0.100182	3.833e-06	7.63786e-05
WDD1 (Table 3; [68])	7.303e-05	0.031047	2.49e-07	0.00112867	0.00013301	0.020504	0.00848	0.67183	0.000395	0.038152	3.478e-06	2.60194e-05
WDD2 (Table 3; [68])	6.122e-05	0.0243569	2.09e-07	0.00101866	0.000116009	0.017033	0.00705	0.79203	0.000625	0.058679	6.92e-06	9.59431e-05
WDD3 (Table 3; [68])	4.882e-05	0.0188679	1.76e-07	0.00092105	0.000102009	0.014354	0.00616	0.87034	0.000775	0.072684	9.3e-06	0.000162321
CDD1 (Table 3; [68])	6.91e-05	0.0318435	2.47e-07	0.000818193	0.000111005	0.01877	0.0081	0.647963	0.000291	0.0350035	7.28e-07	4.71477e-06
CDD3 (Table 3; [68])	5.765e-05	0.0238601	2.02e-07	0.00074695	0.000109012	0.016468	0.00677	0.83446	0.000635	0.0618363	6.02e-06	0.00010077
W7 (Table 2; [69])	6.45e-05	0.00976	1.33E-07	3.94e-04	4.04e-05	0.00528	0.00672	0.761	8.29e-04	0.119	2.55e-06	3.8e-05
CDEF (Table 2; [69])	1.82e-05	0.00205	2.55e-08	9.97e-05	2.15e-05	0.00357	0.00735	0.389	8.2e-04	0.0842	8.45e-07	1.01e-05
CDDT (Table 2; [69])	1.71e-04	0.00691	2.38e-07	2.08e-04	2.95e-05	0.00352	0.00595	0.36	6.7e-04	0.075	7.82e-07	8.82e-06
ODDT (Table 2; [69])	1.31e-04	0.017	2.29e-07	8.72e-04	6.52e-05	0.0104	0.00735	0.651	6.36e-04	0.0805	2.13e-06	3.5e-05

3.6. A Robust Model to Constrain Supernova Fractions (SNAPEC)

The hot gas in ICM is a grand reservoir of metals produced by SN explosions. Spatially resolved X-ray spectra from intracluster medium permit to stack metal content of the ICM. It is known that Fe and Ni are mainly synthesized by SN Ia, whereas O, Ne and Mg are predominantly produced by SN cc explosions. Si-group (Si, S, Ca and Ar) or the so called α elements are produced by both types of SN explosions in similar portions. The precise combination of present observational data with various theoretical predictions of SN yields requires special care due to large uncertainties.

snapec is a recently developed XSPEC model [70, 71]. A unique feature of the model is that *snapec* calculates the total number of SN explosions and measures the spatial distribution of the ratio of SN Ia to SN cc by directly fitting the X-ray spectra. The model calculates the mass of the ith element (M_i^{SNe}) as,

$$M_i^{SNe} = N^{Ia} y_i^{Ia} + N^{cc} \langle y_i^{cc} \rangle \tag{3.4}$$

where the number of SN explosions N^{Ia} and N^{cc} and the yields y^{Ia} and y^{cc} of SN Type Ia and SN core-collapse are given respectively. If we denote the number ratio of SN Ia to SN cc as R and the total number of SN explosions as $N^{SNe} = N^{Ia} + N^{cc}$, we may rewrite the Equation 3.4 as,

$$M_i^{SNe} = N^{SNe}(1+R)^{-1}(R y_i^{Ia} + \langle y_i^{cc} \rangle). \tag{3.5}$$

The given mass range for SN II yields on Table 3 from [68] uses Salpeter Initial Mass Function (hereafter IMF) averaged SN II yields. The assumption of Salpeter IMF indicates that,

$$\langle y_i^{cc} \rangle = \frac{\int_{10M_\odot}^{50M_\odot} y_i^{cc}(m) m^{-\alpha} dm}{\int_{10M_\odot}^{50M_\odot} m^{-\alpha} dm}. \tag{3.6}$$

where the slope $\alpha = 2.35$ for Salpeter IMF [72].

snapec model has five set of free parameters: electron temperature (kT_e), total number of SNe (N^{SNe}) responsible for the enrichment of the ICM, the percentage of SN Ia contribution (R) in the extracted region, the cluster's redshift and *apec* normalization factor (see Equation 2.8). Moreover, two additional SN Ia model index and SN II model index parameters are required to specify the models of which SN yields to be used in calculations.

The advantages of this model are that it fits the spectrum with *apec* simultaneously so that provides a single set of diminished uncertainties and it is straightforward to include or exclude yields available in literature.

4. X-RAY INSTRUMENTS

The astronomical X-ray sources have energy ranges between 0.1 keV to several tens of keV, where the incoming radiation is blocked by even the thin layers of earth's atmosphere due to atmosphere's opacity. Figure 4.1 illustrates the attenuation of the incoming photons in different energy ranges. This brings limitations for X-ray measurements and limits all the ground based experiments. Therefore, the most efficient way of X-ray observations is to use X-ray satellites located in the Earth's orbit.

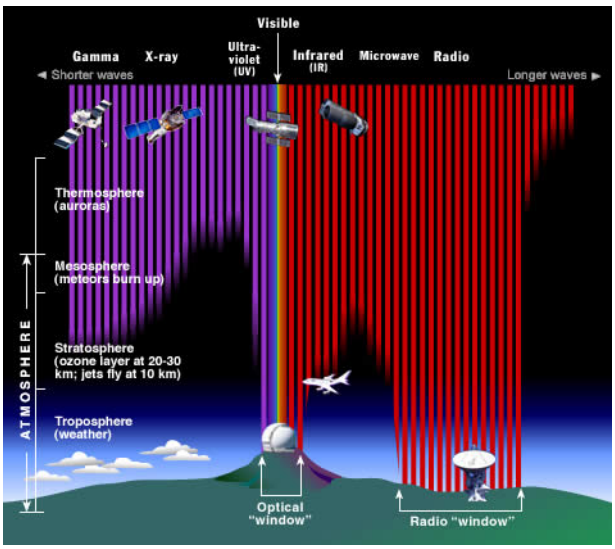

Figure 4.1. The deposition depth of the incoming sources into the Earth's atmosphere [73].

The main working principle of X-ray satellites is to collect the incoming photons by using the grazing incidence telescope to focus and charged-coupled devices (CCD) in the focal plane to determine the energy, position and arrival time of each photon. The measured energy and spatial information of incoming photons do not directly give the distribution of the source since the instrumental response should also be taken into account. All these fundamental components build up the so-called spatially resolved X-ray spectroscopy. As for now, there are many onboard X-ray observatory satellites in use, in this thesis we currently focus on two main operating observatories, *Suzaku* and *Chandra*.

4.1. *SUZAKU* Satellite

Astro-EII is a joint Japanese-US mission X-ray astronomy satellite, designed to detect various X-ray sources with high sensitivity over a spread energy range from 0.2 to 600 keV. It was launched by Japan Aerospace Exploration Agency (JAXA) with the M-V launch vehicle from JAXA's Uchinoura Space Center (USC) on 2005 July 10, right after renamed as *Suzaku*, a red bird guarding the sky in Asian mythology [74]. It has a near circular orbit with 96 minutes long period. It is located at 570 km altitude with 31° inclination angle. Figure 4.2 shows the schematic view of *Suzaku* in orbit.

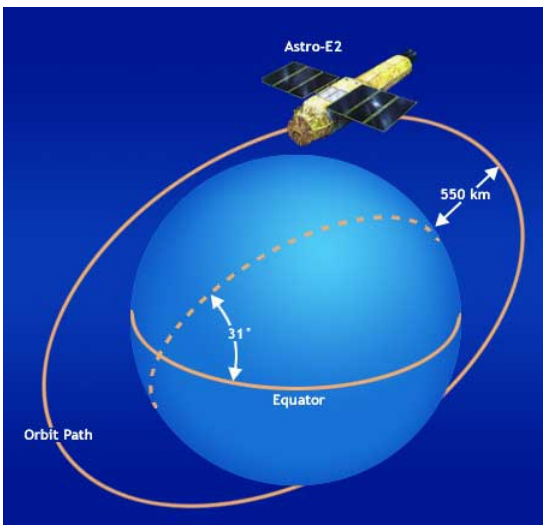

Figure 4.2. An illustrative view of *Suzaku* satellite in near circular orbit [75].

The technical details of *Suzaku* satellite is taken from *The X-ray Observatory Suzaku Guide* [74] and summarized in details.

- The total mass at launch was 1706 kg. The spacecraft length along the telescope axis is 6.5 m after the deployment of extensible optical bench (EOB).

- Three gyroscopes and two star trackers measure the spacecraft attitude regularly. The position is stabilized by four sets of wheels, where one is redundant.

- The electronic boxes of both scientific instruments and the spacecraft bus are located in the side panels.

- *Suzaku* has two wings of solar array paddles (SAP). Total power provided by solar paddles is $\sim$ 660 W. The pointing accuracy is $0.24'$. Power constraint of the solar paddle results 65° – 115° limitation from the Sun. Therefore, except the objects near the orbital pole, any part of sky is observed at least twice a year.

- The mean efficiency of the satellite is about 43%. South Atlantic Anomaly (hereafter SAA) interrupts the operations and this causes decrease in efficiency. The SAA is the area near Brazil which has an anomalous magnetic field. Thus the area contains many charged particles hitting the detectors and the provided solution is to exclude the data from this area.

- At higher altitudes, proton flux contaminates the CCDs and causes serious instrumental background in general. In the case of *Suzaku*, the charged particle background is very low and stable due to being in low altitude.

Suzaku is equipped with three on-board instruments; X-Ray Imaging Spectrometer (hereafter XIS) consisting of four X-Ray Imaging CCD cameras located in the focal plane of X-Ray Telescope (hereafter XRT), Hard X-Ray Detector (HXD) which is a non-imaging instrument that aims to increase the energy bandpass, and X-Ray Spectrometer (XRS) which is no longer active due to a meteoroid hit. For this work, spatially resolved X-ray spectroscopy is performed using XIS device. Hence, our main focus is on this instrument.

4.1.1. Telescope: X-Ray Telescope (XRT)

Observing high energy photons are not trivial due to penetrating nature of those particles. Therefore, some advanced telescopes are required to guide and focus X-rays onto the detector. XRT is a thin-foil nested Wolter-I type telescope, see Figure 4.3. In space observations, Wolter-I type telescopes provide advantages such as compactness

and free space for nested objects. In *Suzaku*, there are four XRTs (XRT-I) corresponding to each CCD and there is also XRT-S with shorter focal length to be used on the high resolution spectrometer. However, XRT-S is no longer in use due to cryogenics problems occurred in the system. The mirrors, which are used to reflect X-Rays at small grazing angles (<1°), are made of thin-foils. In *Suzaku*, each XRT consists of 175 nested mirrors per quadrant. These layers are called to be partially Wolter-I type, due to the geometrical reasons. Thin-foil layers can not perfectly construct Wolter-I type telescope so that cylindrical section of a cone is usually taken as an approximation.

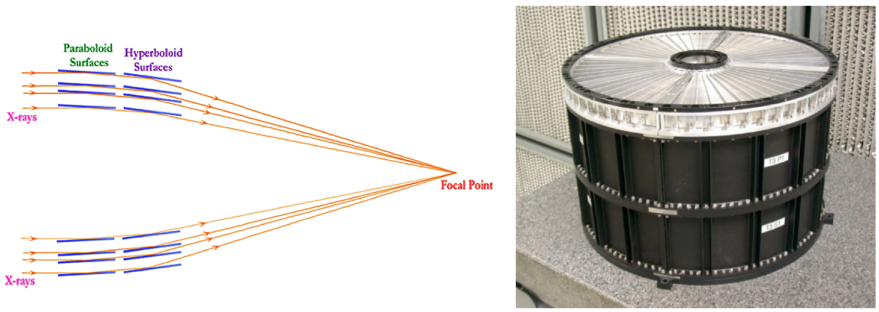

Figure 4.3. Left Figure: An illustrative slice of Wolter Type-I mirror. Incident X-Rays are reflected twice by mirrors sequentially and concentrated at the focal point. Right Figure: A *Suzaku* X-Ray Telescope [76].

Nested layers provide large effective collecting area. However, conical approximation limits the angular resolution. Another important aspect is the smoothness of the reflective surface. Replication technique was preferred to construct smooth reflective surface [78]. XRT has gold coated front surface onto aluminium substrate. The spatial resolution is constraint to $1'$. The field of view is about $17'$ at 1.5keV and $13'$ at 8keV. XRTs' good angular/imaging resolutions with $0.1'$ uncertainty are in the range of $1.8'$ to $2.3'$.

4.1.2. CCDs: X-Ray Imaging Spectrometer (XIS)

It has great importance to understand working principle of these charged-coupled devices for X-ray analysis. A CCD is comprised of an array of linked ("coupled") capacitors. When an incident photon interacts within the semiconductor subtrate (depletion

layer), it is converted into a cloud of electrons whose total charge is proportional to the incoming photon energy. Applied electric field (clock voltages) between the gates creates potential wells and these electrons are then concentrated and stored into the pixels. Three-phase (self-induced drift, thermal diffusion, and fringing field drift) electric potential clocking yield to transfer these packets of charges to the neighbouring gates and finally to the read-out node.

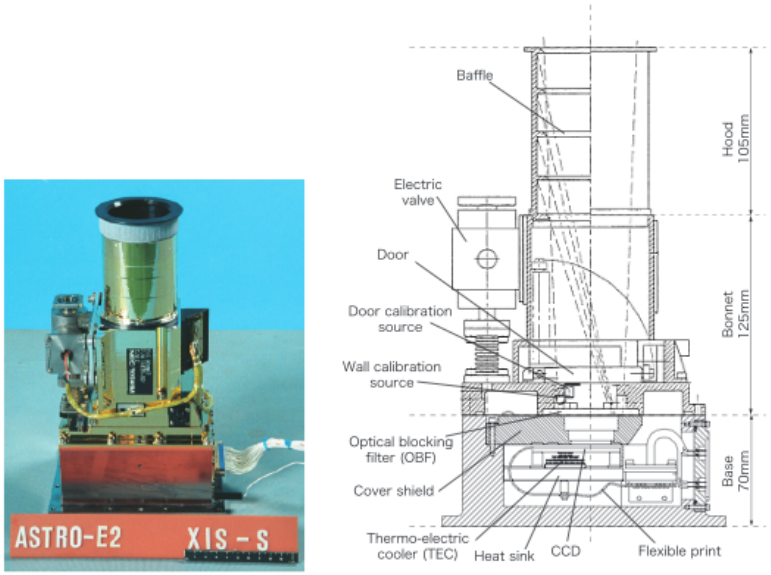

Figure 4.4. Left Figure: XIS sensor (CCD+Camera Body) [79]. Right Figure: Cross Section of XIS sensor [79].

Suzaku has four X-Ray Imaging Spectrometers (XIS0, XIS1, XIS2 and XIS3) and each located in the focal plane of an XRT (XRT-I0, XRT-I1, XRT-I2 and XRT-I3) respectively. A sample of XIS and its schematic cross section are shown in the Figure 4.4. Each spectrometer employs a single MOS-type X-Ray sensitive silicon CCD chip operating in photon-counting mode [79].

XIS1 CCD is a back-illuminated (hereafter BI) type and it covers the energy range of 0.2 to 12 keV, whereas the rest (XIS0, XIS2 and XIS3) is front-illuminated (hereafter FI) CCDs and has a range of 0.4 to 12 keV. The front gate structure of the FI CCDs, made of thin Si (thickness of 0.28 μm) and SiO2 (thickness of 0.44 μm) layers, limits the sensitivity to soft X-rays, while the very thin surface dead layers of

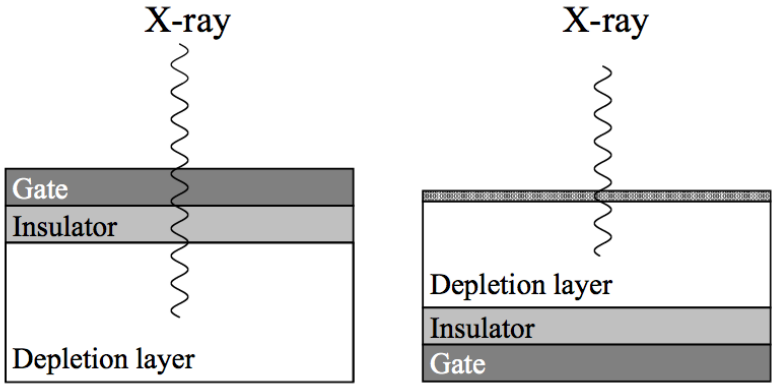

Figure 4.5. Difference in photon interaction path for FI and BI CCDs.

the BI CCD, consisting of 5nm HfO2, 1nm Ag, and 3nm SiO2, prevents sensitivity to hard X-rays.

Figure 4.5 reveals that absence of gate structural layers in BI CCDs gives opportunity to measure even low energetic photons and gain high quantum efficiencies for particles below $\sim$ 1 keV. Due to longer path for incoming particles, FI CCDs have high quantum efficiencies for high energy photons. Quantum Efficiencies (QE) of XIS CCDs, which is the detection percentage of incoming photon producing charge cloud in the sensitive area, are given in the Fig 4.6. The efficiency is calculated through the best estimate values of the thickness of dead layers and depletion layers.

^{55}Fe are used as calibration sources, of which are located on a side wall of the bonnet. The main property of ^{55}Fe is to decay ^{55}Mn, which produces 5.899 and 5.88 keV (Kα1 and Kα2) and 6.490 keV (Kβ) lines with a half-life of 2.73 years. Since these sources illuminate two far corners from the read-out nodes, they have to be taken into consideration during data analysis.

XIS CCDs are sensitive to photons in wide energy range. Therefore, optical block filters (OBF) are laid on 20 mm above of each CCD to block both optical and UV photons. These filters are made of polyimide ($C_{22}H_{10}N_2O_4$) film, thickness $\sim$ 1400 $\mathring{A}$, with vapour-deposited Al on both sides.

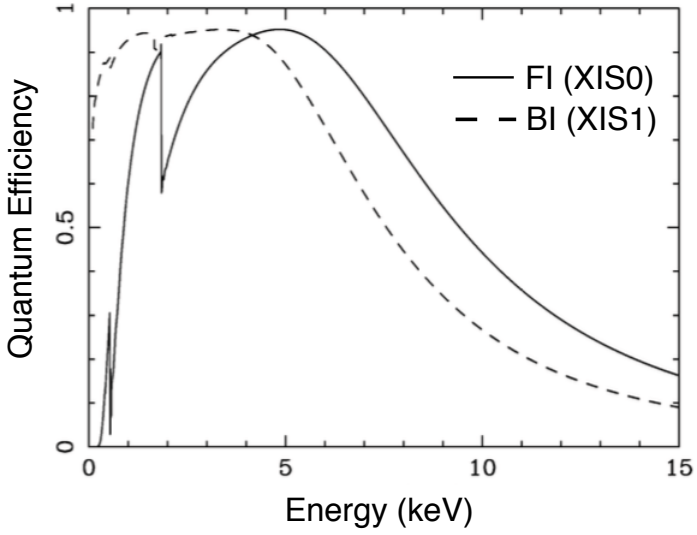

Figure 4.6. The QE as a function of incident energy is shown [79]. The black line represents the FI CCD (XIS0) and the red line is for the BI CCD (XIS1).

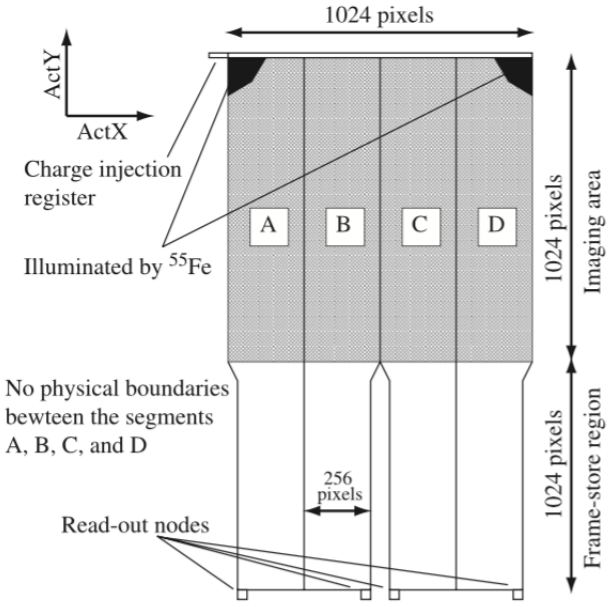

Figure 4.7. Top schematic view of the XIS CCD. It has four segments (A, B, C, and D), each with a dedicated read-out node [79].

Table 4.1. *Suzaku* XIS CCD parameters with combined effects of OBF and XRT.

Item	Value
Field of View	$18' \times 18'$
Energy Range	0.2 – 12 keV
Format	1024×1024 pixels
Pixel Size	24μm × 24μm
Energy Resolution	130 eV (FWHM) at 5.9 keV
Effective area	330 cm^2 (FI)/370 cm^2 (BI) at 1.5 keV 160 cm^2 (FI)/110 cm^2 (BI) at 8 keV
Readout noise	∼2.5 electrons (RMS)
Time Resolution	8 s (Normal) - 7.8 ms (Parallel Sum Clocking)

In summary, *Suzaku* with its low orbit provides low and stable background and makes it sufficient to probe objects with low surface brightness such as outskirts of the galaxy clusters. The combined parameters of XIS CCDs with OBF and XRT are summarized in the Table 4.1 [79].

4.2. *CHANDRA* Satellite

Chandra is NASA's X-ray observatory, designed to detect distinctive X-ray sources with high resolution within 0.1 to 10.0 keV energy range. The satellite was launched from Cape Canaveral on 1999 July 23, as being the NASA's flagship mission for X-ray astronomy. By a built-in propulsion system, the spacecraft was boosted to an unusual high Earth elliptical orbit with 64 hours and 18 minutes period. It is located at an altitude of approximately 139,000 km with 76.7° inclination angle. Figure 4.8 shows the schematic view of *Chandra* in orbit.

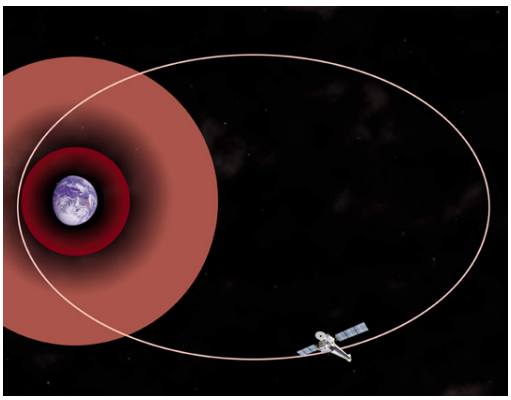

Figure 4.8. An illustrative view of Chandra satellite in high Earth elliptical orbit [80].

The technical details of *Chandra* satellite is taken from *Chandra X-ray Observatory Guide* and summarized in details.

- The total mass at launch was 4,790 kg. The long focal length of the telescope requires the spacecraft length along the telescope axis to be 12 m.

- The position is balanced with the momentum unloading thrusters, by which the control of *Chandra*'s altitude is provided.

- Solar arrays provide total power, which is $\sim$ 2350 W. Thereafter this energy is stored in three banks of batteries and distributed to the Observatory.

- The mean efficiency of the satellite also depending on the solar activities is between % 65 and %70. Charged particle background interrupts the data quality so that the data is not available at the location of the satellite above the radiation belts, which covers % 75 of the orbital period. However, as an advantage, two days lasting observations are possible.

Chandra is equipped with four on-board instruments; Advanced CCD Imaging Spectrometer (hereafter ACIS) which provides a good spectral resolution, whereas High Resolution Camera (HRC) is responsible for high spatial resolution. Two transmission grating spectrometers, the High Energy Transmission Grating (HETG) and the Low Energy Transmission Grating (LETG), are also in operation to improve spectral resolution. In this thesis, the data taken from ACIS will be in use so we will only focus on ACIS instrument.

4.2.1. Telescope: High Resolution Mirror Assembly (HRMA)

The HRMA is a Wolter Type-I design telescope comprised of nesting concentric X-ray mirror segments, where the nested segments are to enlarge the collecting area. The mirror elements are fabricated from Zerodur glass due to its low coefficient of thermal expansion and ability of producing very smooth polished surfaces. All the mirror elements are also coated with iridium.

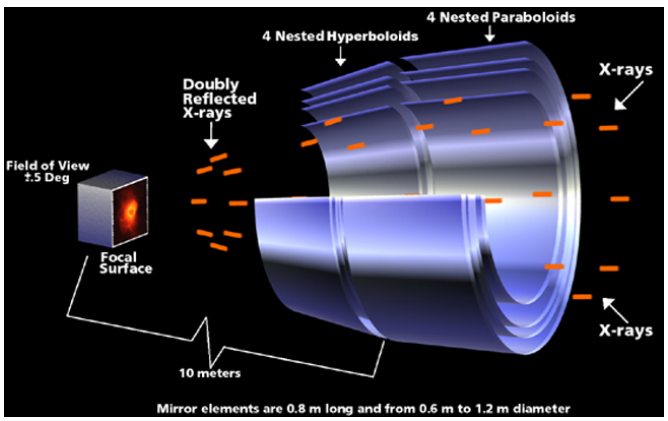

Figure 4.9. A schematic cross sectional view of HRMA showing four nested concentric mirrors and the location of the focus [81].

As can be seen from the Figure 4.9, the focal length is 10 m and the total length of the assembly is 2.76 m covering pre to post collimator. Outer diameters are extended from 1.23 to 0.65 m. The most important gain is the half width at half maximum (HWHM) of the point spread function (PSF) for HRMA, which is $0.5''$, the same size as a pixel in the ACIS. This gain offers to measure source positions with $0.5''$ accuracy.

4.2.2. CCDs: Advanced CCD Imaging Spectrometer (ACIS)

ACIS composes of ten planar CCDs with 1024 × 1024 pixel sizes. The layout of the CCDs are divided into two types, ACIS-I and ACIS-S chips. Four CCDs tangent to the focal surface are designed as 2 × 2 array and it is called "ACIS-I" chip. The primary use of the ACIS-I chip is imaging. The other six CCDs are constructed as 1 × 6 array and it is called "ACIS-S" chip. The purpose of the ACIS-S chip is to make measurements in both imaging and grating read-out. The ACIS in total has the opportunity to determine high resolution spectra and moderate resolution spectra simultaneously.

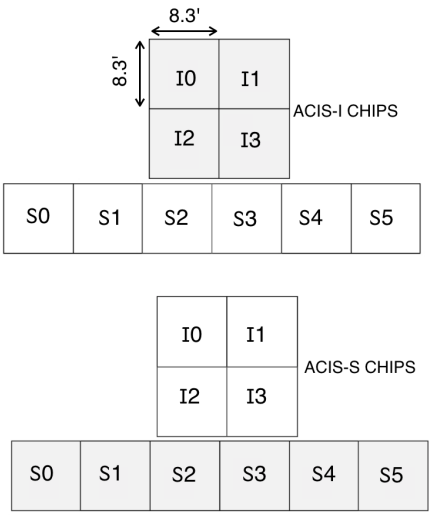

Figure 4.10. A schematic drawing of ACIS-I and ACIS-S chips [82].

Figure 4.10 shows the schematic view of *Chandra* ACIS chips. ACIS-I chips are composed of FI CCDs, while two of the ACIS-S chips (S1 and S3) are BI type. Quantum efficiencies of ACIS CCDs are FI chips are bigger than %30 between 0.7 and 11.0 keV and the same efficiency is reached by the BI CCDs between 0.4 and 10.0 keV (see Figure 4.11). The efficiency is calculated through the best estimate values of the thickness of dead layers and depletion layers.

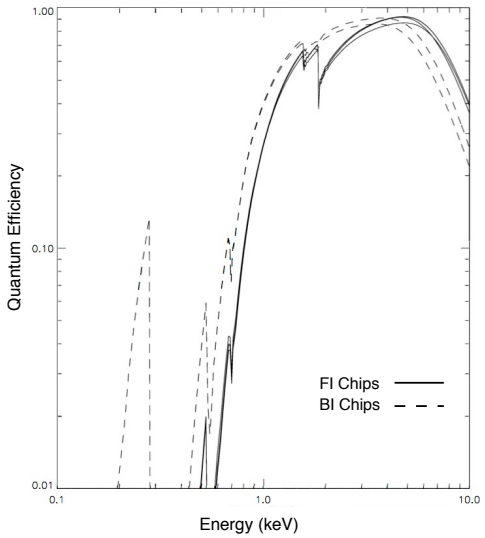

Figure 4.11. The QE as a function of incident energy is shown [82]. The solid line represents the FI CCDs and the dashed line is for the BI CCDs.

To prevent from the radiation from UV and optical lights, the ACIS-I and S chips are shielded by polyamide layers with a layer of aluminium coated on each side. In summary, very high spatial resolution with small PSF (0.5″) of *Chandra* provide excellent sensitivity to distinguish between point sources from cluster's emission. Hence, we use overlapping *Chandra* observations for point source detection. Most of the characteristics of *Chandra* ACIS chips are summarized in Table 4.2.

Table 4.2. *Chandra* ACIS CCD parameters combined with HRMA.

Item	Value
Field of View	ACIS-I:16.9′ × 16.9′ ACIS-S: 8.3′ × 50.6′
Energy Range	0.2 - 12 keV
Format	1024×1024 pixels
Pixel Size	24μm × 24μm
Readout noise	∼2.0 electrons (RMS)
Time Resolution	3.2s (Normal)

5. OBSERVATIONS AND DATA REDUCTION

5.1. Observations

Abell 3112 was observed with *Suzaku* with five different pointings between May 2008 and Dec 2014.[1] Table 5.1 gives detailed information on the data analyzed in this thesis. It would be good to mention that the awarded observations taken between 2013 and 2014 aiming to provide information on chemical enrichment history of the Universe have been analyzed and successfully completed in this thesis.

5.2. The Basic Data Reduction of *Suzaku* Observations

The unfiltered *Suzaku* data are analyzed by using HEASOFT version 6.17 and the latest calibration database (CALDB) as of November 2015. The details of the *Suzaku* data reduction are as follows:

- The FTOOL *aepipeline* is used to reprocess the unfiltered event data files using the latest calibration and screening criteria [84]. Additionally, we require elevation angles above 5° and 20° for the night and day Earth rim and the geomagnetic cut off rigidity of > 6 GV. The data taken when the satellite passes through the regions affected by South Atlantic Anomaly (SAA) and the ^{55}Fe calibration sources at two far corners of CCD chips are excluded from the analysis. The event files in the 3×3 and 5×5 editing modes are combined.

- We precisely check all the light curves to distinguish our data from background flares.

- For observations taken in 2013, one-eight of XIS0 detector due to micro-meteorite hit in June 2009 is also excluded.

[1] The materials in this chapter are based on the work [83].

Table 5.1. *Suzaku* and *Chandra* observations of Abell 3112.

Instrument	Obs. ID	Pointing	RA (J2000)	Dec (J2000)	Observation Date	Exp. XIS0/XIS1/XIS3 (ks)	Filtered Exp. XIS0/XIS1/XIS3 (ks)	PI
Suzaku XIS	803054010	On-axis	49.478	-44.248	2008 May 23	67.5/67.5/67.5	54.9/54.9/54.9	M. Bonamente
	808068010	On-axis	49.498	-44.251	2013 Jun 23	119.1/119.1/119.1	113.5/113.5/113.5	E. Bulbul
	808068020	On-axis	49.497	-44.236	2013 Jun 25	65.4/65.4/65.4	54.4/54.4/54.4	E. Bulbul
	809116010	Offset	49.354	-44.489	2014 Dec 09	107.9/107.9/107.9	87.3/87.3/87.3	E. Bulbul
	809116020	Offset	49.354	-44.449	2014 Dec 12	97.9/97.9/97.9	80.4/80.4/80.4	E. Bulbul
Chandra ACIS-I	13135	On-axis	49.481	-44.258	2011 Mar 14	42.8	42.2	S. Murray
	6972	Offset	49.421	-44.410	2006 Apr 18	30.2	29.7	M. Markevitch

- An additional correction for the comparable fraction of flickering pixels is applied to the data which are taken after January 2014 [85].

- Besides main procedure of data reduction, we also apply filtering on point sources, which contaminate the cluster emission measure. The advanced cleaning technique from point sources is explained in detail in Section 5.4.

- The total filtered exposure time of *Suzaku* XIS0/XIS1/XIS3 is 390.5/390.5/390.5 ks respectively. 67.3 ks of the exposure time is lost through our strict filtering procedure.

5.3. The Basic Data Reduction of *Chandra* Observations

To detect X-ray point sources unresolved by *Suzaku*, we use the two overlapping *Chandra* pointing of the cluster. *Chandra* archived ACIS-I data are cleaned by using *Chandra* analysis software CIAO version 4.7, with CALDB version 4.6.7. The details of the *Chandra* data reduction are as follows:

- *Chandra* ACIS-I data are filtered from background flares using LC_CLEAN.

- The filtered light curves are confirmed not to show left-over significant background flares.

- The total filtered exposure time is 71.9 ks.

5.4. The Unresolved Point Sources

We use the two overlapping *Chandra* observations (both on-axis and offset) to detect X-ray point sources unresolved by *Suzaku*. The PSF sizes of *Suzaku* and *Chandra* are quite different. Therefore, the extents of the point sources detected by *wavdetect* using *Chandra* observations can not be used directly to exclude point sources in the *Suzaku* FOV. We use the same procedure described in detail in [86] to determine a

conservative exclusion radii for point sources detected by *Chandra* pointings.

The background image is extracted from the blank-sky observations. To account for variations in the particle background, we use count rates detected in the 9 - 12 keV band to match Abell 3112 observations as described in [87]. The CIAO's *wavdetect* tool is used to determine the locations of the point sources in the FOV. Point sources are identified by running *wavdetect* tool with source threshold parameter at 10^{-6} corresponding to one spurious source in a 1000 $\times$1000 pixel map and the scanned list of radii are 2.0, 4.0, 6.0, 8.0, 16.0 pixels, where these scales correspond to the radius of the core of the Mexican hat function. Then we extract the spectrum of each point source using the *specextract* tool in CIAO. The spectrum of the source is fitted with an absorbed power-law with a fixed index set to 1.4 and variable normalization from [88],

$$S_{CXB} = phabs * powerlaw. \tag{5.1}$$

We compare the flux of each point source in 0.5 and 2.0 keV energy band. We select the brightest point source in the *Suzaku* FOV (J2000; R.A.: 49.342°; DEC: -44.173°), which is located in a fairly faint region of the cluster (shown in the green circle in Figure 8.1).

We then simulate *Suzaku* observations of the point source based on the best-fit flux (3.47×10^{-5} photons keV^{-1} cm^{-2} s^{-1}) and power-law index obtained from the *Chandra* observations using the FTOOL *xissim*. To estimate the effect of the point source contamination to the surrounding cluster ICM gas, we add simulated diffuse emission to the spectrum with a total net counts of 2000. Our goal is to measure the plasma temperature with better than $< 20\%$ accuracy in these simulations. We extract the spectrum around the point source with incremental extraction radii to determine the radius where the cluster emission is not affected by the point source contamination.

It is given in Figure 5.1, we find that excluding $r > 40''$ around the point source has a minimal effect on the cluster plasma temperature, abundance, and normalization. Since this point source is in a faint region of the cluster and all our spectra include

at least 10^4 counts, the exclusion radius of $40''$ is a conservative estimate for all point sources detected by *Chandra* observations in the *Suzaku* FOV.

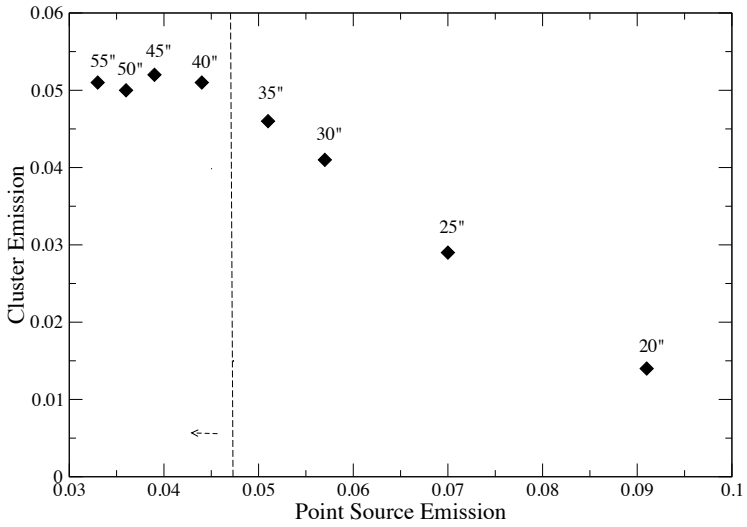

Figure 5.1. The use of *Chandra* overlapping observations is to detect point sources that contaminate the cluster emission. The optimum radius of extraction is chosen $40''$.

6. THE BACKGROUND

6.1. Introduction

The Suzaku XIS CCDs are affected by four different background components: i) non X-ray background; ii) solar wind charge exchange; iii) cosmic X-ray background; iv) soft foreground.[2] While X-ray background is produced via the interaction within the XRT field-of-view (FOV), non X-ray background causes indirect production of X-rays via the interaction of the charged particles or γ rays hitting onto the detector from any directions. It is essential to note that the non X-ray background is the only background that can be directly subtracted from the observed spectrum, whereas the rest of the background components must be modelled. Therefore, we use the most powerful tool to model the cosmic X-ray background, solar wind charge exchange and soft foreground by a joint fit of ROSAT All Sky Survey data (RASS) and local background extracted beyond R_{200} region. The best-fit parameters are given in Section 6.3.

6.2. The Background Components

6.2.1. Non X-ray Background

Suzaku XIS CCDs are designed to collect X-rays in energy range 0.2 - 12.0 keV so that they are sensitive to any photons satisfying this condition. Therefore, the fake X-ray signals produced by the charged particles or γ rays are also recorded by XIS and these are the primary constituents of the so-called non X-ray background (NXB). The location of the satellite due to the radiation environments determines the amount of NXB that CDDs are exposed to. The low altitude design of *Suzaku* satellite gives great advantageous of low and stable intensities of charged particles and γ rays.

Suzaku XIS team created the FTOOL *xisnxbgen*, which utilizes the weighted sum of the night-time-earth observations (NTE) when the satellite points to the Earth

[2]The materials in this chapter are based on the work [83].

at night, to estimate the NXB spectra and images. In our analysis, cutoff-rigidity-weighted NXB spectra are extracted from the NTE data for each detector using the *xisnxbgen* tool. Due to the time varying nature of NXB and steady decay of ^{55}Fe source, the exposure time of NXB event files are set to cover before 150 and after 150 days from the initial exposure time. NXB event files are reprocessed following the same criteria described in Section 5.2. The same annular sections in SKYREG mode are used to produce NXB spectra in FTOOL XSELECT after the calibration sources are removed. An additional correction for the comparable fraction of flickering pixels is applied to the data which are taken after Jan 2014 [85].

6.2.2. Solar Wind Charge Exchange

Solar wind charge exchange process, hereafter SWCX, has been observed at many locations such as the solar system including magnetosheath and the corona of comets by many satellites (*ROSAT*, *XMM-Newton*, *Chandra* and *Suzaku*) [89].

The solar wind is a continuous flow of magnetized plasma of charged particles, radially outward from the Sun. This flow interacts with the neutral particles in the interstellar medium (ISM) via charge exchange process. The charge exchange process occurs when an ion interacts with a neutral particle;

$$\mathrm{A}^{q+} + \mathrm{B} = \mathrm{A}^{(q-1)^{+*}} + \mathrm{B}^{+} \tag{6.1}$$

$$\mathrm{A}^{(q-1)^{+*}} = \mathrm{A}^{(q-1)^{+}} + h\nu. \tag{6.2}$$

When heavy ions such as O^{7+} and O^{8+} encounter the neutral atoms (H or He), they transfer their charge and jump to the excited state so that eventually de-excite and emit X-ray or UV photons.

The observations revealed that SWCX spectrum is dominated by line spectrum rather than continuum. The most prominent SWCX originated lines are O VII ($\sim$

0.56 keV) and O VIII ($\sim$ 0.65 keV). In our analysis, we add two Gaussian components associated emission lines from O VII and O VIII,

$$S_{SWCX} = gaussian + gaussian \tag{6.3}$$

where the centeral line of gaussian functions are fixed at the potential line energies, 0.56 keV and 0.65 keV respectively. The widths of gaussian functions are set to 0.0 since these sources are unresolved but broadened by the instrumental response and we measure the normalizations which are left free. The fluxes of these lines could be calculated, however it requires higher spectral resolution to determine precise values.

6.2.3. Cosmic X-ray Background

The Cosmic X-ray Background, hereafter CXB, refers to the total sum of emissions from extragalactic sources -mostly Active Galactic Nuclei (AGNs)- in the energy range of 2.0-10.0 keV. These point sources are in general below our detection limit but they still have significant contribution onto the background level. The origin of this phenomenon has been discussed in many studies [90,91]. Since the hard X-ray emission from the CXB shows almost isotropic distribution over the sky, this component can be modelled. It is validated that these unresolved sources are well represented by an absorbed power law;

$$S_{CXB} = phabs * powerlaw, \tag{6.4}$$

with a photon-index of $\sim$ 1.4 [88]. In Equation 6.4, *phabs* model requires the galactic hydrogen column density (N_H) as an input, which is set to Leiden/Argentine/Bonn (LAB) value, 1.33×10^{22} cm^{-2} in our analysis [92].

6.2.4. Soft Foreground

The soft local foreground includes three components: i) local hot bubble (LHB); ii) galactic halo (GH); and iii) hot foreground (HF).

The LHB is hot low-density plasma ($kT \sim 0.1$ keV) surrounding the Sun from 50 pc to 150 pc, which is the reason of being called local. The environment of this X-ray emitting gas is called bubble since the only constituents are the plasma and a few partially ionized cloudlets. The map of the LHB is illustrated in Figure 6.1. It is apparent that the emission from hot plasma can not be absorbed by the hydrogen column density of the Galactic interstellar medium (ISM). Therefore, this background is represented by an unabsorbed thermal model,

$$S_{LHB} = apec, \tag{6.5}$$

where the temperature is fixed to 0.1 keV. Since this source of background has galactic origin, the abundance of this *apec* model is set to 1.0 Z$\odot$, whereas the redshift is fixed at 0.0.

The GH background infers the emission from the hot thermal plasma, 3×10^6 K, in the halo of the Milky Way [94]. The distance of this X-ray emitting plasma is located several hundred pc above the Galactic plane so it is away from our disk [95]. Therefore, we represent this component by an absorbed thermal model,

$$S_{GH} = phabs * apec, \tag{6.6}$$

where the the temperature is fixed to 0.25 keV. Since this source of background has galactic origin, the abundance of this *apec* model is set to 1.0 Z$\odot$, whereas the redshift is fixed at 0.0.

The HF background is an additional hot component to GH, which is thought to have main contribution from faint dM stars [96]. This additional hot thermal compo-

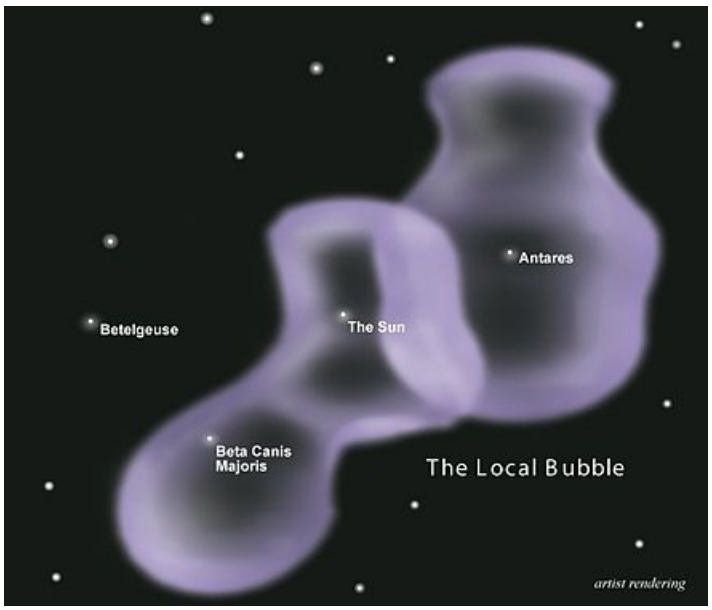

Figure 6.1. This image is illustrative map of the local hot bubble [93].

nent (0.6-0.8 keV) is also used in other studies [97] and in our analysis, it is described by an absorbed thermal model,

$$S_{HF} = phabs * apec, \tag{6.7}$$

where the temperature is fixed to 0.75 keV. This temperature is obtained from our background fits, where it is required to add an additional *apec* component to get the best-fit parameters. Since this source of background has galactic origin, the abundance of this *apec* model is set to 1.0 solar, whereas the redshift is fixed at 0.0.

6.3. Results

Understanding temporal and spatial variations in the local X-ray background is crucial in analyses of faint cluster outskirts. The variable soft X-ray background must be determined carefully before the spectral fits are performed. To determine the local background parameters to be used in the spectral analysis, we first extract a local background spectrum from the outermost region (Region 6 in Figure 6.2, $18'$ -

24′ which is beyond R_{200}) where the expected contribution from the cluster thermal emission is minimal.

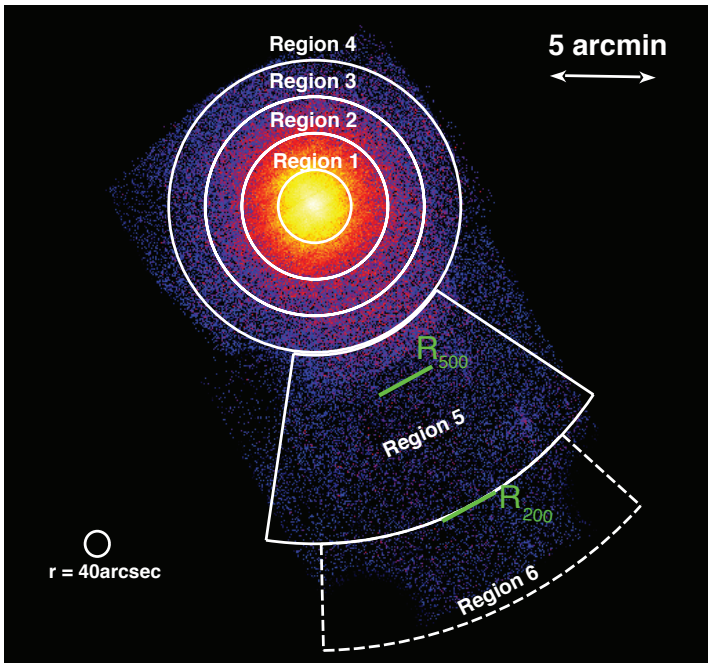

Figure 6.2. Exposure corrected, NXB background subtracted *Suzaku* XIS image of Abell 3112 (see Section 8.1). The local background is extracted from the region shown in dashed lines.

We also extract the ROSAT All Sky Survey (RASS) data from a 1 – 2 degree annulus surrounding the central sub-cluster's centroid by using the HEASARC X-ray background tool [98]. Energy range of RASS data is specified in between 0.1 – 2.0 keV.

The spectral features of local background fit is shown in Figure 6.3. As described in the previous sections, the NXB subtracted local X-ray spectrum is jointly fitted with RASS data. The rest of the X-ray background components are modelled: two Gaussian models to eliminate the O VII and O VIII lines from SWCX at 0.56 keV and 0.65 keV respectively; one power-law component for unresolved point sources (CXB); an unabsorbed thermal model for the LHB; and two absorbed thermal components (*apec*) for GH and HF. We find a good-fit with C-stat value of 507.3 for 341 degrees-of-freedom (d.o.f).

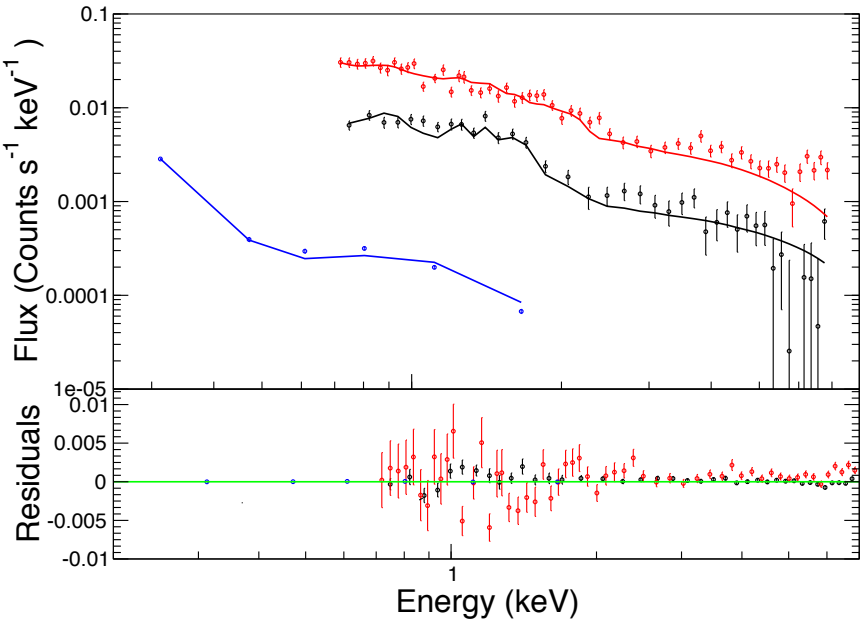

Figure 6.3. The spectral features of RASS data and combined FI & BI Suzaku XIS observation from beyond R_{200} region. The best fit model parameters are summarized in Table 6.1.

The best-fit values of the rest of soft background components are given in Table 6.1. In addition to Table 6.1, the best-fit normalization of the power-law (CXB) is $1.41^{+0.14}_{-0.14} \times 10^{-7}$ photons keV^{-1} cm^{-2} s^{-1} arcmin^{-2} at 1 keV, corresponding to a CXB flux of 4.3 +/- 0.4 $\times$ 10^{-12} ergs s^{-1} cm^{-2} deg^{-2} in the 0.5 – 2.0 keV band.

Table 6.1. Best-fit Parameters from fits to Soft X-ray Background.

Component	kT (fixed) (keV)	Normalization 10^{-8} cm^{-5}	Flux (0.5 – 2.0 keV) 10^{-16} ergs s^{-1} cm^{-2}
GH	0.25	$0.8^{+0.7}_{-0.6}$	$0.14^{+0.09}_{-0.09}$
HF	0.75	$1.2^{+0.3}_{-0.3}$	$0.34^{+0.07}_{-0.07}$
LHB	0.1	$68.4^{+6.2}_{-6.4}$	$1.29^{+0.12}_{-0.11}$

7. SYSTEMATIC UNCERTAINTIES

The analyses of low-surface brightness regions of clusters with *Suzaku* may be subject to systematic uncertainties.[3] To estimate the magnitude of these, we consider the following potential sources of uncertainties: i) systematics associated with the CXB level; ii) systematics due to variations in the soft X-ray and particle background; iii) contamination due to stray light and the large size of the PSF of *Suzaku*'s mirrors. We describe how we estimate and handle these in detail below.

7.1. The Cosmic X-ray Background

The variations in the unresolved CXB within the XIS FOV can be a source of serious systematic uncertainty. Following the same approach in [86], the detection limit in our observations is found 6.7×10^{-14} ergs cm^{-2} s^{-1} in the $2.0 - 10.0$ keV energy band. This procedure contains the extraction of the spectrum of the point sources and the background from the surrounding annulus. We then fit each point source's spectrum with,

$$S_{Flux} = phabs * powerlaw \tag{7.1}$$

where the normalization of the hydrogen column density is fixed to lab value 1.33×10^{22} cm^{-2} and the power-law photon index is freeze to 1.4. *flux* command allows us to measure the flux at given energy range. For all point sources, we compare their fluxes and determine the our *Suzaku* observations' detection limit as 6.7×10^{-14} ergs cm^{-2} s^{-1} in the $2.0 - 10.0$ keV energy band. The contribution of unresolved point sources to the total flux is calculated using the formula given in [99]:

$$F_{CXB} = (2.18 \pm 0.13) \times 10^{-11} - \int_{S_{excl}}^{S_{max}} (\frac{dN}{dS}) \times S \; dS \text{ ergs cm}^2 \text{ s}^{-1} \text{ deg}^{-2} \tag{7.2}$$

[3]The materials in this chapter are based on the work [83].

where the cumulative number of point sources per flux indicated as dN/dS is integrated over the detection limit from the lower bound $S_{excl} = 6.7 \times 10^{-14}$ ergs cm^{-2} s^{-1} to the upper bound $S_{max} = 8.0 \times 10^{-12}$ ergs cm^{-2} s^{-1} given in [99]. We use a total flux of $(2.18 \pm 0.13) \times 10^{-11}$ erg cm^{-2} s^{-1} deg^{-2} obtained from *Swift* data [100]. This flux is also consistent with the total CXB flux from *Chandra* and *XMM-Newton* observations [99, 101]. For the populations of the point sources we adopt an analytical model provided in [99]:

$$N(>S) = N_0 \Big[\frac{(2 \times 10^{-15})^{\alpha}}{S^{\alpha} + S_0^{\alpha-\beta} S^{\beta}} \Big]. \tag{7.3}$$

where the best-fit parameters are $N_0 = 5300^{+2850}_{-1400}$, $S_0 = (4.5^{+3.7}_{-1.7}) \times 10^{-15}$ ergs cm^{-2} s^{-1}, $\alpha = 1.57^{+0.10}_{-0.08}$, and $\beta = 0.44^{+0.12}_{-0.13}$. Using the best-fit parameters of hard energy band given in [99], we find that the unresolved flux contribution in the $2 - 10$ keV band to the CXB flux is $(1.38 \pm 0.62) \times 10^{-11}$ ergs cm^{-2} s^{-1} deg^{-2}.

Table 7.1. Estimated 1σ Fluctuations in the CXB level due to unresolved point sources in the *Suzaku* FOV in units of 10^{-12} ergs cm^{-2} s^{-1} deg^{-2}.

	Region 1	Region 2	Region 3	Region 4	Region 5
CXB Fluctuations	10.10	5.78	4.48	3.78	2.12

The deviations from the expected CXB level due to the unresolved point sources are,

$${\sigma_B}^2 = \frac{1}{\Omega} \int_0^{S_{excl}} (\frac{dN}{dS}) \times S^2 \, dS, \tag{7.4}$$

where Ω is the solid angle. We then calculate 1σ RMS CXB fluctuations using Equations 7.2 and 7.3 for each region. The results are shown in Table 7.1. We find that a typical 1σ uncertainty on the measured CXB level is comparable to the RMS value of CXB fluctuations. We note that this uncertainty is used in Section 7.2 to account for the CXB variations. These systematics are included in the final systematic errors on the observable quantities.

7.2. Systematics due to Variations in the Soft X-ray and Particle Background

We model the soft X-ray background by jointly fitting the ROSAT data with the local X-ray background spectra (including LHB, GH, HF), and CXB obtained from the annuli encompassing the $18'$-$24'$ region. To take into account the spatial variations which may dominate the background, we perform 1000 Markov Chain Monte Carlo (MCMC) realizations of the best-fit background model. The model parameters are allowed to vary within their 1σ uncertainty range. An uncertainty up to 3.6% on the NXB level is also taken into account in these realizations [102].

We find that the systematic variations in the soft foreground, CXB, and the particle background level has an effect of $< 1\%$ on the best-fit temperatures and normalizations of Regions 1 and 2. Variations up to 2%, 6%, and 16% are measured in Regions 3, 4, and 5. The uncertainties due to the variation in the soft X-ray background are taken into account in the total error budget calculations by adding them in quadrature.

7.3. Systematics due to Scattered light and PSF Scattering

The relatively large size of the *Suzaku* mirror PSF ($\sim 2'$) may cause photons emitted from a particular region in the sky to be detected elsewhere on the detector. We note that the size of each spectral extraction region used in this work is larger than the PSF size, minimizing the effect of PSF scattering in this analysis. To estimate the magnitude of this uncertainty, we use the ray-tracing simulator *xissim* to generate *Suzaku* event files using [103]. The *Chandra* ACIS images and the best-fit *Suzaku* spectral models are used to simulate event files of each XIS sensor with 1×10^6 photons. The image of each sector shown in Figure 6.2 (left panel) is extracted from the simulated event files.

The percentile contribution of the flux on each sector from adjacent regions are shown in Table 7.2. Columns refer to the percentage fluxes providing the flux, while the

Table 7.2. Percentage Contribution of PSF Scattering.

	Region 1	Region 2	Region 3	Region 4	Region 5
Region 1	68.5	15.6	3.47	1.33	0.33
Region 2	14.3	65.6	16.4	2.25	0.38
Region 3	0.24	17.7	64.5	13.7	0.82
Region 4	0.26	1.52	15.2	66.8	6.81
Region 5	0.09	0.27	0.79	7.06	89.2

Note: The regions in different columns represent the origins of the fluxes and the rest of the rows represent the percentage contamination from neighbouring annuli.

rows refer to the percentage fluxes receiving the flux in Table 7.2. For instance, 3.47% (first row, third column) is the fraction of photons leaked from Region 1 contaminating Region 3. As clearly seen in Table 7.2, most of the photons which originate from one particular annulus in the sky are detected in the same region on the detector, while up to 17% of the photons may be detected in surrounding annuli. However, the fraction of photons which are detected in the outermost annulus that scatter from the inner regions is negligibly small ($< 1\%$). The results are consistent with the fractions reported in [104] and [86].

To estimate the effect of the PSF scattering and the scattered light contribution to the variables, e.g. temperature and metallicity, we jointly fit the spectra of each sector with the normalizations scaled according to the reported fractions in Table 7.2. Although the uncertainty on the measured temperature is smaller than the statistical errors in each sector, we added these in quadrature to the total error budget of the thermal model variables.

8. ANALYSIS

8.1. Image Analysis

8.1.1. Suzaku Image Analysis

We combined the images from XIS0, XIS1, and XIS3 of Abell 3112 cluster in the 0.5 – 7.0 keV energy band.[4] For each observation we extract images of each XIS detector by using XSELECT and mosaic each of the five pointings in sky coordinates. The NXB images are created by using *xisnxbgen*, where the same basic cleaning criteria applied in Section 5.2 and before the exposure correction, we subtract these images from the mosaicked images.

Merging images from multiple pointings requires proper treatment of generation of exposure maps. Therefore, we follow the same procedure for the generation of exposure maps given in [86,104]. First of all, for each detector and pointing a monochromatic photon list is simulated by using XRT ray- tracing simulator *xissim* [103] as if the assumption of $20'$ uniform extended source. These vignetting corrected maps are used as the input for *xisexpmapgen* to create exposure maps. Prior to exposure correction, underexposed regions with $< 15\%$ of the maximum exposure time are removed. An exposure corrected and particle background subtracted *Suzaku* mosaic image is shown in the left panel of Figure 8.1. In this figure, the spectral extraction regions out to R_{200} are shown in white, and the region which is used to extract the local background spectrum is shown in dashed lines. The figure also shows the location of the overdensity radii R_{500} and R_{200}, which are marked with green bars in the figure. The point source exclusion radius of $40''$ is shown in the lower corner of the image.

[4]The materials in this chapter are based on the work [83].

8.1.2. Chandra Image Analysis

We extract image in the 0.5 – 7.0 keV band from two pointings. The background image is extracted from the blank-sky observations. The background subtracted and exposure corrected image is obtained by using *merge-obs* algorithm in CIAO. To account for variations in the particle background, we use count rates detected in the 9 – 12 keV band to match Abell 3112 observations as described in [87]. The CIAO's *wavdetect* tool is used to determine the locations of the point sources in the FOV. The point sources detected by *Chandra* in the *Suzaku* FOV are shown in the right panel of Figure 8.1. The figure is important that it shows the *Chandra* pointings used to detect point sources within the *Suzaku* FOV, and the brightest point source, which is used in estimating point-source exclusion extent, is shown in the green.

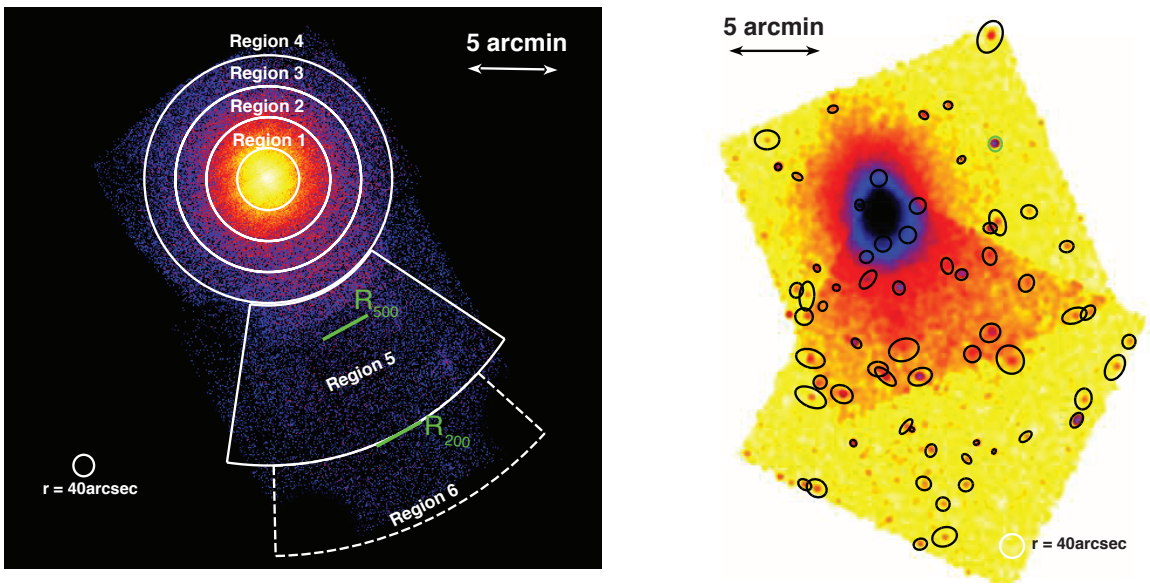

Figure 8.1. Left panel: Exposure corrected, NXB background subtracted *Suzaku* XIS image of Abell 3112. The image is extracted in the 0.5 – 7.0 keV energy range. Right panel: Background subtracted *Chandra* image of Abell 3112 is given in 0.5 – 7.0 keV energy band.

8.2. Spectral Analysis

To examine the spectral properties of Abell 3112, we extract spectra in five regions as shown in Figure 1 (Region 1, $0' - 2'$; Region 2, $2' - 4'$; Region 3, $4' - 6'$; Region 4, $6' - 8'$; and Region 5, $8' - 18'$) surrounding the cluster's centroid from the filtered event files in XSELECT for each XIS sensor (XIS0, XIS1, and XIS3). The radius of these regions are selected to be $2'$ and larger considering the large PSF size of the *Suzaku* XIS detectors (half-power diameter of $2'$). The regions are also selected based on the total source counts ($> 10^4$ counts) in each. The over density radii R_{500} and R_{200} are also marked in Figure 8.1.

The contamination due to the point sources are taken into account and we subtract all point sources resolved by *Chandra* with an exclusion radius fixed to $40''$ (see Section 5.4). Cutoff-rigidity-weighted NXB spectra are registered as background in XSPEC and extracted prior to fitting. The FTOOLS *xissimarfgen* and *xisrmfgen* are used to generate the effective area ancillary response file (ARF) and detector redistribution matrix file (RMF), respectively. For each annulus and each observation, we merge data and NXB from FI XIS0 and XIS3 detectors. The BI XIS1 data are fit simultaneously with the FI spectra. Spectral fitting is performed in the 0.7 – 7.0 keV energy band where the *Suzaku* XIS detectors are the most sensitive.

Table 8.1. The best-fit Parameters of the 1T *apec* Model.

Region	kT (keV)	Abundance ($Z_\odot$)	Normalization (10^{-6} cm^{-5})	C-stat (dof)
Region 1	4.27 ± 0.02	0.54 ± 0.01	881.0 ± 2.4	1260.9 (849)
Region 2	4.81 ± 0.04	0.36 ± 0.01	204.1 ± 2.9	1383.6 (1135)
Region 3	4.66 ± 0.05	0.26 ± 0.03	71.7 ± 0.14	997.3 (844)
Region 4	4.26 ± 0.10	0.25 ± 0.05	22.3 ± 2.3	397.9 (279)
Region 5	3.37 ± 0.77	0.22 ± 0.08	1.1 ± 0.2	264.9 (136)

8.2.1. Global Spectral Properties of Abell 3112

To examine the global temperature and abundance out to R_{200} of Abell 3112, we first fit the spectra with 1T *apec* model. The NXB background is subtracted prior to fitting, the rest of the background parameters are tied to the best fit values given in Table 6.1. The complete model can be written as;

$$\begin{aligned} S_{tot} &= constant * (gaussian + gaussian + apec \\ &+ (apec + apec + powerlaw + apec) * phabs) \end{aligned} \tag{8.1}$$

where the first six components represent the background and the last absorbed thermal model is for the cluster. The initial *constant* term is added to check the measure of the deviations, where different type CCDs have different quantum efficiencies. The model parameters between different observations are tied to each other. The best-fit projected temperature together with their 1σ statistical uncertainties are shown in Table 8.1 and the samples for the spectral features are given in the Figure 8.2, where the goodness of 1T *apec* model fits can be seen in Table 8.1.

The Figure 8.3 shows the best fit temperature and abundance radial profiles of cool-core galaxy cluster Abell 3112. In the same figure, the *Suzaku* temperature results are compared with the previous measurements from the *XMM-Newton* observations [34]. The *Suzaku* and *XMM-Newton* results are in agreement with each other at the 1σ confidence level from the cluster core out to R_{500}. While previous observations were able to measure the temperature only out to R_{500}, we are able to measure the ICM temperature to R_{200} owing to *Suzaku*'s lower particle background.

We also compare the abundance profiles obtained from *XMM-Newton* and *Suzaku* observations in Figure 8.3 . While *XMM-Newton* observations can accurately constrain the profiles in the core of the cluster out to $\sim 0.5R_{500}$, *Suzaku* observations are able to constrain abundances at radii out to R_{200}. The regions which are covered by *XMM-Newton* and *Suzaku* are in agreement with each other at the 1σ level. The abundance profile is peaked at the center, and remains fairly constant beyond $\sim 0.5R_{500}$. The

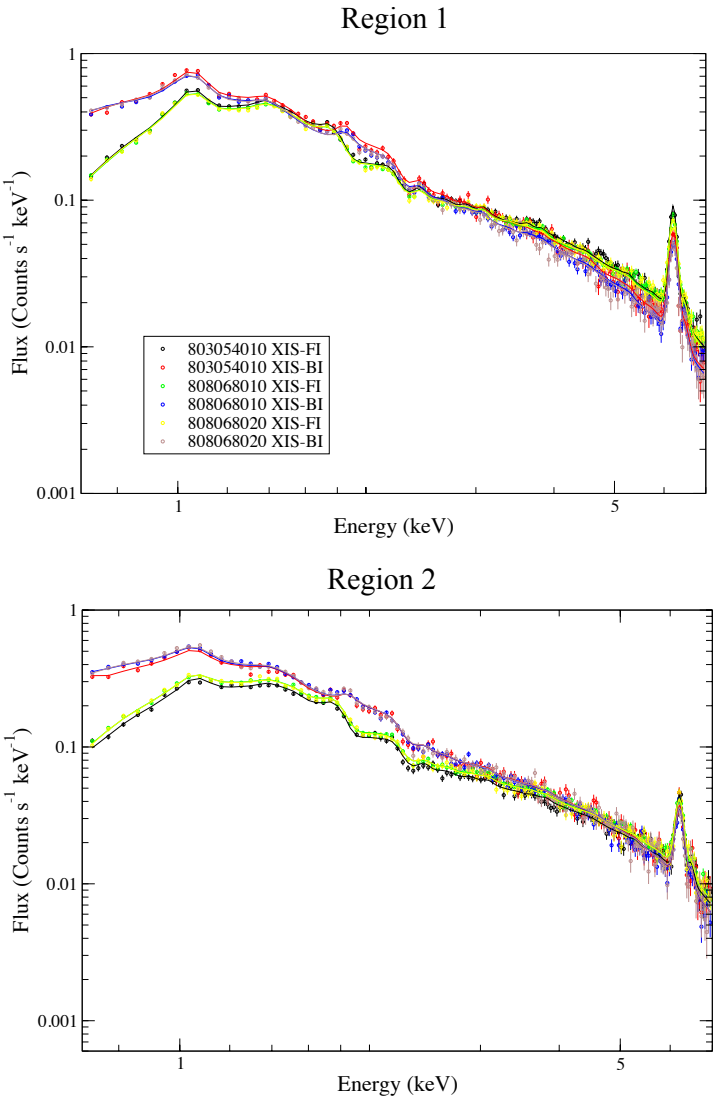

Figure 8.2. The spectral features of 1T *apec* model fits of combined FI and BI *Suzaku* XIS observations from Region 1 ($0' - 2'$, upper panel) and Region 2 ($2' - 4'$, lower panel) are shown.

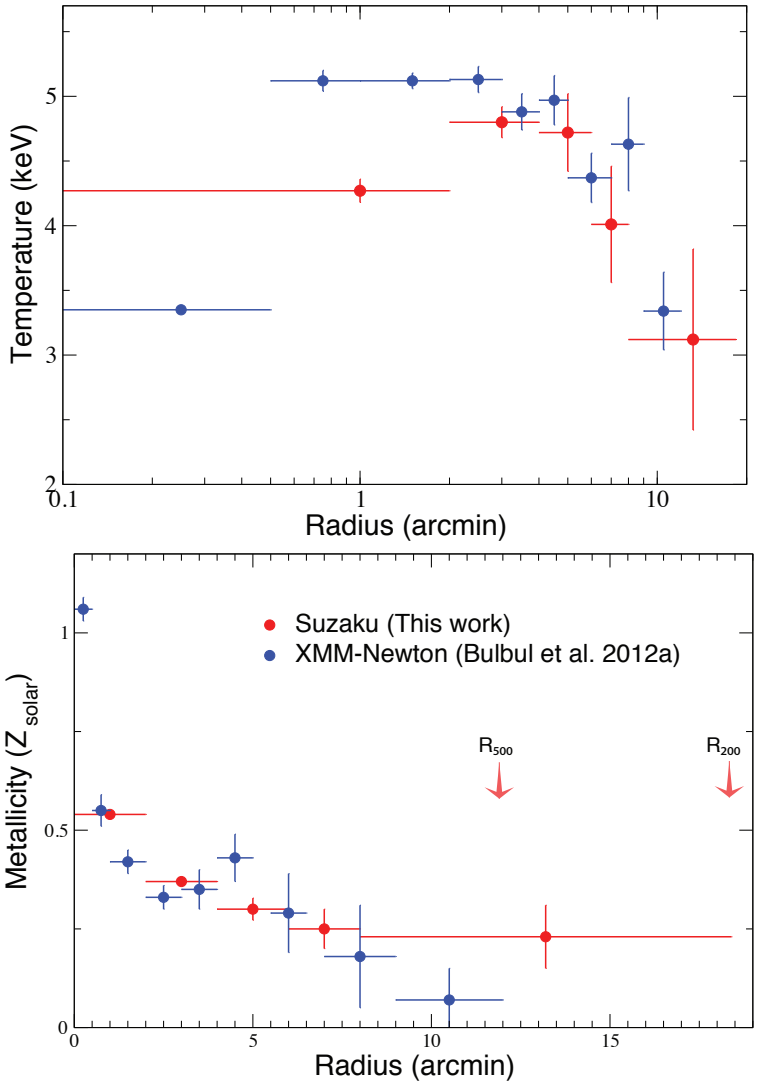

Figure 8.3. The radial profile of temperature (upper panel) and abundance (lower panel) for Abell 3112 obtained from a single temperature *apec* model. The statistical errors (68% confidence level) together with systematics on the *Suzaku* results are overplotted.

Table 8.2. The best-fit Parameters of the 2T *apec* Models.

Region	kT_1 (keV)	kT_2 (keV)	Abundance ($Z_\odot$)	Normalization1 10^{-4}cm^{-5}	Normalization2 10^{-4}cm^{-5}	C-stat (dof)
Region 1	$3.24^{+0.20}_{-0.16}$	$5.94^{+0.15}_{-0.16}$	0.55 $\pm$0.01	$4.32^{+0.90}_{-0.78}$	$4.46^{+0.78}_{-0.77}$	1135.5 (847)
Region 2	$3.41^{+0.09}_{-0.07}$	5.63 $\pm$ 0.10	0.37 $\pm$ 0.01	$0.65^{+0.08}_{-0.06}$	$1.41^{+0.15}_{-0.26}$	1366.2 (1133)

overall abundance of the ICM (mostly driven by the Fe lines) in the outskirts of the galaxy cluster is 0.25 $\pm$ 0.05 $Z_\odot$ and 0.22 $\pm$ 0.08 $Z_\odot$ in Regions 4 and 5 which cover the region between $0.5R_{500}$ and R_{200}. These measurements are consistent with the abundances found in low-mass systems [86].

In order to investigate the multi-phase gas in the ICM, we fit the spectra with a two temperature (2T) *apec* model. The best-fit temperature of the ICM in Region 1 becomes $5.94^{+0.15}_{-0.16}$ keV, with a lower kT component of $3.24^{+0.20}_{-0.16}$ keV. The temperature in Region 2 is 5.63$\pm$0.10 with a lower kT component of $3.41^{+0.09}_{-0.07}$ keV. The abundances remain unchanged in both regions with an addition of the second *apec* model. Adding the second thermal component improves the statistics of the fit to the spectra of Region 1 and Region 2 significantly (ΔC-stat=126 for 2 dof in Region 1; ΔC-stat=17 for 2 dof in Region 2), while the fits to the other regions are insensitive. C-statistics do not provide a statistical test to quantify the significance of the improvement in adding the secondary *apec* component. We therefore calculate the corresponding χ^2 values from the best-fits (which are obtained using C–statistics). The improvement in χ^2 values are 114 and 12 in Region 1 and Region 2 for two extra dof (temperature and normalization of the second *apec* model). This corresponds to F-test values of 40.8 and 4.9 with null hypothesis probabilities of 10^{-25} and 0.7% in Regions 1 and 2. The best-fit 1T and 2T *apec* model parameters are summarized in Table 8.2. The limited statistics of the spectra extracted from Regions 3, 4, and 5 do not allow to test the multi-phase nature of the plasma in these regions. We, therefore, do not provide the 2T results from those fits here.

8.2.2. Chemical Properties of Abell 3112

We further investigate the radial abundance distributions of individual α-elements, such as Si, S, Fe, and Mg out to R_{200} (see Figure 8.4). The fits are performed with a single temperature *vapec* model.

$$\begin{aligned} S_{tot} &= constant * (gaussian + gaussian + apec \\ &+ (apec + apec + powerlaw + vapec) * phabs) \end{aligned} \tag{8.2}$$

The Fe, Si, S, and Mg elemental abundances are allowed to vary independently while other elemental abundances which cannot be measured, (e.g. Ca and Ar) are fixed to the measured Fe abundance at the outskirts, $0.25Z_{\odot}$. We find that Si, S, and Fe abundances show an increasing trend towards the core of the cluster, confirming the results from *XMM-Newton* observations. We are also able to extend the detection of Si out to $\sim 0.5R_{200}$ in the *Suzaku* observations, while previous *XMM-Newton* observations report the detection of these metals only in the very central region ($< 0.06R_{200}$; see [34]).

SN Ia produce large amounts of Fe, while lighter elements, such as Mg, is produced mainly by SN cc. Measurements of the radial profile of Mg and Fe abundances within the ICM provide clues on the relative contribution of different types of SNe to the chemical enrichment. For instance, SN cc products are thought to be produced in early in the formation history of clusters at z$\sim$2 – 3 [105]. We, therefore, investigate distributions of these elements in the outskirts of Abell 3112. We perform fits to the observed Mg and Fe profiles with phenomenological models to quantify the change in their distribution with radius. In a power-law model fit to the observed Mg profile, the best-fit normalization is 0.35 ± 0.12 and index of 0.11 ± 0.15. We find a good fit with overall χ^2 of 0.62 (3 d.o.f.). Although, the power-law index in this fit indicate a slight decline with radius, it is consistent with zero. This indicates that the distribution of the Mg is consistent with a uniform profile. However, due to large uncertainties neither the uniform profile, nor the peaked profile can be excluded based on the *Suzaku* data.

We observe a steeper decline in the Fe abundance profile with a power-law index of 0.54±0.15, normalization of 0.13±0.03. The overall χ^2 is 1.37 for 3 d.o.f. The observed slope of the Fe profile is steeper compared to the Virgo cluster [105]. The Fe abundance peaks in the core of Abell 3112 (similar to those of S and Si), however it becomes uniform beyond $0.2R_{200}$ at a level of $\sim 0.22 - 0.25\ Z_{\odot}$. The uniform abundance in the outskirts of the cluster is consistent with the Fe abundance observed in the *Suzaku* observations of the nearby clusters, e.g. the Perseus cluster [106]. Additionally, the mean observed value at the outskirts of Abell 3112 is consistent with both the Perseus and Virgo clusters.

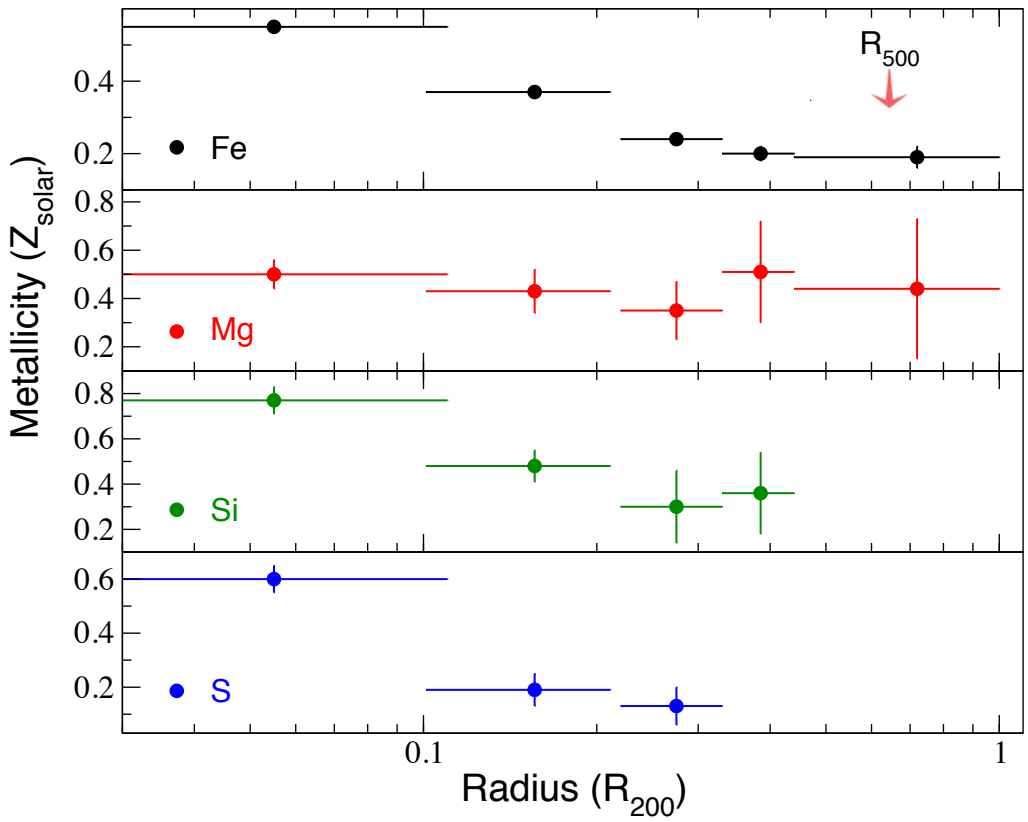

Figure 8.4. The radial distribution of elemental abundances of α-elements, Si, S, Mg, and Fe. We are able to determine Mg and Fe abundances out to R_{200}. The uncertainties are for ΔC=1.

9. CHEMICAL ENRICHMENT HISTORY OF ABELL 3112 GALAXY CLUSTER

9.1. Introduction

X-ray spectra of the ICM contain emission lines of heavy elements, which can only be produced by the late evolutionary stage of stars.[5] From the observational results, the enriched abundance in the ICM is found to be larger than the total metal abundances found in the stellar population within the cluster [22, 23]. This implies that the gas is not purely in the primordial state, but a considerable amount of it has been reprocessed within the galaxies and injected into the ICM.

ASCA observations provided the first measurements of spatial distributions of heavy element abundances, e.g., Fe and Si, in clusters of galaxies [107]. This pioneering result triggered studies for testing supernova models based on measured supernova (SN) yields. Using the limited *ASCA* measurements of abundance ratios, several studies investigated the efficiency of SN Ia and SN cc enrichment in the ICM [108–111]. These earlier studies suggest an early homogeneous enrichment by SN cc shortly after the cluster formation with its products well-mixed throughout the ICM.

The launch of satellites such as *XMM-Newton* and *Chandra*, with improved spatial and spectral resolutions, enabled more precise measurements of elemental abundances, and allowed determination of supernovae contribution to the metal enrichment in galaxy clusters' cores out to R_{500} [112–114, 116, 117].[6] The subsequently discovered centrally peaked Fe abundance at the center of cool core clusters may be explained by a more extensive period of enrichment by SN Ia explosions in the brightest cluster galaxy [118, 119]. This Fe enhancement in cluster cores is also seen in high spatial resolution observations with *XMM-Newton* [38, 120, 121].

[5] The materials in this chapter are based on the work [83].

[6] R_{500} is the radius at which the mean density of the cluster is 500 times the critical density of the Universe at the cluster's redshift.

Studies of azimuthal spatial distributions of metal abundances out to cluster outskirts have become possible with the launch of *Suzaku*. Due to its low particle background, deep observations of clusters of galaxies with *Suzaku* provide the measurements of elemental abundances and SN ratio out to R_{200} in nearby clusters ($z < 0.02$), e.g., the Perseus and Virgo clusters [105, 106]. These results suggest a uniform distribution of SN Ia and SN cc yields in the cluster outskirts, thus favoring an early enrichment by SN Ia started in the early stages of the cluster formation.

In this study, we take a further step to investigate the radial distribution of SN enrichment in Abell 3112 out to the cluster's virial radius by comparing deep *Suzaku* and *Chandra* X-ray observations with the nucleosynthesis models available in the literature.

9.2. Radial Distribution of SN Ia to SN cc Fraction

A commonly used method to constrain the distribution of SN enrichment in clusters of galaxies is to examine the relative abundances of metals which are produced by SN Ia and SN cc [114]. Detailed studies of high signal-to-noise *Suzaku* data of nearby Perseus cluster (z =0.018) and Virgo cluster (z= 0.004) have provided tight constraints on the fractional distribution of SN enrichment out to R_{200} using S, Si, and Mg abundance ratios with respect to Fe [105, 106]. However, it is challenging to perform this method for higher redshift clusters, such as Abell 3112 since the detection of abundances of key elements, e.g., Si and S, extends only out to an intermediate radius ($\sim 0.5R_{200}$). Additionally, the uncertainty of the observed Mg abundance is large in our observations. Therefore, we use an alternative approach here to measure the SN fraction out to the virial radius.

To investigate the percentage contribution of SN explosions that enrich the ICM, we fit the spectra with the *snapec* model implemented in the *XSPEC* fitting package (for details, see Section 3.6). The *snapec* model compares the SN yields available in the literature to X-ray spectra in a given energy band. After the fit is performed the goodness of the fit can be used as a test for SN yields.

The advantage of this model is that it uses all available elements to constrain the fractional contribution of SNe to chemical enrichment of the ICM as opposed to determining SN enrichment from individual elemental abundance ratios. The *snapec* model provides a self-consistent set of physical parameters, SN fraction and the total number of SNe. Therefore, statistical uncertainties on these parameters are greatly reduced because of the larger number of elemental abundance measurements used in deriving the constraints. Additionally, the method allows the user to choose between different SN enrichment models, and the goodness of the overall fit can be used to test SN enrichment models when finer resolution X-ray observations are available (see for *Hitomi* simulations [38]). This method is specifically helpful for the case here where we have low signal-to-noise data.

Table 9.1. Best-fit Parameters of *snapec* Model to the *Suzaku* Spectrum of Region 1.

SN Ia Model	N_{SNe} ($\times 10^9$)	R	C-stat (dof)
W7	3.61 ± 0.16	0.10 ± 0.01	1112.4 (840)
W70	3.59 ± 0.25	0.10 ± 0.02	1108.9 (840)
WDD1	2.79 ± 0.14	0.20 ± 0.019	1110.0 (840)
WDD	3.24 ± 0.10	0.12 ± 0.02	1108.1 (840)
WDD3	3.42 ± 0.19	0.10 ± 0.004	1110.9 (840)
CDD1	2.66 ± 0.18	0.24 ± 0.030	1111.2 (840)
CDD	3.18 ± 0.15	0.12 ± 0.01	1108.8 (840)
CDDT	3.08 ± 0.28	0.41 ± 0.09	1173.3 (840)
ODDT	3.06 ± 0.21	0.18 ± 0.03	1112.3 (840)

We use a variety of SN yields from the literature in this work (for details, see Table 3.1). Among the SN Ia yields are one dimensional spherically symmetric slow deflagration models W7 and W70; delayed detonation models referring to WDD and CDD from [68] and [115] (I99 and N06 hereafter); and two dimensional delayed detonation models including symmetric (CDDT) and asymmetric (ODDT) explosions from (hereafter M10, [69]). Meanwhile, for the SN cc yields, we use the [68] Salpeter-IMF-average yields calculated for a large range of progenitor masses (10 – 50 $M_{\odot}$) and metallicities (0 – 1 $Z_{\odot}$).

We first fit the spectrum extracted from Region 1 (0″ – 120″) using a set of yields from various SN enrichment models. The goodness of the fits of various SN Ia yields are shown in Table 9.1. We find that I99 WDD model describes the *Suzaku* data of the immediate core region the best, with C-stat of 1108.13 (840 dof), where we have the highest signal-to-noise data. The I99 W7, CDD, and WDD SN Ia models produce equally good fits to the data with ΔC-stat of 3–4 for the same number of d.o.f. Indeed, W7, WDD, and CDD models predict similar amounts of Fe and Mg. Since the most significantly detected lines in our spectra are Fe-L and Fe-K shell lines, they are likely to be responsible for the similar observed C-stat values in our fits with W7, CDD, and WDD models. Slight C-stat discrepancy between W7 and WDD (and CDD) model can be due to the under-predicted Si abundance in W7 models. However, due to the saddle difference in abundance yields of elements which are available to us in CCD resolution observations, we cannot distinguish between W7, W70, CDD, and WDD models in this work.

Additionally, we find that M10 CDDT model produces a significantly worse fit to the data (ΔC-stat=65 for 840 dof) compared to the 1D deflagration and detonation SN Ia models. The current *Suzaku* CCD observations can already confirm that there is a disagreement between the *Suzaku* observations core region of Abell 3112 and the M10 CDDT model. The underlying reason is the over-predicted Si abundance and under-predicted Mg abundance in the M10 CDDT model compared to observations in the core region (Region 1). A similar tension in *XMM-Newton* observations of a large sample of clusters is reported by [122]. The authors suggest that the observed

discrepancy is due to high Si/Fe ratio requested by the CDDT model similarly to our conclusion. Lastly, we find a better agreement with the ODDT model and the *Suzaku* data as compared to the M10 CCDT model. This agreement is also noted in [122].

Table 9.2. Best-fit Parameters of the *snapec* Model Obtained Using I99 WDD SN Ia and I99 SN cc yields.

Region	N_{SNe} ($\times 10^9$)	R	C-stat (dof)
Region 1	3.24 ± 0.10	0.12 ± 0.02	1108.1 (840)
Region 2	1.96 ± 0.36	0.16 ± 0.02	1079.9 (842)
Region 3	1.48 ± 0.13	0.12 ± 0.04	1008.9 (850)
Region 4	1.22 ± 0.12	0.13 ± 0.05	337.3 (259)
Region 5	0.87 ± 0.17	0.11 ± 0.06	244.2 (151)

To determine the distribution of SN fraction out to R_{200} rather than individual testing the SN Ia models, we use the I99 WDD SN Ia and I99 SN cc yields providing the best-fit to the highest signal-to-noise data we have here in determining SN fractions. In the *snapec* model fits of Region 1 the model parameters N_{SNe}, R, kT, redshift, and normalization are left free. The best-fit parameters of the *snapec* models are given in Table 9.2. The temperature measurements between 2T *snapec* (5.29 ± 0.2 keV, 3.24 ± 0.12 keV) and 2T *apec* fits are consistent with each other within the 1σ confidence level. The best-fit N_{SNe} and R are respectively (3.24 ± 0.10) $\times 10^9$ and 0.12 ± 0.02. To calculate the total number of SN explosions that enrich the ICM, the parameter N_{SNe} should be rescaled with the projected gas mass within the spectral extraction region (see for details [38]). The gas mass within 0 – 2′ is 3.3 $\times 10^{12} M_{\odot}$ (see for mass profiles [34]). Applying a conversion factor of 3.3 (in the units of 10^{12} $M_{\odot}$), we find that the ICM of the core of Abell 3112 has been enriched by a total of 1.00 ± 0.03 $\times 10^9$ SN

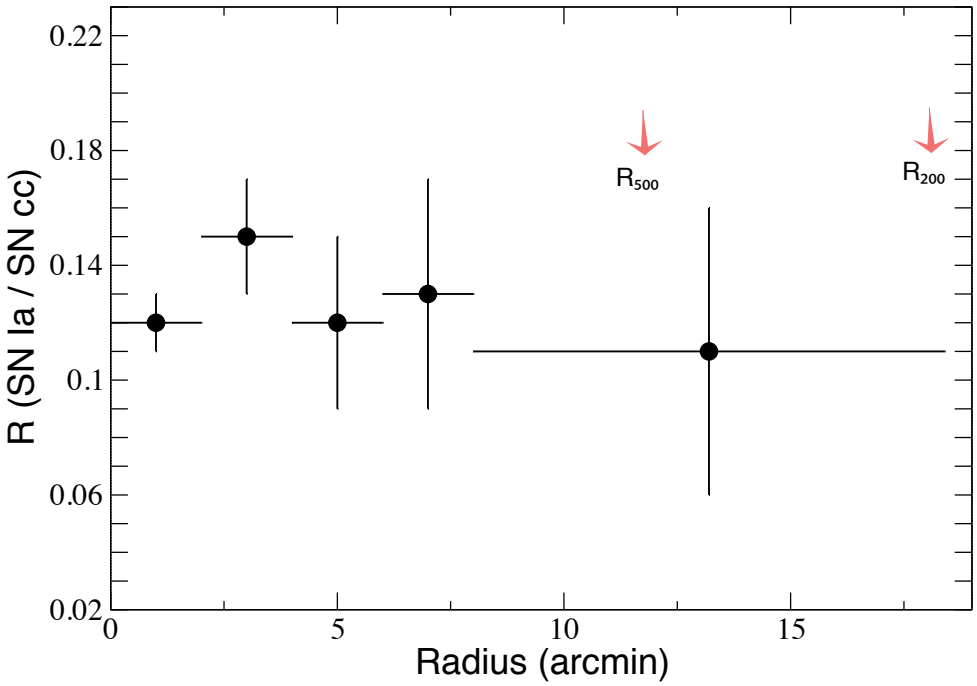

Figure 9.1. The radial distribution of the SN Ia to SN cc ratio in Abell 3112 out to R_{200} obtained from the fits of X-ray spectra with I99 WDD SN yields. The statistical errors corresponding to $\Delta C = 1$ with the systematic uncertainties are added to the total error budget.

explosions within a 12.5 billion year period. This result is consistent with the reported total number of SN explosions ($1.06 \pm 0.34 \times 10^9$) from *XMM-Newton* observations [38].

The observed fraction R in the *Suzaku* observations corresponds to a SN Ia fraction of 11% in the 0 – 2′ region of the cluster. We note that in their results [38] report a SN Ia fraction of $\sim$ 30% in the inner 52 kpc (0.6′) core region of the cluster. The discrepancy in the SN Ia fraction indicate that SN fraction is diluted by the large PSF size of the *Suzaku* mirrors. The observed difference of the radial profiles of SN Ia products, e.g., S and Si between the *XMM-Newton* and *Suzaku* observations, indeed, indicates a similar offset.

Using the I99 WDD models in the *snapec* fits of Region 2, we find that N_{SNe} is 1.96 $\pm$ 0.36 $\times$ 10^9, while R is 0.16 $\pm$ 0.02 with C-stat=1079.9 (for 842 dof). The reported enclosed gas mass is 7×10^{12} $M_\odot$ in Region 2 based on the [132] models (see [38]). Normalizing the N_{SNe} with a factor of 7, we find that the total number of SN explosions enriching the ICM in Region 2 is $(2.8 \pm 0.5) \times 10^8$ within 12.5 billion years.

The low signal-to-noise data in the spectra of Regions 3, 4, and 5 do not allow us to determine of both N_{SNe} and normalization of the *snapec* model simultaneously due to the degeneracy between these variables. The normalization of the *snapec* model is essentially determined from the continuum level, and it should be consistent with the normalization parameter of the *apec* model. We therefore use the normalization constrained from the *apec* model fits for the spectra of Regions 3, 4, and 5 and allow them to vary within their 1σ ranges. The best-fit parameters of the *snapec* model obtained with this method are shown in Table 9.2. For all the spectra we find acceptable fits to the *snapec* model.

The distribution of R (=SN Ia/SN cc) is shown in Figure 9.1 from the cluster core out to R_{200}. We note that the systematic uncertainties are included in the error bars shown in the figure. We find that the SN Ia and SN cc ratio, R, is consistent with a uniform SN Ia contribution to the enrichment, with $R \sim 0.13$. The SN Ia fraction of 11 – 14% (of the total SN explosions) are consistent with the enrichment

of the solar neighborhood [123]. This uniformity suggests that both SN Ia and SN cc enrichment of the ICM outside of the core occurred at an early epoch. Since star formation in galaxy clusters occurs at $z > 2$ [124], this implies that the SN Ia that enrich the ICM are of the prompt variety, exploding with short delay following this early epoch of star formation. A similar conclusion is inferred from measurements in the low redshift Perseus and Virgo clusters [105, 106], and the early enrichment timescale is consistent with studies of mass-selected samples of galaxy clusters with redshift $0 < z < 1.5$ [125, 126].

10. DEPROJECTED PROFILES

The clusters of galaxies are three dimensional objects on the sky, however our observations of optically thin ICM can only cover two dimensional images of them. To recover three dimensional information, one has to assume a certain shape for the gas distribution such as spherical symmetry. In this chapter, we will analyze and discuss the deprojected temperatures and densities of our cluster, and we will later use our deprojected results to calculate gas mass fraction of Abell 3112 galaxy cluster.

10.1. DSDEPROJ: The method for Deprojection

For deprojection analysis, we adopt the method "Direct Spectral Deprojection (DSDEPROJ)" [127]. This code is based on a model-invariant algorithm and hence uses spherical symmetry and purely geometric procedure to calculate deprojected spectrum [128, 129].

This python based code requires spectra and background for each shell with embedded header keywords (e.g. outer radius, initial and final angles, which are necessary to calculate the volume and area elements). In our analysis, we used BACKFILE keyword and prefer background subtracted spectrum to be used. As illustrated in Figure 10.1, this code starts from the outermost annulus and assumes the emission comes from a spherical shell. The volume normalized spectrum of the outermost region is then scaled by the volume projected onto the next neighbouring inner spherical shell and subtracted from the spectrum of that annulus, hence for this neighbouring region a new spectrum is created. This procedure continues by subtraction of outer projected emissions from inner regions with successive iterations and generate a new set of deprojected spectra.

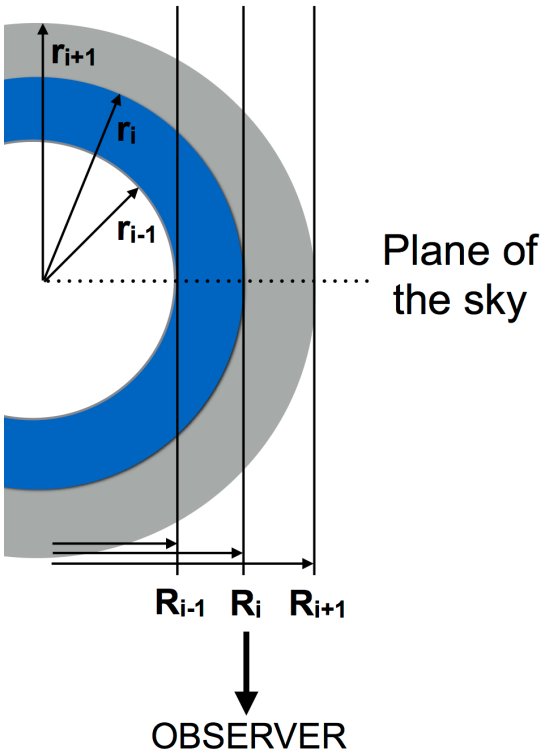

Figure 10.1. Illustration of the contamination of the extracted spectrum [130].

10.2. The Application to Abell 3112 Galaxy cluster

The source and background are extracted following the same procedure as explained in Section 5.2 and Chapter 6 respectively. Dsdeproj code requires some external parameters and these parameters are added manually by using *ftool fparkey*. The outer boundary (in arcmin), the starting angle (in degrees), and the stopping angle (in degrees) of each annular region are specified by the three additional keywords respectively, where XFLT0001, XFLT0004, and XFLT0005, are added to both the spectrum and background files. Adding the BACKFILE to each spectrum is also done manually by using *fparkey*.

The observed deprojected spectra are then fitted by using a single-temperature *apec* model. The resulted spectrum of $0 - 2'$ and $2' - 4'$ regions are given in the Figure 10.2 to demonstrate the spectral features. For both figures; the solid lines represent

the best fit line of the single temperature *apec* model (for details, see Equation 8.1) and data points are denoted by circles. The goodness of the fits can be checked by the lower panels showing the residuals. To calculate the baryonic mass fraction, we need to determine the deprojected temperature and density. The best fit parameters by using deprojected spectra give us deprojected temperature and the emission measure. To obtain the electron density, we use the best-fit normalization *Norm* (or emission measure) given in Equation 2.8 of the *apec* model. The resulting deprojected electron density and temperature are summarized in Table 10.1.

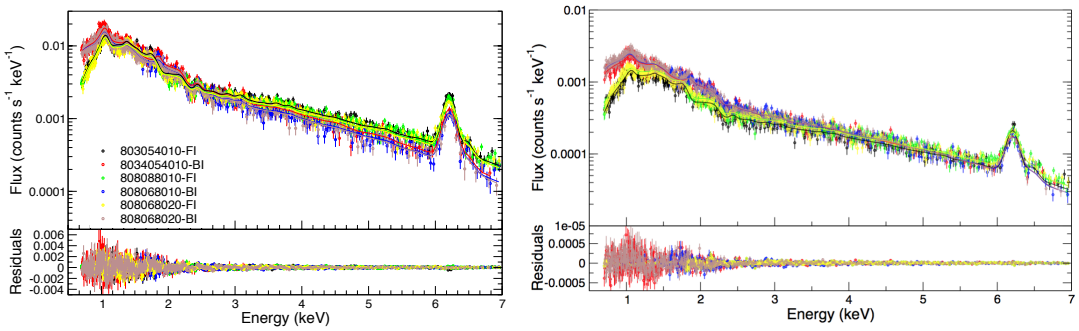

Figure 10.2. The deprojected spectra are shown to demonstrate the spectral features of single temperature model from Region 1 (0 – 2′, upper panel) and Region 2 (2′ – 4′, lower panel).

Table 10.1. 1T Apec Model with 1σ statistical errors.

Region	1T Apec		
	kT (keV)	Electron Density ($10^{-3}\times$ cm^{-3})	χ^2/d.o.f
0′ – 2′	4.16 ± 0.03	38 ± 3.2	2681.20/2426
2′ – 4′	4.76 ± 0.05	8.1 ± 0.81	2519.85/2427
4′ – 6′	4.56 ± 0.1	2.8 ± 0.38	2506.66/2427
6′ – 8′	3.89 ± 0.07	0.80 ± 0.10	2428.32/2427
8′ – 13.3′	3.16 ± 0.50	0.55 ± 0.17	737.26/617
13.3′ – 18.3′	2.82 ± 0.20	0.37 ± 0.092	1000.18/617

The radial profiles of deprojected temperature and electron density are given in the Figure 10.3. We are able to obtain temperature and density profile out to R_{200} ($\sim$ 1470 kpc). This central drop of the temperature provides the first clue that Abell 3112 is a cool core cluster.

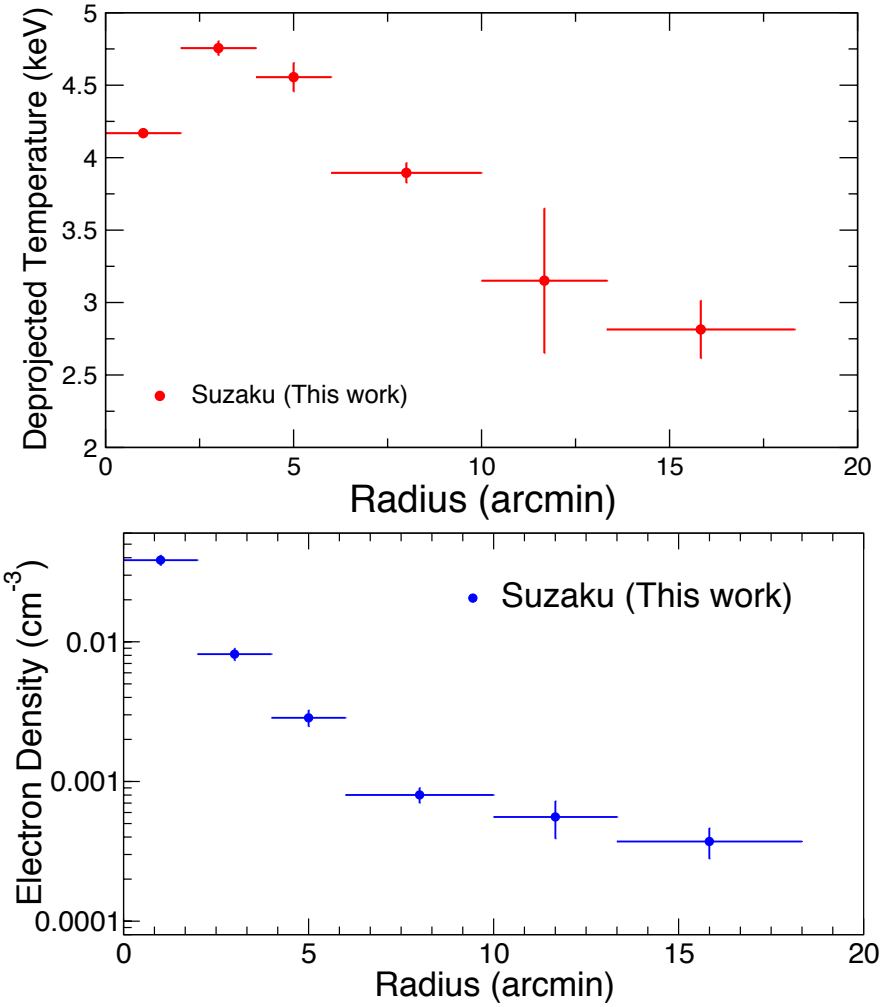

Figure 10.3. Upper Panel: Deprojected radial temperature profile is obtained from single temperature *apec* model in 0.7 – 7.0 keV energy range. Lower Panel: The deprojected radial density profile from the single temperature *apec* model in the 0.7 – 7.0 keV range. Both figures contain the statistical errors at 68% confidence level.

11. GAS MASS FRACTION IN GALAXY CLUSTERS

Galaxy clusters as being a fair volume representative of the Universe are the most important objects to constraint cosmological models and thus they are effective probes in cosmology. In particular, galaxies and intracluster gas are trapped in the gravitational potential well of the dark matter, which is also called "dark matter halo". The relation between the total mass of the cluster and the mass of the gas are highly nontrivial. In this chapter, we will use results of Section 10.2.

11.1. The Model for Gas Mass Fraction

There are various methods (such as β and double β models [131]) to discriminate the contribution of the baryonic mass to the total mass of the cluster. In this work, we adopt Bulbul et al. Model given in [132], and the detailed discussion of the adopted model is briefly explained.

Hot gas in the ICM can be observed through the direct measurement of the X-ray emission [41], or through its effects on the Cosmic Microwave Background (CMB), which is so-called Sunyaev-Zeldovich Effect [133]. The S-Z effect is effectively used for observing clusters at high redshifts since it is independent from the distance.

It is known that the pressure gradient in the ICM drifts the gas particles outward from the center, whereas the gravitational force pulls them towards the center. Hydrostatic equilibrium states the balance of theses forces, pressure differences and the gravity.

The generalized 3-dimensional mass density equation obtained from Navarro-Frenk-White model (NFW model, [134]) is given by

$$\rho_{tot}(r) = \frac{\rho_i}{(r/r_s)(1 + r/r_s)^{\beta}} \tag{11.1}$$

where ρ_i is the normalization constant and r_s is the scale radius which refers the size of the dark matter halo. The spherically symmetric distribution leads the total mass of the cluster within radius r,

$$M(r) = 4\pi\rho_i r_s \int_0^r \frac{r'}{(1 + r'/r_s)^\beta} dr' \tag{11.2}$$

With the result of the integral, total mass of the cluster is obtained as,

$$M(r) = \frac{4\pi\rho_i r_s^3}{(\beta - 2)} \Big(\frac{1/(1-\beta) - r/r_s}{(1 + r/r_s)^{\beta-1}} + \frac{1}{\beta - 1} \Big) \tag{11.3}$$

The gravitational potential at a point r is defined as,

$$\phi(r) = \int_\infty^r \frac{GM(r)}{r^2} dr \tag{11.4}$$

When we insert $M(r)$ into the Equation 11.4, the gravitational potential takes the form as,

$$\phi(r) = \phi_0 \Big[\frac{(1 + r/r_s)^{\beta-2} - 1}{(\beta - 2) r/r_s (1 + r/r_s)^{\beta-2}} \Big] \tag{11.5}$$

where ϕ_0 is the central potential with,

$$\phi_0 = (-4\pi G \rho_i r_s^2)/(\beta - 1) \tag{11.6}$$

Under the assumption of hydrostatic equilibrium,

$$\frac{dP_e(r)}{dr} = -\rho(r) \frac{d\phi(r)}{dr} \tag{11.7}$$

where $P_e(r)$ is the electron pressure and $\rho(r)$ can be expressed in terms of $\rho(r) = \mu m_p n_e(r)$ of which μ is the mean molecular weight, m_p is the mass of a proton and n_e is the number of electron density. If the ideal gas law where $P_e(r) = n_e(r) k_B T(r)$ is

used, the Equation 11.7 becomes,

$$\frac{k}{\mu m_p}\Big(T(r)\frac{dn_e(r)}{dr} + n_e(r)\frac{dT(r)}{dr}\Big) = -n_e(r)\frac{d\phi(r)}{dr} \tag{11.8}$$

For our analysis, we will use polytropic equation which states that:

$$n_{e,poly}(r) = \frac{n_{e0}}{T_0^n} T_{poly}(r)^n \tag{11.9}$$

and leads to radial temperature distribution as:

$$\frac{dT(r)}{dr} = -\frac{\mu m_p}{k(n+1)}\frac{d\phi(r)}{dr} \tag{11.10}$$

and using gravitational potential given in Equation 11.5 yields:

$$T_{poly}(r) = T_0\Big[\frac{(1+r/r_s)^{\beta-2}-1}{(\beta-2)r/r_s(1+r/r_s)^{\beta-2}}\Big] \tag{11.11}$$

where $T_0 = \frac{4\pi G\mu m_p \rho_i r_s^2}{k(n+1)(\beta-1)}$ and if we insert this quantity into the polytropic equation, we will obtain the value of electron number density,

$$n_{e,poly}(r) = n_{e0}\Big[\frac{(1+r/r_s)^{\beta-2}-1}{(\beta-2)r/r_s(1+r/r_s)^{\beta-2}}\Big]^n \tag{11.12}$$

Now the crucial part for the cool core cluster is to introduce cooling temperature for the central region. This requires a small modification in the measured temperature,

$$T(r) = T_{poly}(r)\tau_{cool}(r) \tag{11.13}$$

where $\tau_{cool}(r)$ described by,

$$\tau_{cool}(r) = \frac{\alpha + (r/r_{cool})^\gamma}{1 + (r/r_{cool})^\gamma} \tag{11.14}$$

r_{cool} is the cooling radius and α is the measure of central cooling constraint to $0< \alpha <1$. Hence, the explicit temperature for the cool core clusters is derived as:

$$T(r) = T_0\Big[\frac{(1+r/r_s)^{\beta-2}-1}{(\beta-2)r/r_s(1+r/r_s)^{\beta-2}}\Big]\frac{\alpha+(r/r_{cool})^{\gamma}}{1+(r/r_{cool})^{\gamma}} \tag{11.15}$$

Right now, we can derive the electron gas pressure from the ideal gas law:

$$P_e(r) = P_{e0}\Big[\frac{(1+r/r_s)^{\beta-2}-1}{(\beta-2)r/r_s(1+r/r_s)^{\beta-2}}\Big]^{(n+1)} \tag{11.16}$$

where $P_{e0} = kn_{e0}T_0$ and this left the electron gas pressure equation with four free parameters. When we adopt the polytropic pressure distribution, the gas density is driven as follows.

$$\begin{aligned} n_e(r) &= \frac{P_e(r)}{kT(r)} \\ &= n_{e0}\Big[\frac{(1+r/r_s)^{\beta-2}-1}{(\beta-2)r/r_s(1+r/r_s)^{\beta-2}}\Big]^{n}\tau_{cool}^{-1} \end{aligned} \tag{11.17}$$

Therefore, the modified mass distribution for cool core clusters is given:

$$M(r) = \frac{4\pi\rho_i r_s^3}{(\beta-2)}\Big(\frac{1/(1-\beta)-r/r_s}{(1+r/r_s)^{\beta-1}}+\frac{1}{\beta-1}\Big)\tau_{cool}(r) \tag{11.18}$$

where the additional $\tau_{cool}(r)$ term is considerable effect for small radii, however at large radii the term becomes insignificant and the state approaches to polytropic equation of state. The gas mass within the cluster's volume is equal to:

$$M_{gas} = \int \rho_{gas}dV = 4\pi\mu_e m_p \int n_e(r)r^2dr \tag{11.19}$$

The gas mass fraction is defined as the ratio of the gas mass to the total mass within a fixed radius and given by the expression:

$$f_{gas} = \frac{M_{gas}}{M_{tot}} \tag{11.20}$$

Since the stars together with the gas are the only interacting constituents via the Standard Model and stars have very small fraction compared to the gas, the gas mass fraction can be considered as baryonic mass ratio of the cluster. Therefore, by considering the clusters as a fair representative of the Universe, we may roughly rewrite the Equation 11.20,

$$f_{gas} = \frac{M_{gas}}{M_{tot}} \simeq \frac{\Omega_B}{\Omega_M} \tag{11.21}$$

where Ω_M is the matter density, Ω_B is the baryon density and $\frac{\Omega_B}{\Omega_M}$ term is the baryon fraction of the Universe.

11.2. The Application to Abell 3112 Galaxy Cluster

We present the gas mass fraction of the Abell 3112 galaxy cluster, as being one of the relaxed cool core described in Section 1.3. For this cluster, we use obtained profiles and fit them with modified temperature and gas density distributions derived in the previous section to calculate modified mass distribution for our Abell 3112 cool core galaxy cluster.

We use the deprojected temperature values and gas densities found in Section 10.2. Since these two sets have common parameters, it requires to perform simultaneous fit to obtain the best fit values. Markov Chain Monte Carlo Metropolis Hastings (hereafter MCMC M-H) code is used to perform the fit, because this algorithm allows the simultaneous estimation of the parameters for complex models with multi parameter space. The model in total has five set of free parameters of which are common for both temperature and density profiles (β, r_s, γ, α, r_{cool}) and three separate parameters (T_0, n_{e0}, n).

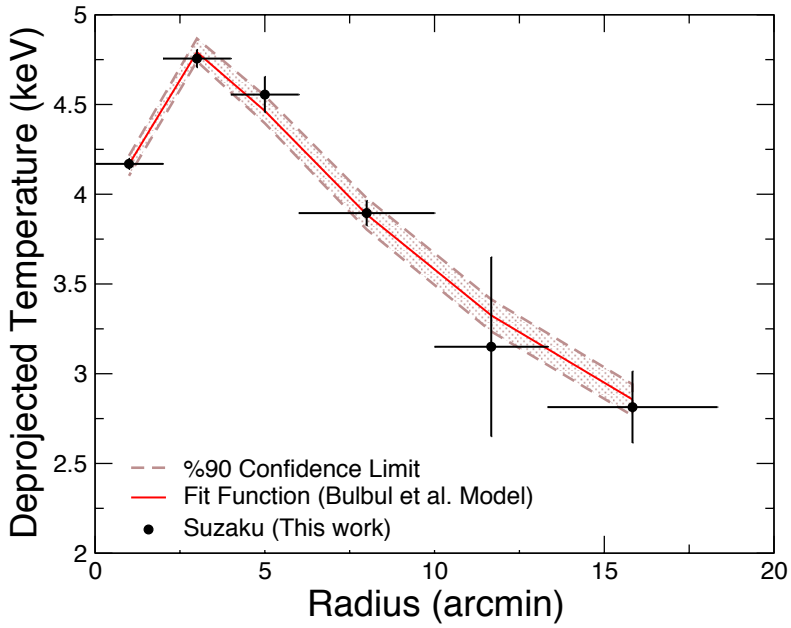

Figure 11.1. The radial deprojected temperature profile of *Suzaku* observations of Abell 3112 galaxy cluster with the best fit to Bulbul et al. Model [132] and 90 % confidence limit.

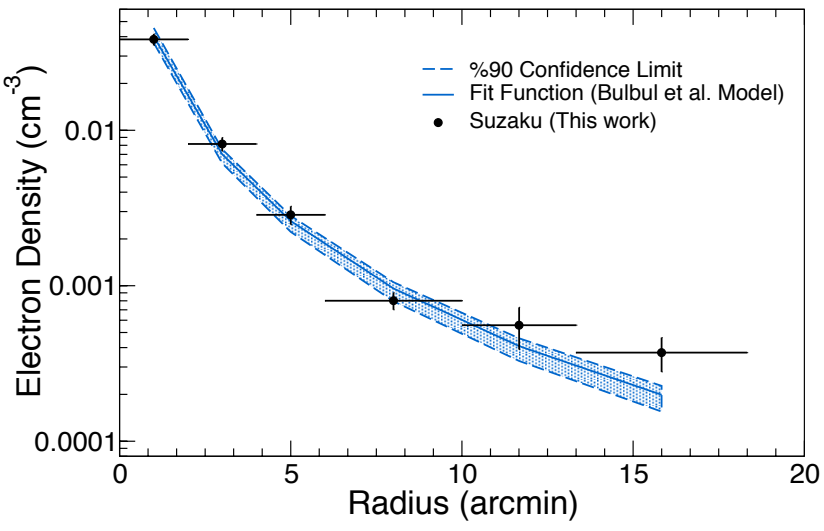

Figure 11.2. The radial deprojected gas density profile of *Suzaku* observations of Abell 3112 galaxy cluster with the best fit to Bulbul et al. Model [132] and 90 % confidence limit.

The resulting deprojected temperature measurements of *Suzaku* observations and applied model to fit the radial profile are given in the Figure 11.1. Furthermore, the measured deprojected normalizations are used to calculate electron density and the results of deprojected density measurements of *Suzaku* observations with applied model to fit the radial profile of gas density are given in the Figure 11.2.

Table 11.1. The best fit parameters of Bulbul et al. Model [132], with all errors at the 90% confidence level.

n_{e0} ($\times 10^{-2}$ cm^{-3})	β	n	r_s (arcsec)	r_{cool} (arcsec)	α	γ	T_0 (keV)	χ^2/dof
$3.50^{+0.80}_{-0.35}$	$2.11^{+0.01}_{-0.04}$	$3.30^{+0.15}_{-0.12}$	$87.0\ ^{+11.0}_{-15.0}$	$161.8^{+17.0}_{-13.0}$	0.03	$0.85^{+0.05}_{-0.01}$	$17.5^{+1.50}_{-0.50}$	11 / 5

By using the best fit parameters given in Table 11.1, the total mass and gas mass within a specific volume are calculated by using Equations 11.18 and 11.19. The derived gas mass, total mass and gas mass fraction of the cool core Abell 3112 galaxy cluster are utilized in Table 11.2.

Table 11.2. The derived gas mass, total mass and gas mass fraction of *Suzaku* measurements of Abell 3112 galaxy cluster at R_{2500} and R_{500} with errors at 90% confidence levels.

Δ	r_Δ (arcsec)	r_Δ (kpc)	M_{gas} 10^{13} M$_\odot$	M_{tot} 10^{14} M$_\odot$	f_{gas}
2500*	$331.0^{+16.1}_{-14.2}$	$452.5^{+26.4}_{-49.9}$	$3.05^{+1.90}_{-1.36}$	$1.69^{+0.39}_{-0.28}$	$0.18^{+0.12}_{-0.08}$
500 *	$708.8^{+43.7}_{-36.5}$	$968.9^{+59.7}_{-68.2}$	$7.05^{+5.08}_{-3.59}$	$3.31^{+0.77}_{-0.63}$	$0.21^{+0.16}_{-0.11}$

Note: * indicates the parameters adopted from [34].

We can compare our foundings with the results from 9-year Wilkinson Microwave Anisotropy Probe (hereafter WMAP). By using the results from [135] as $\Omega_B h^2 = 0.02264 \pm 0.00050$ and $\Omega_c h^2 = 0.1138 \pm 0.0045$, we can derive the baryon fraction of

the Universe;

$$f_B = \frac{\Omega_B h^2}{\Omega_B h^2 + \Omega_C h^2} = 0.166 \pm 0.0065 \tag{11.22}$$

The derived gas mass fraction at R_{500} is found to be $f_{gas} = 0.21^{+0.16}_{-0.11}$, which overestimates the WMAP 9-year result. To ensure reasonable results, we require to have more proper observations (more data points) for a detailed analysis.

12. CONCLUSIONS

This work presents an analysis of deep *Suzaku* (1.2 Ms of total XIS exposure) and *Chandra* (72ks) observations of Abell 3112, to constrain the distribution of SN enrichment of the ICM from the cluster core out to the cluster's virial radius using various published SN yields [68, 69, 115]. To constrain the SN fraction we use an *XSPEC* model, which is capable of fitting X-ray spectra with pre-defined SN yields from the literature.

Deep *Suzaku* observations of this relaxed archetypal cluster allow us to measure the plasma temperature and metal abundance out to cluster's virial radius. We find that temperature constraints from *Suzaku* observations are in agreement with previous *XMM-Newton* observations within R_{500}. The temperature profile peaks around ~ 4.8 keV and declines to 3.37 ± 0.77 around the virial radius of the cluster.

We are also able to extend the measurements of metal abundances out to the cluster's virial radius. We find that the metallicity of the ICM is $0.22 \pm 0.08\ Z_{\odot}$ in the outskirts of the cluster near the virial radius and is consistent with the reported metallicities in nearby clusters [86,105,106]. The observed decline in the Fe abundance is steeper compared to the Mg profile, however, the Fe profile becomes uniform beyond the overdensity radius of $0.2R_{200}$.

We find that the W7, CDD, and WDD SN Ia models produce similar goodness-of-fit to the *Suzaku* data. The best-fit SN fraction and the total number of SN parameters obtained from these models are consistent with each other. However, a 2D delayed detonation SN Ia model M10 CDDT produces significantly worse fits to the X-ray spectrum of the central region of the cluster. This suggests that the CDDT models are insufficient to reproduce observed metal abundances (e.g. Si and Mg) in the cores of cluster of galaxies. Nonetheless, accurate testing of SN Ia models using galaxy cluster spectroscopy requires higher spectral resolution. Unfortunately, it will have to wait for the launch of the next calorimeter mission (see [38, 136]).

The distribution of the SN Ia fraction to the total number of SN explosions changes between 11 – 14% based on the I99 WDD delayed detonation models, which produce the best-fit to the X-ray spectra. This fraction is consistent with the observed fraction in our Galaxy and proto-solar abundances (13 – 20%) [123]. We find that the distribution of the SN Ia fraction is fairly uniform out to the cluster's virial radius. The homogenous SN fraction points to an early (z$\sim$2–3) metal enrichment and mixing originating from an intense period of star formation activity in the cluster outskirts, and it also suggests that the metals are well-mixed into the ICM. Furthermore, our results are in agreement with the early enrichment timescale inferred from nearby Perseus and Virgo clusters [105, 106] and a mass-selected sample of galaxy clusters reported by [126].

Furthermore, we also investigate the gas mass fraction of this cool core Abell 3112 cluster by using our observational results. The deprojected temperatures and densities of the *Suzaku* XIS spectra are fitted with [132] model which considers modification on temperature profile for cool core clusters. We calculate the total mass of the cluster at R_{500} as $3.31^{+0.77}_{-0.63} \times 10^{14} M_{\odot}$ and our results are consistent with [34]. Additionally, we derive the gas mass fraction at R_{500} as $f_{gas} = 0.21^{+0.16}_{-0.11}$, which is comparable with the 9-year WMAP result for the baryon fraction of the Universe.

REFERENCES

1. Borgani, S., M. Plionis, O. Lopez-Cruz and D. Hughes, "A Pan-Chromatic View of Clusters of Galaxies and the Large-Scale Structure", *Lecture Notes Phys., 740, 287*, 2008th Edition, Springer, United States, 2008.

2. Voit, G. M., "Tracing cosmic evolution with clusters of galaxies", *Reviews of Modern Physics*, Vol. 77, p. 207, 2005.

3. Peterson, J. R. and A. C. Fabian, "X-ray Spectroscopy of Cooling Clusters", *Physics Reports*, Vol. 427, No. 1, pp. 1–39, 2006.

4. Biviano, A., "Constructing the Universe with Clusters of Galaxies", F. Durret and D. Gerbal (editors), p. 25, 2000.

5. Hubble, E., "A Relation Between Distance And Radial Velocity Among Extragalactic Nebulae", *Proceedings of the National Academy of Sciences*, Vol. 15, No. 3, pp. 168–173, 1929.

6. Zwicky, F., "On the Masses of Nebulae and of Clusters of Nebulae", *The Astrophysical Journal*, Vol. 86, p. 217, 1937.

7. Abell, G. O., "The Distribution of Rich Clusters of Galaxies", *The Astrophysical Journal Supplement*, Vol. 3, p. 211, 1958.

8. Owen, F. N., "The 1400-MHz luminosity function for Abell clusters of galaxies", *The Astrophysical Journal*, Vol. 195, pp. 593–603, 1975.

9. Jaffe, W. J. and G. Perola, "A Westerbork survey of clusters of galaxies. I - 21 CM observations of A1656, A2147, A2151, A2197 and A2199 - Radio data and identifications ", *Astronomy and Astrophysics Supplement Series*, Vol. 21, pp. 137–169, 1975.

10. Owen, F. N., R. A. White, K. C. Hilldrup and R. J. Hanisch, "A 1400-MHz survey of 1478 Abell clusters of galaxies", *Astronomical Journal*, Vol. 87, pp. 1083–1087, 1982.

11. Fomalont, E. B. and D. H. Rogstad, "Radio Emission from Clusters of Galaxies", *The Astrophysical Journal*, Vol. 146, p. 528, 1966.

12. Slingo, A., "Observations of ten extragalactic radio sources with very steep spectra", *Monthly Notices of the Royal Astronomical Society*, Vol. 166, pp. 101–111, 1974a.

13. Slingo, A., "The structure of origin of radio sources with very steep spectra", *Monthly Notices of the Royal Astronomical Society*, Vol. 168, pp. 307–330, 1974b.

14. Riley, J. M., "The structures and properties of 4C radio sources in Abell clusters - I", *Monthly Notices of the Royal Astronomical Society*, Vol. 170, pp. 53–79, 1975.

15. McHardy, I. M., "The structure and properties of 4C radio sources in Abell clusters - II. The declination ranges 10 - 20 and > 50", *Monthly Notices of the Royal Astronomical Society*, Vol. 185, pp. 927–928, 1978b.

16. Fritz, G., A. Davidsen, J. F. Meekins and H. Friedman, "Discovery of an X-Ray Source in Perseus", *The Astrophysical Journal Letters*, Vol. 164, p. L81, 1971.

17. Gursky, H., E. M. Kellogg, C. Leong, H. Tananbaum and R. Giacconi, "Detection of X-Rays from the Seyfert Galaxies NGC 1275 and NGC 4151 by the UHURU Satellite", *The Astrophysical Journal Letters*, Vol. 165, p. L43, 1971a.

18. Gursky, H., E. M. Kellogg, S. Murray, C. Leong, H. Tananbaum and R. Giacconi, "A Strong X-Ray Source in the Coma Cluster Observed by UHURU", *The Astrophysical Journal Letters*, Vol. 167, p. L81, 1971b.

19. Meekins, J. F., F. Gilbert, T. A. Chubb, H. Friedman and R. C. Henry, "Physical

Sciences: X-rays from the Coma Cluster of Galaxies", *Nature*, Vol. 231, pp. 107–108, 1971.

20. Kellogg, E. M., H. Gursky, H. Tananbaum, R. Giacconi and K. Pounds, "The Extended X-Ray Source at M87", *The Astrophysical Journal Letters*, Vol. 174, p. L65, 1972.

21. Forman, W., E. Kellogg, H. Gursky, H. Tananbaum and R. Giacconi, "Observations of the Extended X-Ray Sources in the Perseus and Coma Clusters from UHURU", *The Astrophysical Journal*, Vol. 178, p. 309, 1972.

22. Portinari, L., A. Moretti, C. Chiosi and J. Sommer-Larsen, "Can a "Standard" Initial Mass Function Explain the Metal Enrichment in Clusters of Galaxies?", *The Astrophysical Journal*, Vol. 604, No. 2, p. 579, 2004.

23. Loewenstein, M., "On Iron Enrichment, Star Formation, and Type Ia Supernovae in Galaxy Clusters", *The Astrophysical Journal*, Vol. 648, No. 1, p. 230, 2006.

24. Fabian, A. C., C. S. Crawford, A. C. Edge and R. F. Mushotzky, "Cooling flows and the X-ray luminosity-temperature relation for clusters", *Monthly Notices of the Royal Astronomical Society*, Vol. 267, p. 779, 1994b.

25. Fabian, A. C., J. C. Zarnecki, J. L. Culhane, F.J. Hawkins, A. Peacock, et al., "Copernicus X-Ray Observations of NGC 1275 and the Core of the Perseus Cluster", *The Astrophysical Journal*, Vol. 189, pp. L59-L63, 1974.

26. Mitchell, R. J., P. A. Charles, J. L. Culhane, P. J. N. Davison and A. C. Fabian, "X-ray emission from the Centaurus cluster", *The Astrophysical Journal*, Vol. 200, pp. L5-L8, 1975.

27. Fabian, A. C., "Cooling Flows in Clusters of Galaxies", *Annual Review of Astronomy and Astrophysics*, Vol. 32, pp. 277-318, 1994.

28. Million, E. T. and S. W. Allen, "Chandra measurements of non-thermal X-ray emission from massive, merging, radio-halo clusters", *Monthly Notices of the Royal Astronomical Society*, Vol. 399, pp. 1307–1327, 2009.

29. Voit, G. M., G. L. Bryan, M. L. Balogh and R. G. Bower, "Modified Entropy Models for the Intracluster Medium", *The Astrophysical Journal*, Vol. 576, No. 2, pp. 601–624, 2002.

30. Markevitch, M., "Chandra Observation Of The Most Interesting Cluster In The Universe", *arXiv:astro-ph/0511345*, 2005.

31. Clowe, D., M. Bradac, A. H. Gonzalez, M. Markevitch, R. W. Scott, C. Jones and D. Zaritsky, "A Direct Empirical Proof of the Existence of Dark Matter" *The Astrophysical Journal Letters*, Vol. 648, No. 2, pp. L109, 2006.

32. Takizawa, M., C. L. Sarazin, E. L. Blanton and G.B. Taylor, "Chandra Observations of the Central Region of A3112", *The Astrophysical Journal*, Vol. 595, p. 142, 2003.

33. O'Dea, C. P., S. A. Baum, G. Privon, J. Noel-Storr, A. C. Quillen, et al., "An Infrared Survey of Brightest Cluster Galaxies. II. Why are Some Brightest Cluster Galaxies Forming Stars?", *The Astrophysical Journal*, Vol. 681, No. 2, pp. 1035-1045, 2008.

34. Bulbul, E., R. Smith, A. Foster, J. Cottam, M. Loewenstein, R. Mushotzky and R. Shafer, "High-Resolution XMM-Newton Spectroscopy Of The Cooling Flow Cluster A3112", *The Astrophysical Journal*, Vol. 747, No. 1, 2012.

35. Nevalainen, J., R. Lieu, M. Bonamente and D. Lumb, "Soft X-Ray Excess Emission in Clusters of Galaxies Observed with XMM-Newton", *The Astrophysical Journal*, Vol. 584, No. 2, p. 716, 2003.

36. Bonamente, M., J. Nevalainen and R. Lieu, "Soft and Hard X-Ray Excess Emission

in Abell 3112 Observed with Chandra", *The Astrophysical Journal*, Vol. 668, No. 2, 2007.

37. Lehto, T., J. Nevalainen, M. Bonamente, N. Ota and J. Kaastra, "Suzaku observations of X-ray excess emission in the cluster of galaxies A3112", *Astronomy and Astrophysics*, Vol. 524, No. A70, 2010.

38. Bulbul, E., R. K. Smith and M. Loewenstein, "A New Method to Constrain Supernova Fractions Using X-Ray Observations of Clusters of Galaxies", *The Astrophysical Journal*, Volume 753, Vol. 1, p. 54, 2012.

39. Karzas, W. J. and R. Latter, "Electron Radiative Transitions in a Coulomb Field", *The Astrophysical Journal Supplement Series*, Vol. 6, p. 167, 1961.

40. Osterbrock, D. E., "Astrophysics of gaseous nebulae", Freeman & Co, San Francisco, 1974.

41. Sarazin, C. L., "X-ray emission from clusters of galaxies", Cambridge Astrophysics Series, Cambridge University Press, 1988.

42. Mitchell, R. J., J. L. Culhane, P. J. N. Davison and J. C. Ives, "Ariel 5 Observations of the X-ray Spectrum of the Perseus Cluster", *Monthly Notices of the Royal Astronomical Society*, Vol. 175, pp. 29-34, 1976.

43. Böhringer, H., "X-ray Observations of the Chemical Abundances in the Intra-Cluster Medium", *Memorie della Societa Astronomica Italiana*, Vol. 85, p. 396, 2014.

44. Smith, R.K., N.S. Brickhouse, D.A. Liedahl, and J. C. Raymond, "Collisional Plasma Models with APEC/APED: Emission-Line Diagnostics of Hydrogen-like and Helium-like Ions", *Astrophysical Journal*, Vol. 556, p. L91, 2001.

45. Foster, A. R., L. Ji, R. K. Smith and N. S. Brickhouse, "Updated Atomic Data

and Calculations for X-Ray Spectroscopy", *Astrophysical Journal*, Vol. 756, p. 128, 2012.

46. Arnaud, K. A., "XSPEC: The First Ten Years", *Astronomical Data Analysis Software and Systems V, Conference Series*, Vol. 101, p. 17, 1996.

47. Leibundgut, B., "Supernovae and cosmology", *General Relativity and Gravitation*, Vol. 40, No. 2, pp. 221-248, 2008.

48. Weiler, K. W., "Supernovae and Gamma-Ray Bursters", Springer, Berlin, 2003.

49. Woosley, S. E. and T. A. Weaver, "The physics of supernova explosions", *Annual Review of Astronomy and Astrophysics*, Vol. 24, pp. 205-253, 1986.

50. Chris Milos, *Lecture Notes*, 2017, `http://burro.astr.cwru.edu/Academics/Astr221/LifeCycle/highmassburn.html`, accessed at January 2017.

51. Chandrasekhar, S., "The Maximum Mass of Ideal White Dwarfs", *Astrophysical Journal*, Vol. 74, p.81, 1931.

52. Whelan, J. and Jr. I. Iben, "Binaries and Supernovae of Type I", *Astrophysical Journal*, Vol. 186, pp. 1007-1014, 1973.

53. Ashley Villar, *Daily Paper Summaries: Super - bright Supernovae are Single - Degenerate?"*, 2015, `https://astrobites.org/2015/04/07/super-bright-supernovae-are-single-degenerate`, accessed at January 2017.

54. van den Heuvel, E. P. J., D. Bhattacharya, K. Nomoto, S. A. Rappaport, "Accreting white dwarf models for CAL 83, CAL 87 and other ultrasoft X-ray sources in the LMC", *Astronomy and Astrophysics*, Vol. 262, No. 1, pp. 97-105, 1992.

55. Han, Z. and P. Podsiadlowski, "The single-degenerate channel for the progenitors of Type Ia supernovae", *Monthly Notices of the Royal Astronomical Society*, Vol.

350, No. 4, pp. 1301-1309, 2004.

56. Tutukov, A. V. and L. Yungelson, "Double-degenerate semidetached binaries with helium secondaries: cataclysmic variables, supersoft X-ray sources, supernovae and accretion-induced collapses", *Monthly Notices of the Royal Astronomical Society*, Vol. 280, No. 4, pp. 1035-1045, 1996.

57. Patat, F., N. N. Chugai, P. Podsiadlowski, E. Mason, C. Melo and L. Pasquini, "Connecting RS Ophiuchi to [some] type Ia supernovae", *Astronomy and Astrophysics*, Vol. 530, No. A63, 2011.

58. Li, X. D. and E. P. J. van den Heuvel, "Evolution of white dwarf binaries: supersoft X-ray sources and progenitors of type IA supernovae", *Astronomy and Astrophysics*, Vol. 322, pp. L9-L12, 1997.

59. Iben, Jr. I. and A. V., Tutukov, "Supernovae of type I as end products of the evolution of binaries with components of moderate initial mass", *The Astrophysical Journal Supplement Series*, Vol. 54, pp. 335-372, 1984.

60. Webbink, R. F., "Double white dwarfs as progenitors of R Coronae Borealis stars and type I supernovae", *Astrophysical Journal*, Vol. 277, pp. 355-360, 1984.

61. Piersanti, L., S. Gagliardi, I. Jr. Iben and A. Tornambé, "Carbon-Oxygen White Dwarf Accreting CO-Rich Matter. II. Self-Regulating Accretion Process up to the Explosive Stage", *The Astrophysical Journal*, Vol. 598, No. 2, pp. 1229-1238, 2003.

62. Paczyński, B., "Gravitational Waves and the Evolution of Close Binaries", *Acta Astronautica*, Vol. 17, p. 287, 1967.

63. Saio, H. and K. Nomoto, "Evolution of a merging pair of C + O white dwarfs to form a single neutron star", *Astronomy and Astrophysics*, Vol. 150, No. 1, pp. L21-L23, 1985.

64. Nomoto, K. and Y. Kondo, "Conditions for accretion-induced collapse of white dwarfs", *Astrophysical Journal*, Vol. 367, pp. L19-L22, 1991.

65. Arnett, W. D.,"A possible model of supernovae: Detonation of ^{12}C",*Astrophysics and Space Science*, Vol. 5, No. 2, p. 180, 1969.

66. Khokhlov, A. M., "Delayed detonation model for type IA supernovae", *Astronomy and Astrophysics*, Vol. 245, No. 1, pp. 114-128, 1991.

67. Yamaoka, H., K. Nomoto, T. Shigeyama and F. Thielemann, "Late detonation models for the type IA supernovae SN 1991T and SN 1990N", *The Astrophysical Journal*, Vol. 393, No. 2, pp. L55-L58, 1992.

68. Iwamoto, K., F. Brachwitz, K. Nomoto, N. Kishimoto, H. Umeda, W. R. Hix and F. K. Thielemann, "Nucleosynthesis in Chandrasekhar Mass Models for Type IA Supernovae and Constraints on Progenitor Systems and Burning-Front Propagation", *The Astrophysical Journal Supplement Series*, Vol. 125, No. 2, pp. 439-462, 1999.

69. Maeda, K., F. K. Röpke, M. Fink, W. Hillebrandt, C. Travaglio, F. K. Thielemann, "Nucleosynthesis in Two-Dimensional Delayed Detonation Models of Type Ia Supernova Explosions", *The Astrophysical Journal*, Vol. 712, No. 1, pp. 624-638, 2010.

70. Bulbul, E., R. K. Smith and M. Loewenstein, "A New Method to Constrain Supernova Fractions Using X-Ray Observations of Clusters of Galaxies", *The Astrophysical Journal*, Vol. 753, No. 1, 2012.

71. NASA, "Spectra for galaxy clusters using abundances based on models for SN yields", 2015, `http://heasarc.gsfc.nasa.gov/xanadu/xspec/models/snapec.html`, accessed at January 2017.

72. Salpeter E. E., "The Luminosity Function and Stellar Evolution", *Astrophysical*

Journal, Vol. 121, p.161, 1955.

73. NASA, *Lecture Notes*, 2013, https://imagine.gsfc.nasa.gov/science/toolbox/emspectrum1.html, accessed at January 2017.

74. Mitsuda, K., M. W. Bautz, H. Inoue, R. L. Kelley, et al., "The X-Ray Observatory Suzaku", *Publications of the Astronomical Society of Japan*, Vol. 59, No. SP1, pp.1-7, 2007.

75. The Suzaku Technical Description, 2007, https://heasarc.gsfc.nasa.gov/docs/astroe/prop_tools/suzaku_td/node6.html, accessed at January 2017.

76. The Suzaku Technical Description, 2007, http://www.astro.isas.ac.jp/suzaku/proposal/ao3/suzaku_td/node9.html, accessed at January 2017.

77. Serlemitsos P., Y. Soong, K.W. Chan, T. Okajima, et al., "The X-Ray Telescope onboard Suzaku", *Publications of Astronomical Society of Japan*, Vol. 59, No. sp1, pp. S9-S21, 2007.

78. Suzaku X-Ray Observatory, 2015, http://www.astro.isas.ac.jp/suzaku/proposal/ao3/suzaku_td/node9.html\#SECTION00911000000000000000, accessed at January 2017.

79. Koyama K., H. Tsunemi, D. Tadayasu, M. W. Bautz, et al., "X-Ray Imaging Spectrometer (XIS) on Board Suzaku", *Publications of the Astronomical Society of Japan*, Vol. 59, No. SP1, pp. 23-33, 2007.

80. The Chandra X-Ray Observatory, 2017, http://chandra.harvard.edu/graphics/resources/illustrations/orbit/orbit5-72l.jpg, accessed at January 2017.

81. The Chandra X-Ray Observatory, 2017, http://chandra.harvard.edu/graphics/resources/illustrations/cxcmirrors-72.jpg, accessed at January

2017.

82. The Chandra Proposers' Observatory Guide, 2016, `http://cxc.harvard.edu/proposer/POG/html/chap6.html`, accessed at January 2017.

83. Ezer, C., E. Bulbul, E. N. Ercan, R. K. Smith, M. W. Bautz, M. Loewenstein, M. McDonald and E. D. Miller, "Uniform Contribution of Supernova Explosions to the Chemical Enrichment of Abell 3112 out to R_{200}", *The Astrophysical Journal*, Vol. 836, No. 1, 2017.

84. Suzaku XIS Team, "Screening criteria for the XIS data in the version 2.0 processing", 2007, `http://heasarc.gsfc.nasa.gov/docs/suzaku/processing/criteria_xis.html`, accessed at January 2017.

85. Suzaku XIS Team, "A new recipe for generating NXB background spectra", 2015, `http://www.astro.isas.jaxa.jp/suzaku/analysis/xis/nxb\_new/`, accessed at January 2017.

86. Bulbul, E., S. W. Randall, M. Bayliss, E. D. Miller, F. Andrade-Santos, R. Johnson, M. Bautz, et al., "Probing The Outskirts Of The Early-stage Galaxy Cluster Merger A1750", *The Astrophysical Journal*, Vol. 818, No. 2, 2016.

87. Markevitch, M., M. W. Bautz, B. Biller, Y. Butt, R. Edgar, et al., "Chandra Spectra of the Soft X-Ray Diffuse Background", *The Astrophysical Journal*, Vol. 583, Issue 1, pp. 70-84, 2003.

88. Hickox, R. C. and M. Markevitch, "Absolute measurement of the unresolved X-ray background in the 0.5-8 keV band with Chandra", *The Astrophysical Journal*, Vol. 645, No. 1, 2006.

89. Snowden, S. L., M. R. Collier and K. D. Kuntz, "XMM-Newton Observation of Solar Wind Charge Exchange Emission", *The Astrophysical Journal*, Vol. 610, Issue 2, pp. 1182-1190, 2004.

90. Fabian, A. and X. Barcons, "The origin of the X-ray background", *Annual Review of Astronomy and Astrophysics*, Vol. 30, pp. 429-456, 1992.

91. Mushotzky, R., L. L. Cowie, A. J. Barger and K. A. Arnaud, "Resolving the extragalactic hard X-ray background", *Nature*, Vol. 404, Issue 6777, pp. 459-464, 2000.

92. Kalberla, P. M. W., W. B. Burton, D. Hartmann, E. M, Arnal, et al., "The Leiden/Argentine/Bonn (LAB) Survey of Galactic HI. Final data release of the combined LDS and IAR surveys with improved stray-radiation corrections", *Astronomy and Astrophysics*, Vol. 440, Issue 2, pp.775-782, 2005.

93. NASA, *Near-Earth Supernovas*, 2003, `https://science.nasa.gov/science-news/science-at-nasa/2003/06jan_bubble`, accessed at January 2017.

94. Snowden, S. L., U. Mebold, W. Hirth, U. Herbstmeier, and J. H. M. Schmitt, "ROSAT detection of an X-ray shadow in the 1/4-keV diffuse background in the Draco nebula", *Science*, Vol. 252, pp. 1529-1532, 1991.

95. Lilienthal, D., A. Wennmacher, U. Herbstmeier and U. Mebold, "Interstellar NA I D line studies of stars towards the Draco nebula", *Astronomy and Astrophysics*, Vol. 250, No. 1, pp. 150-158, 1991.

96. Masui, K., K. Mitsuda, N. Y. Yamasaki, Y. Takei, Y. Kimura and T. Yoshino, "The Nature of Unresolved Soft X-Ray Emission from the Galactic Disk", *Publications of Astronomical Society of Japan*, Vol. 61, pp. S115-S122, 2009.

97. Simionescu, A., S. W. Allen, A. Mantz, N. Werner and Y. Takei, "Baryons in the outskirts of the X-ray brightest galaxy cluster", *American Institute of Physics Conference Proceedings*, Vol. 1427, No. 1, 2012.

98. NASA, "X-Ray Background Tool", 2014, `http://heasarc.gsfc.nasa.gov/`

`cgi-bin/Tools/xraybg/xraybg.pl`, accessed at January 2017.

99. Moretti, A., S. Campana, D. Lazzati and G., Tagliaferri, "The Resolved Fraction of the Cosmic X-Ray Background", *The Astrophysical Journal*, Vol. 588, No. 2, pp. 696-703, 2003.

100. Moretti, A., C. Pagani, G. Cusumano, S. Campana, M. Perri, et al., "A new measurement of the cosmic X-ray background", *Astronomy and Astrophysics*, Vol. 493, No. 2, pp. 501-509, 2009.

101. De Luca, A. and S. Molendi, "The 2-8 keV cosmic X-ray background spectrum as observed with XMM-Newton", *Astronomy and Astrophysics*, Vol. 419, pp.837-848, 2004.

102. Tawa, N., K. Hayashida, M. Nagai, H. Nakamoto, H. Tsunemi, H. Yamaguchi, et al., "Reproducibility of Non-X-Ray Background for the X-Ray Imaging Spectrometer aboard Suzaku", *Publications of the Astronomical Society of Japan*, Vol. 60, No. SP1, pp. S11-S24, 2008.

103. Ishisaki, Y., Y. Maeda, R. Fujimoto, O. Masanobu, K. Ebisawa, et al., "Monte Carlo Simulator and Ancillary Response Generator of Suzaku XRT/XIS System for Spatially Extended Source Analysis", *Publications of the Astronomical Society of Japan*, Vol. 59, No. SP1, pp.113-132, 2007.

104. Bautz, M. W., E. D. Miller, J. S. Sanders, K. A. Arnaud, R. F. Mushotzky, F. S. Porter, K. Hayashida, et al., "Suzaku Observations of Abell 1795: Cluster Emission to r_{200}", *Publications of the Astronomical Society of Japan*, Vol. 61, No. 5, pp.1117-1133, 2009.

105. Simionescu, A., N. Werner, O. Urban, S. W. Allen, Y. Ichinohe and I. Zhuravleva, "A Uniform Contribution Of Core-Collapse and Type Ia Supernovae To The Chemical Enrichment Pattern In The Outskirts Of The Virgo Cluster", *The Astrophysical Journal Letters*, Vol. 811, No. 2, 2015.

106. Werner, N., O. Urban, A. Simionescu and S. A. Allen, "A uniform metal distribution in the intergalactic medium of the Perseus cluster of galaxies", *Nature*, Vol. 502, pp. 656-658, 2013.

107. Baumgartner, W. H., M. Loewenstein, D. J. Horner and R. F. Mushotzky, "Intermediate-Element Abundances in Galaxy Clusters", *The Astrophysical Journal*, Vol. 620, Issue 2, pp. 680-696, 2005.

108. Mushotzky, R. F. and M. Loewenstein, "Lack of Evolution in the Iron Abundance in Clusters of Galaxies and Implications for the Global Star Formation Rate at High Redshift", *The Astrophysical Journal*, Vol. 481, Issue 2, pp. L63-L66, 1997.

109. Ishimaru, Y. and N. Arimoto, "Roles of SN IA and SN II in ICM Enrichment", *Publications of the Astronomical Society of Japan*, Vol.49, pp.1-8, 1997.

110. Finoguenov, A., L. P. David and T. J. Ponman, "An ASCA Study of the Heavy-Element Distribution in Clusters of Galaxies", *The Astrophysical Journal*, Vol. 544, Issue 1, pp. 188-203, 2000.

111. Dupke, R. A. and R. E., White III, "Constraints on Type Ia Supernova Models from X-Ray Spectra of Galaxy Clusters", *The Astrophysical Journal*, Vol. 528, pp.139-144, 2000.

112. Buote, D. A., A. D. Lewis, F. Brighenti and W. G. Mathews, "XMM-Newton and Chandra Observations of the Galaxy Group NGC 5044. II. Metal Abundances and Supernova Fraction", *The Astrophysical Journal*, Vol. 595, Issue 1, pp. 151-166, 2003.

113. Werner, N., J. de Plaa, J. S. Kaastra, J. Vink, J. A. M. Bleeker, T. Tamura, J. R. Peterson and F. Verbunt, "XMM-Newton spectroscopy of the cluster of galaxies 2A 0335+096", *Astronomy and Astrophysics*, Vol. 449, pp.475-491, 2006.

114. de Plaa, J., N. Werner, J. A. M. Bleeker, J. Vink, J. S. Kaastra and M. Méndez,

"Constraining supernova models using the hot gas in clusters of galaxies", *Astronomy and Astrophysics*, Vol. 465, No. 2, pp. 345-355, 2007.

115. Nomoto, K., N. Tominaga, U. Hideyuki, C. Kobayashi and K. Maeda, "Nucleosynthesis yields of core-collapse supernovae and hypernovae, and galactic chemical evolution", *Nuclear Physics A*, Vol. 777, pp. 424-458, 2006.

116. Matsushita, K., H. Böhringer, I. Takahashi and Y. Ikebe, "The abundance pattern of O, Mg, Si, and Fe in the intracluster medium of the Centaurus cluster observed with XMM-Newton", *Astronomy and Astrophysics*, Vol. 462, No. 3, pp. 953-963, 2007.

117. Baldi, A., S. Ettori, P. Mazzotta, P. Tozzi, and S. Borgani, "A Chandra Archival Study of the Temperature and Metal Abundance Profiles in Hot Galaxy Clusters at $0.1 < z < 0.3$", *The Astrophysical Journal*, Vol. 666, No. 2, pp. 835-845, 2007.

118. De Grandi, S., S. Ettori M. Longhetti, S. Molendi, "On the iron content in rich nearby clusters of galaxies", *Astronomy and Astrophysics*, Vol. 419, pp. 7-18, 2004.

119. Böhringer, H., K. Matsushita, E. Churazov, A. Finoguenov and Y. Ikebe, "Implications of the central metal abundance peak in cooling core clusters of galaxies", *Astronomy and Astrophysics*, Vol. 416, pp. L21-L25, 2004.

120. Simionescu, A., N. Werner, H. Böhringer, J. S. Kaastra, A. Finoguenov, M. Brüggen and P. E. J. Nulsen, "Chemical enrichment in the cluster of galaxies Hydra A", *Astronomy and Astrophysics*, Vol. 493, No. 2, pp. 409-424, 2009.

121. De Grandi, S., J. S. Santos and S. M. Nonino, "On the Fe abundance peak formation in cool-core clusters of galaxies: hints from cluster WARPJ1415.1+3612 at $z = 1.03$", *Astronomy and Astrophysics*, Vol. 567, No. A102, 2014.

122. Mernier, F., J. de Plaa, C. Pinto, J. S. Kaastra, P. Kosec, Y. Zhang, J. Mao, et al., "Origin of central abundances in the hot intra-cluster medium - II. Chemical

enrichment and supernova yield models", *Astronomy and Astrophysics*, Vol. 595, No. A126, 2016.

123. Tsujimoto, T., K. Nomoto, Y. Yoshii, M. Hashimoto, S. Yanagida and F. K. Thielemann, "Relative frequencies of Type Ia and Type II supernovae in the chemical evolution of the Galaxy, LMC and SMC", *Monthly Notices of the Royal Astronomical Society*, Vol. 277, Issue 3, pp. 945-958, 1995.

124. Tran, K. V. H., M. Franx, G. D. Illingworth, P. van Dokkum, D. D. Kelson, et al., "A Keck Spectroscopic Survey of MS 1054-03 (z = 0.83): Forming the Red Sequence", *The Astrophysical Journal*, Vol. 661, p. 750, 2007.

125. Ettori, S., A. Baldi, I. Balestra, F. Gastaldello, S. Molendi and P. Tozzi, "The evolution of the spatially-resolved metal abundance in galaxy clusters up to z=1.4", *Astronomy & Astrophsics*, Vol. 478, No. A46, 2015.

126. McDonald, M., E. Bulbul, T. de Haan, E. D. Miller, B. A. Benson, L. E. Bleem, M. Brodwin, J. E. Carlstrom, I. Chiu and W. R. Forman, "The Evolution Of The Intracluster Medium Metallicity In Sunyaev Zel'dovich Selected Galaxy Clusters At $0 > z > 1.5$", *The Astrophysical Journal*, Vol. 826, No. 2, 2016.

127. Sanders J., "Direct X-ray Spectra Deprojection", 2016, `https://www-xray.ast.cam.ac.uk/papers/dsdeproj/`, accessed at January 2017.

128. Sanders, J. S. and A. C. Fabian, "A deeper X-ray study of the core of the Perseus galaxy cluster: the power of sound waves and the distribution of metals and cosmic rays", *Monthly Notices of the Royal Astronomical Society*, Vol. 381, pp. 1381-1399, 2007.

129. Russell H. R., J. S. Sanders and A. C. Fabian, "Direct X-ray spectral deprojection of galaxy clusters", *Monthly Notices of the Royal Astronomical Society*, Vol. 390, p. 1207, 2008.

130. McLaughlin, D. E., "The Efficiency Of Globular Cluster Formation", *The Astronomical Journal*, Vol. 117, No. 5, pp. 2398-2427, 1999.

131. King, IR., "The structure of star clusters. I. an empirical density law" , *Astronomical Journal*, Vol. 67, p. 471, 1962.

132. Bulbul, E., N. Hasler, M. Bonamente and M. Joy, "An Analytic Model of the Physical Properties of Galaxy Clusters", *The Astrophysical Journal*, Vol. 720, p. 1038, 2010.

133. Sunyaev, R.A. and Y. B. Zel'dovich, "Formation of Clusters of Galaxies; Protocluster Fragmentation and Intergalactic Gas Heating", *Astronomy and Astrophysics*, Vol. 20, p. 189, 1972.

134. Navarro, J. F., C. S. Frenk and S. D. M. White, "The Structure of Cold Dark Matter Halos", *The Astrophysical Journal*, Vol. 462, p. 563, 1996.

135. Hinshaw, G., D. Larson, E. Komatsu, D. N. Spergel, C. L. Bennett, J. Dunkley, et al., "Nine-year Wilkinson Microwave Anisotropy Probe (WMAP) Observations: Cosmological Parameter Results", *The Astrophysical Journal Supplement Series*, Vol. 208, No. 2, 2013.

136. Pointecouteau, E., T. H. Reiprich, C. Adami, M. Arnaud, V. Biffi, S. Borgani, K. Borm, et al., "The Hot and Energetic Universe: The evolution of galaxy groups and clusters", *arXiv:1306.2319, 2013.*